



SURVEY OF MILITARY APPLICATIONS
FOR FOURIER TRANSFORM INFRARED (FTIR)
SPECTROSCOPY

THESIS

ROBERT G. HAUSER, CAPTAIN, USAF

AFIT/GM/ENP/99M-07

19990402 024

DISTRIBUTION STATEMENT A
Approved for Public Release
Distribution Unlimited

DEPARTMENT OF THE AIR FORCE
AIR UNIVERSITY

AIR FORCE INSTITUTE OF TECHNOLOGY

DTIC QUALITY INSPECTED 2

Wright-Patterson Air Force Base, Ohio

AFIT/GM/ENP/99M-07

SURVEY OF MILITARY APPLICATIONS FOR
FOURIER TRANSFORM INFRARED (FTIR) SPECTROSCOPY

THESIS

Presented to the Faculty of the Graduate School of Engineering

of the Air Force Institute of Technology

Air University

Air Education and Training Command

in Partial Fulfillment of the Requirements for the

Degree of Master of Science in Meteorology

Robert G. Hauser, B.A.

Captain, USAF

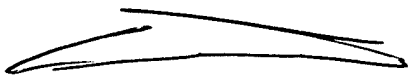
February 1999

Approved for public release; distribution unlimited

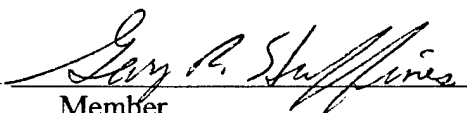
SURVEY OF MILITARY APPLICATIONS FOR
FOURIER TRANSFORM INFRARED (FTIR) SPECTROSCOPY

Robert G. Hauser, B.A.
Captain, USAF

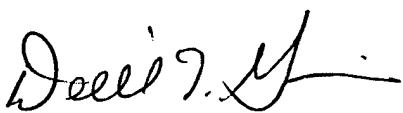
Approved:


Chairman

8 MAR 99
date


Member

2 Mar 99
date


Member

2 Mar 99
date

Acknowledgments

I would like to take this time to acknowledge all of the support and understanding my loving family provided to me during the past 18 months. Without their help this would have been a much more difficult effort. To my wife Khande, who many times gave me the encouragement I needed to keep going. To my kids, who I told too often, "not right now, I'm doing homework," I look forward to playgrounds and ball games.

I would also like to thank my advisor, Lt Col Glen Perram for providing me the latitude and guidance to complete this research effort.

And lastly, I must thank my classmates. I do not think I could have made it through mathematics and dynamics without their help.

Robert G. Hauser

Table of Contents

Acknowledgments.....	iv
Table of Contents	v
List of Figures	vii
List of Tables	xii
Abstract	xiii
 SURVEY OF MILITARY APPLICATIONS FOR FOURIER TRANSFORM INFRARED (FTIR) SPECTROSCOPY	 1
 Part 1-- Determining Vertical Atmospheric Temperature and Moisture Profiles from Radiance Data and Validating Atmospheric Transmittance Models with a Fourier Transform Infrared (FTIR) Spectrometer	 1
I. Introduction	1
Summary	1
Spectrometer's Components.....	2
Principles of Operation	4
Calibration Theory	7
Atmospheric Radiation Theory.....	8
The Moderate Resolution Transmittance Model (MODTRAN)	13
Radiative Transfer Equation and Retrieval Methods.....	16
Environmental Monitoring.....	17
Assumptions and Limitations	17
II. Literature Review	20
III. Methodology	24
Summary	24
Data Collection and Calibration Technique.....	24
Determining the Kernel Functions.....	26
The Physical Retrieval	31
Model Validation	31
Environmental Monitoring.....	34
IV. Results for Part 1	36
Determining the Kernel Functions.....	36

The Physical Retrieval	37
Model Validation	38
Environmental Monitoring.....	48
V. Conclusions for Part 1.....	50
Part 2-Spectral Features of Conventional Warhead Explosions	52
I. Introduction	52
Summary.....	52
Background.....	52
Assumptions and Limitations	54
II. Methodology	55
III. Results for Part 2.....	59
V. Conclusions for Part 2.....	66
Appendix 1: Weather Data.....	68
Weather Data for 5 October 1998	68
Weather Data for 20 October 1998	68
Weather Data for 11 November 1998	69
Weather Data for 25 November 1998	70
Appendix 2: Event Information for Part 2	72
Appendix 3: Additional Spectral Plots of Explosion Events.....	76
Bibliography	129
Vita.....	131

List of Figures

Figure	Page
1.1. Diagram of side view of MR-154 spectrometer with main components labeled.....	3
1.2. Principle of operation of the FTIR spectrometer	6
1.3a. Combined atmospheric radiance due to water vapor, carbon dioxide, and nitrous oxide.....	9
1.3b. Atmospheric radiance due to carbon dioxide along 600 to 3500 cm ⁻¹ using HITRAN.....	9
1.3c. Atmospheric radiance due to water vapor. Calculated using HITRAN 1996.....	10
1.3d. Atmospheric radiance due to nitrous oxide. Calculated using HITRAN 1996.....	10
1.4a. Vibrational modes of the water vapor molecule.	12
1.4b. Vibrational modes of the carbon dioxide molecule.	12
1.5a. Atmospheric transmittance plot generated by MODTRAN using PLEXUS 2.1b.....	15
1.5b. Atmospheric radiance plot associated with Figure 1.6a	15
1.6a. Kernel functions calculated from the surface looking up for selected wavenumbers by height (m).	30
1.6b. Kernel functions calculated from 45 km altitude looking down for selected wavenumbers by height (m).	30
1.7. Example matrix for kernel functions	37
1.8a. Spectral plot of cloudy sky on 5 October 1998.....	39
1.8b. Spectral plot of mostly cloudy sky on 5 October 1998.....	39
1.8c. Spectral plot of clear sky on 5 October 1998.....	39
1.9a. Observed radiance from 0728 LST to 0900 LST compared to MODTRAN calculated radiance.....	41

1.9b. Observed radiance from 0728 LST to 0900 LST compared to MODTRAN calculated radiance in spectral region 620 to 720 cm^{-1}	41
1.9c. Observed radiance from 0728 LST to 0900 LST compared to MODTRAN calculated radiance in spectral region 800 to 1000 cm^{-1}	42
1.9d. Observed radiance from 0728 LST to 0900 LST compared to MODTRAN calculated radiance in spectral region 1000 to 1200 cm^{-1}	42
1.10a. Radiance observed at 0900 LST 11 November 1998 compared to MODTRAN calculated radiance using 1200 UTC rawinsonde from Wilmington OH.	44
1.10b. Radiance observed at 0900 LST 11 November 1998 compared to MODTRAN calculated radiance using 1200 UTC rawinsonde from Wilmington OH.....	44
1.10c. Radiance observed at 0900 LST 11 November 1998 compared to MODTRAN calculated radiance using 1200 UTC rawinsonde from Wilmington OH.....	45
1.10d. Radiance observed at 0900 LST 11 November 1998 compared to MODTRAN calculated radiance using 1200 UTC rawinsonde from Wilmington OH.....	45
1.10e. Radiance observed at 0900 LST 11 November 1998 for elevation angles of 15, 30, and 45 degrees.	46
1.10f. Radiance calculated for 0900 LST 11 November 1998 using MODTRAN with a representative sounding for 15, 30, and 45 degrees elevation.	46
1.11. Spectral plot of emissions from a coal-burning plant smokestack located near Area B Wright-Patterson AFB compared to background radiance.	49
2.1. Photograph of spectrometer's view of bomb range.	55
2.2. Photograph of deployed computer used to operate spectrometer.....	55
2.3. Photograph of West Tower on Bravo 20 Bomb Range.	56
2.4. Photograph of aligning the spectrometer with the black body.	57
2.5. Initial spectral signature of event 1, Mk 82 bomb explosion.	62
2.6. Initial spectral signature of event 34, HARM missile explosion.....	63
2.7. Initial spectral signature of event 43, TLAM missile explosion.	64
2.8. Initial spectral signature of event A, C-4 plastic explosives detonation.....	65

A3.1a.	Initial spectral signature of event 1, Mk 82 bomb explosion.	79
A3.1b.	Spectral signature 0.279 seconds after A3.1a.....	80
A3.1c.	Spectral signature 0.555 seconds after A3.1a.....	81
A3.2a.	Initial spectral signature of event 5, Mk 82 bomb explosion.	82
A3.2b.	Spectral signature 0.279 seconds after A3.2a.....	83
A3.3a.	Initial spectral signature of event 9, Mk 82 bomb explosion.	84
A3.3b.	Spectral signature 0.278 seconds after A3.3a.....	85
A3.4.	Spectral signature of event 11, Mk 82 explosion.	86
A3.5.	Spectral signature of event 21, Mk 82 explosion.	87
A3.6.	Spectral signature of event 23, Mk 82 explosion.	88
A3.7.	Spectral signature of event 29, Mk 82 explosion.	89
A3.8a.	Initial spectral signature of event 34, HARM missile.	90
A3.8b.	Spectral signature 0.278 seconds after A3.8a.....	91
A3.9a.	Initial spectral signature of event 36, HARM missile.	92
A3.9b.	Spectral signature 0.278 seconds after A3.9a.....	93
A3.10a.	Initial spectral signature of event 49, TLAM missile.....	94
A3.10b.	Spectral signature 0.269 seconds after A3.10a.....	95
A3.10c.	Spectral signature 0.538 seconds after A3.10a.....	96
A3.11.	Spectral signature of event 53, TLAM missile.....	97
A3.12a.	Initial spectral signature of event 54, TLAM missile.....	98
A3.12b.	Spectral signature 0.807 seconds after A3.12a.....	99
A3.12c.	Spectral signature 1.347 seconds after A3.12a.....	100

A3.13a. Initial spectral signature of event 43, TLAM missile.....	101
A3.13b. Spectral signature 0.267 seconds after A3.13a.....	102
A3.13c. Spectral signature 0.536 seconds after A3.13a.....	103
A3.13d. Spectral signature 0.804 seconds after A3.13a.....	104
A3.14a. Initial spectral signature of event 47, Mk 84 bomb.....	105
A3.14b. Spectral signature 0.267 seconds after A3.14a.....	106
A3.14c. Spectral signature 0.536 seconds after A3.14a.....	107
A3.14d. Spectral signature 0.803 seconds after A3.14a.....	108
A3.14e. Spectral signature 1.071 seconds after A3.14a.....	109
A3.14f. Spectral signature 1.339 seconds after A3.14a.....	110
A3.14g. Spectral signature 1.606 seconds after A3.14a.....	111
A3.15a. Initial spectral signature of event 45, Mk 84 bomb.....	112
A3.15b. Spectral signature 0.269 seconds after A3.15a.....	113
A3.15c. Spectral signature 0.537 seconds after A3.15a.....	114
A3.16a. Initial spectral signature of event 52, Mk 83 bomb.....	115
A3.16b. Spectral signature 0.271 seconds after A3.16a.....	116
A3.16c. Spectral signature 0.540 seconds after A3.16a.....	117
A3.16d. Spectral signature 0.810 seconds after A3.16a.....	118
A3.16e. Spectral signature 1.080 seconds after A3.16a.....	119
A3.16f. Spectral signature 1.351 seconds after A3.16a.....	120
A3.16g. Spectral signature 1.621 seconds after A3.16a.....	121
A3.17a. Initial spectral signature of event A, C-4 plastic explosive.....	122
A3.17b. Spectral signature 0.270 seconds after A3.17a.....	123
A3.17c. Spectral signature 0.538 seconds after A3.17a.....	124

A3.18a. Initial spectral signature of event C, C-4 plastic explosive.	125
A3.18b. Spectral signature 0.538 seconds after A3.18a.....	126
A3.19a. Example of radio frequency interference patterns	127
A3.19b. Observed background plotted against scale of typical explosion.....	128

List of Tables

Table	Page
1. Example worksheet of atmospheric transmittances.	28
2. Example worksheet of calculated kernel functions.	29
A2.1. Information on the explosion events on day 1.....	72
A2.2. Information on the explosion events on day 2.....	73
A2.3. Information on the explosion events on day 3.....	74
A2.4. Information on the explosion events on day 4.....	75

Abstract

In Part 1--Determining Vertical Atmospheric Temperature and Moisture Profiles from Radiance Data and Validating Atmospheric Transmittance Models with a Fourier Transform Infrared (FTIR) Spectrometer, two meteorological applications and one environmental application were investigated. A method to retrieve vertical atmospheric temperature and moisture profiles by applying a least-squares solution to atmospheric radiance observed at the surface in the 4.3- μm carbon dioxide absorption band was analyzed. The method did not work. Weighting functions calculated between 2250 cm^{-1} and 2400 cm^{-1} from the surface looking up at a 45-degree angle were a maximum at the surface, so no unique solution for temperature retrieval by height could be determined. Atmospheric radiances, observed under various meteorological conditions and viewing angles, were compared to radiances calculated using the Moderate Resolution Transmittance Code (MODTRAN). The utility of the FTIR spectrometer for environmental monitoring was demonstrated by identifying emissions from a coal-burning plant. Constituent gases identified were CO_2 , CO , O_3 , HCl , SO_2 , and N_2O .

In Part 2--Spectral Features of Conventional Warhead Explosions, results are presented from a field test where an FTIR spectrometer was used to collect data of conventional warhead explosions from 7 December 1998 to 11 December 1998 at Fallon Naval Air Station NV. Data of controlled detonations of statically displayed Mk 82, Mk 83, and Mk 84 bombs; High-speed Anti-Radiant Missiles (HARM); Tomahawk Land-Attack Missiles (TLAM); and C-4 plastic explosives were collected over the 1800 cm^{-1} to 6000 cm^{-1} spectral band at resolutions of 16 cm^{-1} . Spectral plots of the explosions

showed there were unique spectral features associated with some warhead detonations.

The preliminary results of this effort suggest it may be possible to identify the type of warhead detonated by its spectral signature alone.

SURVEY OF MILITARY APPLICATIONS FOR FOURIER TRANSFORM INFRARED (FTIR) SPECTROSCOPY

Part 1-- Determining Vertical Atmospheric Temperature and Moisture Profiles from Radiance Data and Validating Atmospheric Transmittance Models with a Fourier Transform Infrared (FTIR) Spectrometer

I. Introduction

Summary

This introductory section to Part 1 covers background information needed by anyone not familiar with a Fourier Transform Infrared (FTIR) spectrometer, atmospheric radiation, the radiative transfer equation, and retrieval methods. An introduction to the spectrometer and its components is followed by an explanation of its principle of operation. An important step in the data analysis process is properly calibrating the data for accuracy, so calibration theory is discussed. General atmospheric radiation theory and atmospheric transmittance codes will be discussed. To understand how atmospheric temperature information can be found from radiance measurements, the radiative transfer

equation and retrieval methods are summarized. Finally, assumptions and limitations to this research effort are presented.

Spectrometer's Components

Figure 1.1 is an external side view of the main components of the BOMEM MR-154 FTIR spectrometer. The tripod and telescope accessories are not included in the drawing. When used, the telescope was attached to the collimator.

There are two aperture wheels that can be used to control the amount of energy allowed to reach the detector. One aperture wheel is located on the collimator. The second aperture wheel is located on top of the spectrometer. For meteorological applications, both aperture wheels were normally set to a diameter of 6.4 mm. Aperture settings were recorded for each measurement, so proper geometric throughput coefficients were applied when calibrating. Caution was needed to ensure the proper aperture setting was selected. On one occasion, a smaller aperture setting actually increased the signal. It was determined infrared energy emitted by the fringe of the aperture opening was included in the incoming signal. Leaving the front aperture at 6.4 mm and adjusting the top aperture wheel eliminated this problem.

Either an MCT or InSb detector was needed for data collection. The term MCT stands for mercury, cadmium, and telluride; and InSb stands for indium antimonide. Both detectors are semiconductors and are responsive to different frequency ranges. The MCT detector was used for data collection in the region from 525 cm^{-1} to 1800 cm^{-1} (or $19\text{ }\mu\text{m}$ to $5.55\text{ }\mu\text{m}$).

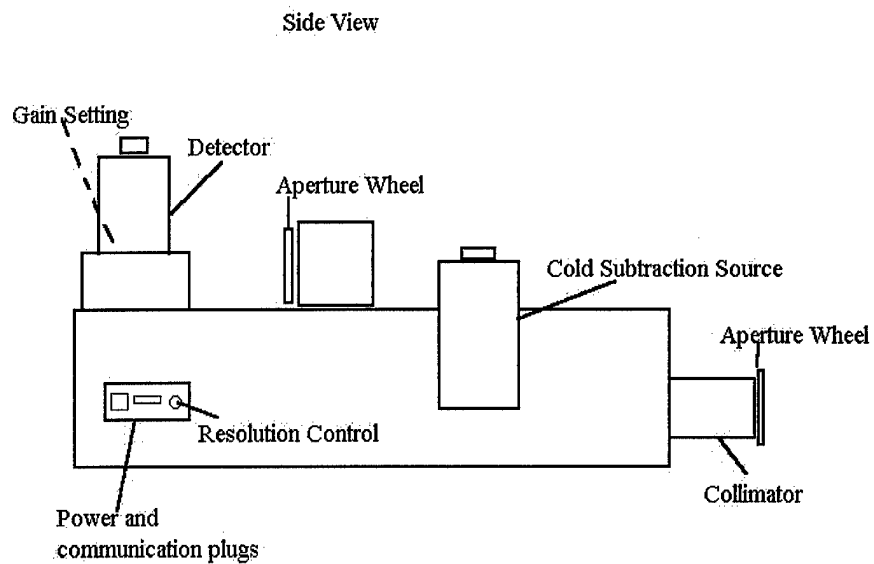


Figure 1.1. Diagram of side view of MR-154 spectrometer with main components labeled.

The InSb detector was normally used for data collection over the 1800 cm^{-1} to 3000 cm^{-1} spectral region ($5.56\text{ }\mu\text{m}$ to $3.33\text{ }\mu\text{m}$) and was useful for collecting data up to 6000 cm^{-1} ($1.67\text{ }\mu\text{m}$) for some applications, such as the one discussed in Part 2 of this thesis.

Detectors were cooled with liquid nitrogen at 77K to reduce the detector noise.

The cold subtraction source reduced the emission of the spectrometer to a negligible level. It was filled with liquid nitrogen to reduce its thermal emission. The telescope attachment, not pictured, is a Cassegrainian telescope with a focal length of 12 cm. It has a narrow field of view of only 5 milliradians or 0.286 degrees. The purpose of the telescope was to focus energy into the aperture. It also served to determine that the desired target was in the field of view. The tripod served as a platform to stabilize and position the instrument. It allowed a 360-degree horizontal rotation and an elevation range of -5 to +45 degrees. Elevations above 45 degrees were not possible since liquid nitrogen would spill out from the detector and cold subtraction source. Resolutions of 1, 2, 4, 8, 16, 32, 64 and 128 cm^{-1} were available.

Principles of Operation

The BOMEM MR-154 Fourier Transform Infrared (FTIR) spectrometer collects highly accurate spectral radiance measurements of clear skies, clouds, industrial emissions, and other desired targets in the infrared spectral region 525 cm^{-1} to 6000 cm^{-1} at resolutions of 1 cm^{-1} to 128 cm^{-1} . Radiance measurements are very useful for characterizing a source based on its emissions, spectral characteristics, and temperature.

Figure 1.2 represents the event sequence from receiving radiant emission from a source scene to creating a calibrated spectral plot. Incoming radiation at point 1 enters

the spectrometer through the aperture, passes through the collimator, and encounters the beamsplitter at point 2. Upon striking the beamsplitter, one portion of the beam is directed towards one corner-cube mirror and another portion of the beam is directed towards a second corner-cube mirror. A rotating arm mounted on a pivot moves the mirrors to cause a phase shift in the beam portions.

When the beams are recombined, the resulting constructive and destructive interference creates a unique interference pattern at point 3. The maximum signal in the middle of the interferogram is called the zero phase difference or ZPD. It signifies the point where the recombined beams are in phase. At point 4, a Fourier Transform is applied to the interferogram resulting in a complex raw spectral plot. A calibration is then applied to the raw spectrum. The calibrated spectral plot is the final product and an example is shown at point 6. This calibrated plot was useful for characterizing its source. Spectral features of the plot can be compared with molecular spectroscopic databases for identification. Also, temperature information can be calculated from radiance values at discrete frequencies or over a spectral region through the Planck function.

The spectrometer was connected to a personal computer by a standard serial cable. The computer ran the Research Acquire software package that operated the spectrometer and performed all necessary data collection and processing applications. The software allowed a user to collect, process, plot, and view data and calibration files; calculate calibration files, radiance files, temperatures, and other products; and, derive textual data from plotted products.

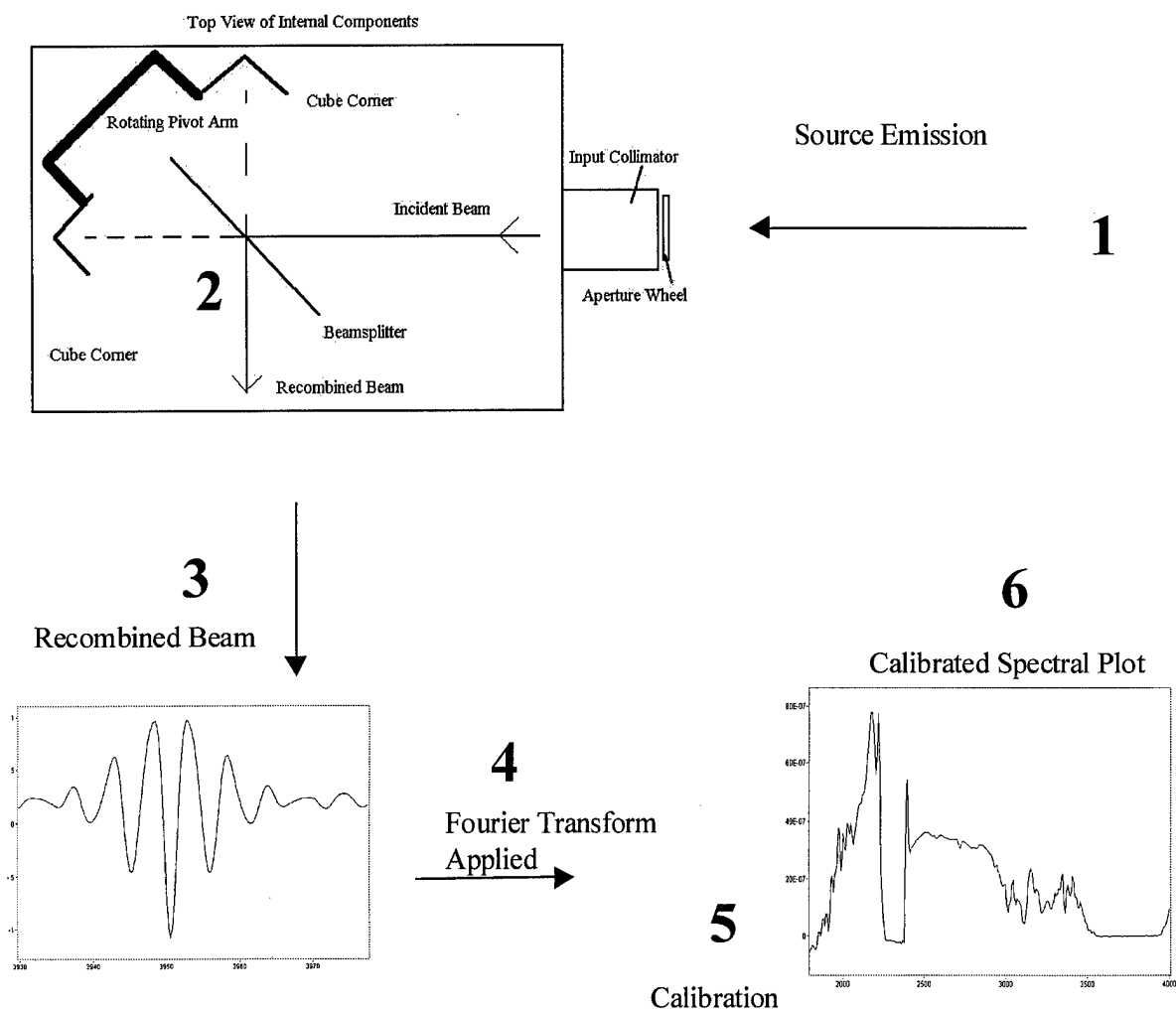


Figure 1.2. Principle of operation of the FTIR spectrometer. Incident energy, 1, enters aperture and encounters beam splitter at point 2. The beam is recombined where constructive and destructive interference result represented by the interferogram at 3. A Fourier Transform is applied to the interferogram and a raw spectrum results. At 5, a calibration process is completed. Finally, a calibrated spectral plot is obtained at point 6 (after BOMEM Users Manual.).

Calibration Theory

Calibration of the data using cold and hot radiometric references was required to account for any stray radiance and offset caused by thermal emission of the spectrometer.

Calibration is the process where a numerical calculation is applied against the raw spectrum as a function of wavelength. An uncalibrated spectrum can be expressed as (BOMEM Users Manual, 1995: 27-30):

$$S(\sigma)=K(\sigma)[L(\sigma)+M(\sigma)]. \quad (1)$$

σ	frequency
$S(\sigma)$	the measured complex spectrum provided by the spectrometer
$K(\sigma)$	the complex instrument response function
$L(\sigma)$	the source spectral radiance
$M(\sigma)$	the spectral power of the stray radiance

Calibration is a two-step process. First, the instrument response is found by solving equation (1) for $K(\sigma)$ for each black body reference. The $S(\sigma)$ term is the radiance observed by the spectrometer while looking at the black body reference. The $L(\sigma)$ term is the theoretical radiance found through the Planck function representing the source radiance of the black body at the temperature setting. For all calibrations, the black body filled the field of view, and the stray radiance $M(\sigma)$ was negligible. A mathematical calculation uses these solved $K(\sigma)$ values to generate a single file used for calibrating raw data. Once the detector response $K(\sigma)$ is known, a raw spectrum can be calibrated. The observed radiance $S(\sigma)$ becomes the unknown source. Applying $K(\sigma)$ to the raw spectrum, the solution $L(\sigma)$ is the calibrated file (BOMEM Users Manual, 1995: 27-30). The result is a calibrated spectrum from which radiance, magnitude, and

temperature can be derived for comparison with other sources, references, or with calculated output from MODTRAN.

Calibration drift includes error associated with the changes in the radiometric gain and offset during the time between when the calibration was done and when the source radiance is observed. Factors that contribute to calibration drift are electrical gain, stability of detector responsivity, and the ambient temperature (BOMEM Users Manual, 1995: 33-34).

Atmospheric Radiation Theory

Scientists, at what was then known as the Air Force Geophysics Lab (AFGL), assembled an archive of spectral signatures of selected atmospheric gases. Today, this information has evolved into the HITRAN 1996 molecular database available on CD. Figures 1.3a through 1.3d were generated with the HITRAN 1996 CD. Figure 1.3a displays intensity due to the combined effects of CO₂, H₂O, and N₂O. Figures 1.3b through 1.3d display the individual emission patterns of the CO₂, H₂O, and N₂O molecules respectively. Even on this low-resolution plot, differences between intensity bands of the CO₂, H₂O, and N₂O molecules are noted. In principle, it is this difference in the emission features between the molecules that allows source characterization. It would be useful to look at why these patterns are different.

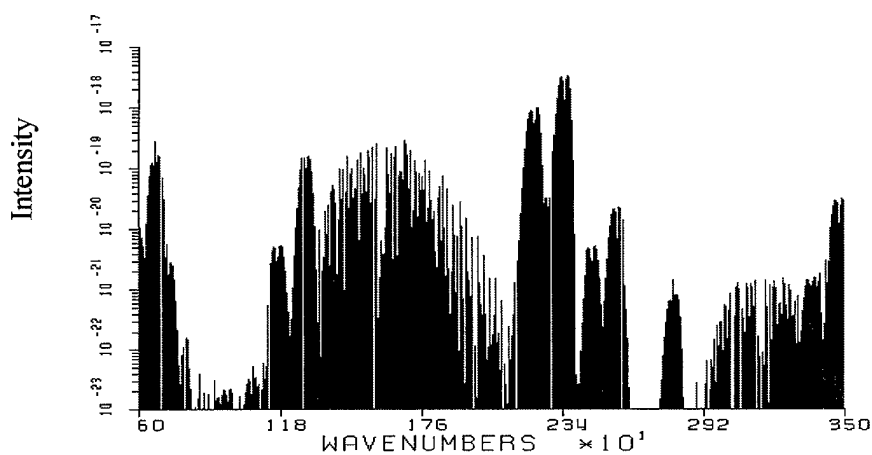


Figure 1.3a. Combined atmospheric radiance due to water vapor, carbon dioxide, and nitrous oxide. The plot was generated along the spectral band from 600 to 3500 cm^{-1} using HITRAN 1996.

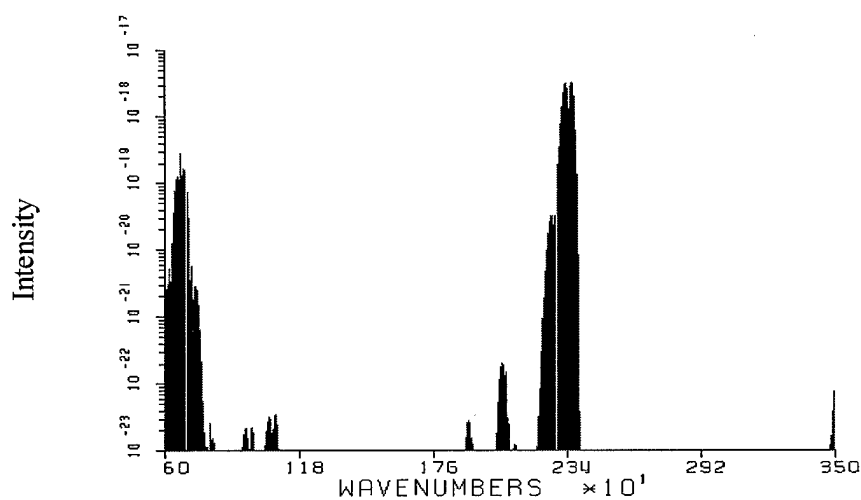


Figure 1.3b. Atmospheric radiance due to carbon dioxide. Calculated using HITRAN.

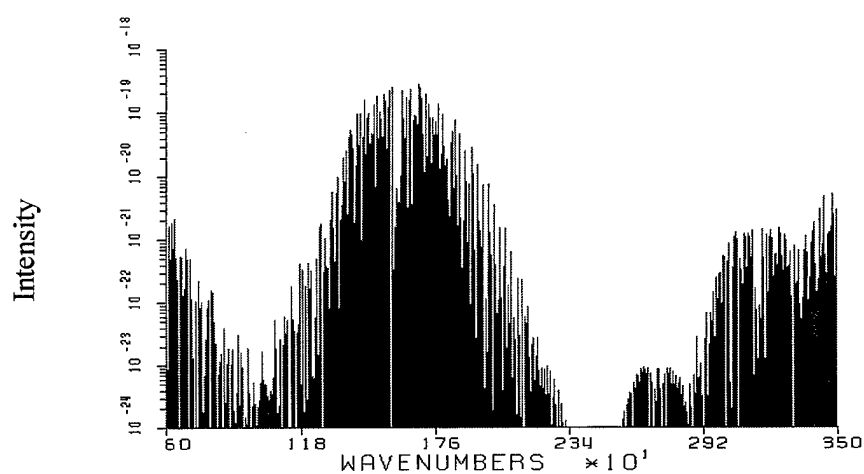


Figure 1.3c. Atmospheric radiance due to water vapor. Calculated using HITRAN 1996.

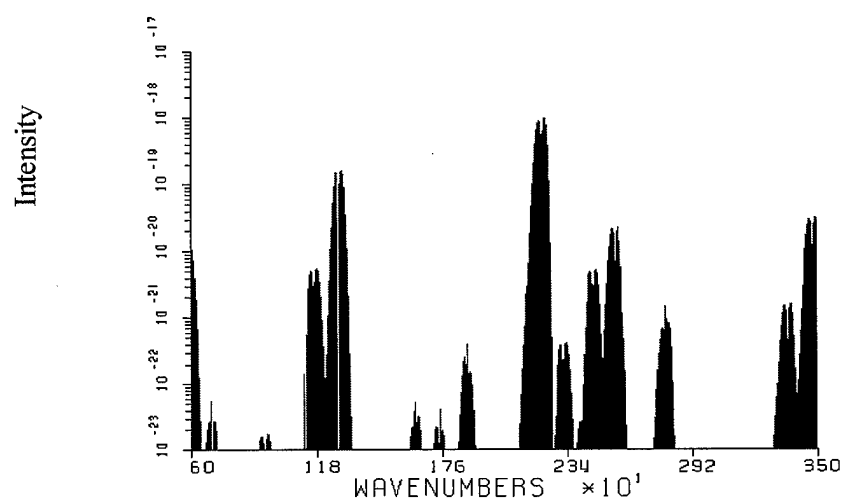


Figure 1.3d. Atmospheric radiance due to nitrous oxide. Calculated using HITRAN 1996.

Radiation can interact with atmospheric gases in five ways: ionization-dissociation interactions, electronic transitions, vibrational transitions, rotational transitions, and forbidden transitions (Kidder and Vonder Haar, 1995: 68). The vibrational transitions are the most important for the applications considered here.

The two chief absorbers in the infrared region of the spectrum are CO_2 and H_2O . Their vibrational modes are shown in Figure 1.4a and 1.4b. Note that CO_2 has three vibrational modes, but in Figure 1.3b there are only two bands shown. The vibrational modes associated with the ν_2 mode at 668 cm^{-1} or $15\text{ }\mu\text{m}$ and the ν_3 mode at 2349 cm^{-1} or $4.3\text{ }\mu\text{m}$ appear in Figure 1.3b. The ν_1 vibrational mode of the CO_2 molecule is inactive at 1340 cm^{-1} or $7.46\text{ }\mu\text{m}$, because the ν_1 mode has no electric dipole moment. If a vibrational mode does not have a dipole moment, the electric field of incident radiation cannot interact with the molecule. More specifically, the spectrometer will not detect emission from that molecule in that spectral region. Lack of electric dipole moment is also why the two most abundant gases in the atmosphere, *i.e.*, O_2 and N_2 , are transparent in the infrared (Kidder and Vonder Haar, 1995: 68).

Even though molecules absorb and emit at unique spectral bands associated with vibrational modes, when observed as a whole such as a radiance measurement of the atmosphere, patterns between various molecules overlap. This can create a problem with accurately characterizing a source depending on the intensity of the bands that overlap. To minimize this problem, careful consideration must be given as to which band to use. For instance, there are strong water vapor absorption bands in the $15\text{ }\mu\text{m}$ CO_2 band but not in the $4.3\text{ }\mu\text{m}$ CO_2 . For this reason, the latter was considered here for the physical retrieval problem.

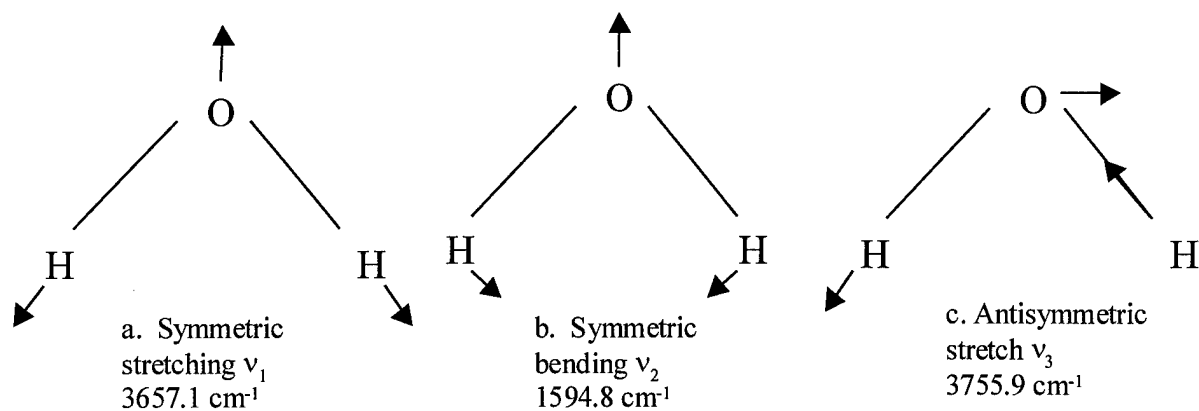


Figure 1.4a. Vibration modes of the water vapor molecule (after Kidder and Vonder Haar).

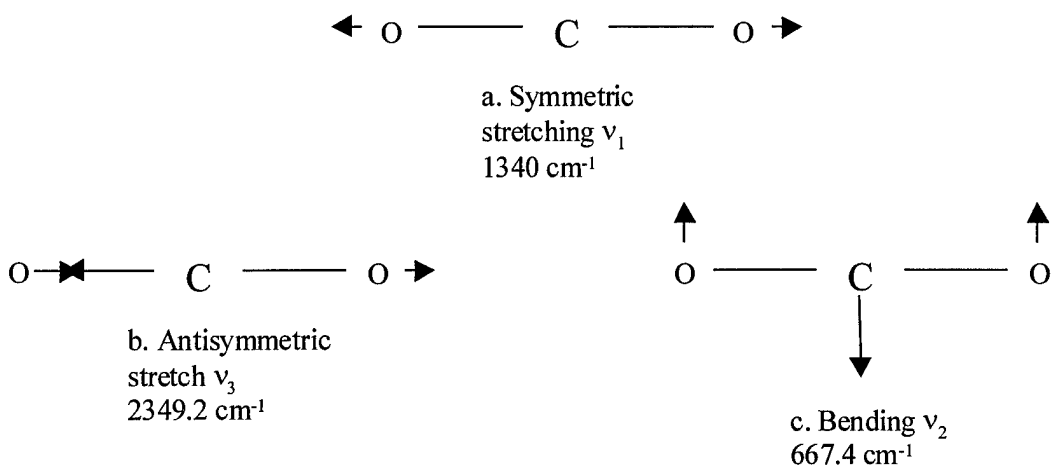


Figure 1.4b. Vibration modes of the carbon dioxide molecule (after Kidder and Vonder Haar).

The Moderate Resolution Transmittance Model (MODTRAN)

A brief description of MODTRAN is needed to understand the methodology used in the physical retrieval method attempted to determine vertical profiles from radiance and for validating the model output. Specifically, the model was used to calculate atmospheric radiance for similar meteorological conditions and viewing angles for comparison with that observed by the spectrometer. MODTRAN was also used to calculate atmospheric transmittances needed to determine the kernel function in Equation (2). This process will be covered in more detail in the Methodology section.

An in-depth description of MODTRAN is found in GL -TR-89-0122. The detail provided in that document is not needed here. A basic understanding of the model is sufficient.

What was then named the Air Force Cambridge Research Laboratory (AFCRL) developed a set of atmospheric propagation codes for Department of Defense (DoD) electrooptical systems. With these codes, atmospheric transmittance and radiance could be calculated to estimate atmospheric effects on electrooptic systems. These models considerably enhanced both the design of DoD systems and their operational performance (Liebowitz, 1990: 1).

Simply put, MODTRAN is a band model based on empirical transmission functions and effective absorption coefficients derived from laboratory experiments. It evolved from LOWTRAN 7, the Low Resolution Transmittance Model, as user needs changed requiring higher resolution atmospheric models. The model's functions are coupled with a detailed database (*i.e.*, HITRAN 1996) containing thousands of spectral lines of common and rare atmospheric constituents. As a band model, transmittance and radiance

values are calculated as an average over a bin of 1 cm^{-1} width (Anderson and others, 1994: 1-2).

The model MODTRAN is available on a CD called Phillips Laboratory Expert-assisted User Software (PLEXUS, 1996). PLEXUS provides a user-friendly interface with MODTRAN and other atmospheric transmission models. With PLEXUS, users can select a variety of meteorological parameters, paths, and other inputs to determine atmospheric radiance and transmittance. The output is atmospheric radiance in units of $\text{W/cm}^2 \text{ sr}^{-1} \text{ cm}^{-1}$ and transmittance is in percent. An example is provided in Figures 1.5a and 1.5b. There are two versions of PLEXUS, version 2.1b and 3.0 beta. The advantage of PLEXUS 3.0 beta is that it incorporates the latest version of MODTRAN and the HITRAN 1996 database. The disadvantage is that it is a beta version, so problems with the software may have not yet been detected. The advantage of PLEXUS 2.1b is that it is validated software and includes the prototype of the user-defined atmosphere (UDA) functionality. The UDA allows a user to calculate atmospheric transmittance and radiance using an observed temperature profiles. In PLEXUS 3.0, the UDA function is not currently available. A disadvantage of the UDA software is that it is a prototype and has not been benchmarked by the software developer, so caution must be exercised when using the UDA functionality. In this research effort, PLEXUS 2.1b with UDA was used allowing calibrated radiance measurements to be compared with calculated radiance data from MODTRAN using representative atmospheric profiles.

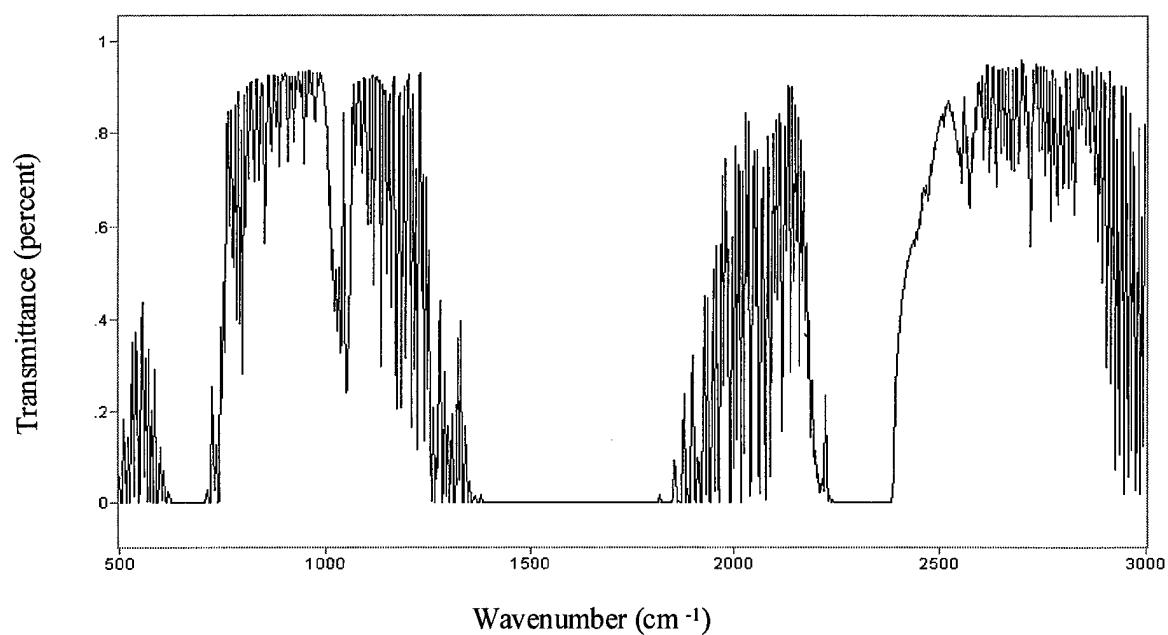


Figure 1.5a. Atmospheric transmittance plot generated by MODTRAN using PLEXUS 2.1b. Viewing angle is 020 degrees at 45 degrees elevation in mid January on a clear day.

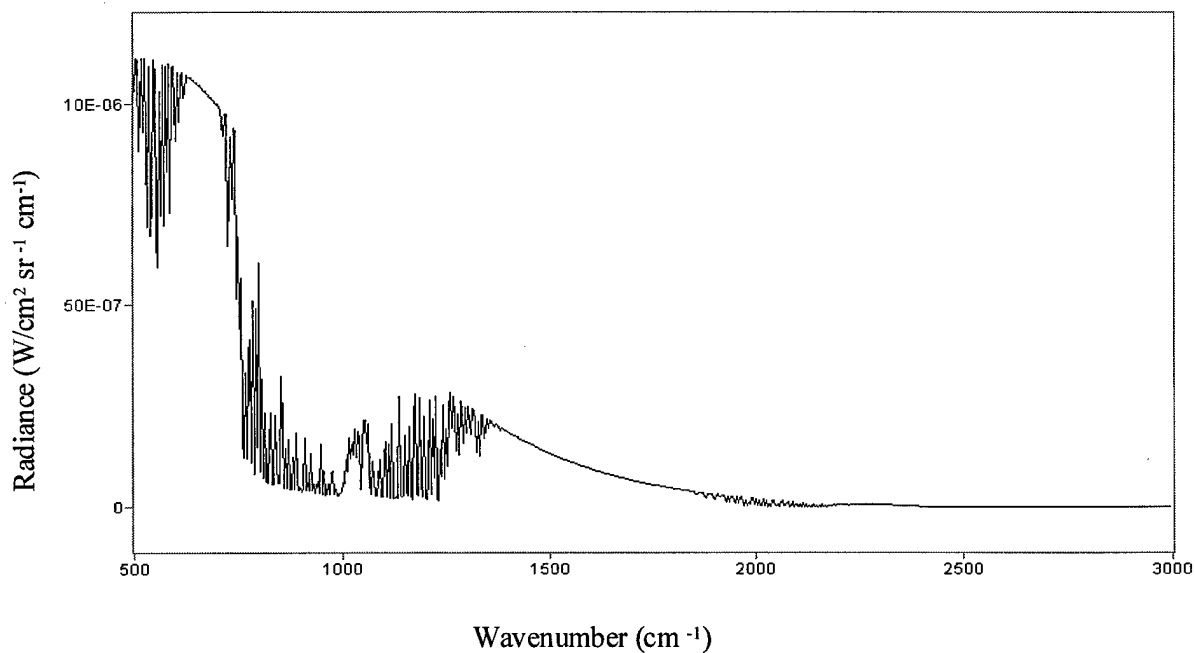


Figure 1.5b. Atmospheric radiance plot associated with Figure 1.6a.

Radiative Transfer Equation and Retrieval Methods

To determine atmospheric temperature and moisture information from observed radiance Kidder and Vonder Haar see the physical problem as determining the temperature and trace gas concentration profiles that could have produced a set of observed radiances. This is called the inverse problem or retrieval problem. The opposite of this, the forward problem, is calculating the atmospheric radiance given an atmospheric temperature and moisture profile.

Retrieval methods can be grouped into three general areas. They are the physical retrieval, statistical retrieval, and hybrid retrieval. A physical retrieval uses the radiative transfer equation similar to that shown below (after Goody and Yung, 1989).

$$I(\sigma) = \int_0^{\infty} B[\Theta(z)] \frac{\partial T(z, \sigma)}{\partial z} dz. \quad (2)$$

The term on the left is the observed radiance provided by the spectrometer. This term represents radiance (I) as a function of wavenumber or frequency (σ). The vertical temperature information as a function of height is identified by the term $B[\Theta(z)]$ and is the unknown function to be solved for. The second term on the right is the kernel or weighting function. This weighting function represents the change in atmospheric transmittance over a height or path length as a function of frequency (Goody and Yung, 1989: 259-261).

In the statistical method, the radiative transfer equation is not directly used. Several years' worth of observed atmospheric profiles are run through an atmospheric model to calculate radiance. The result is a set of data pairs of observed profiles and calculated radiances. An observed radiance measurement is iteratively compared to the data set

until a match is found and considered to be the solution (Kidder and Vonder Haar, 1995: 193-194).

Hybrid retrieval methods fall in between the physical and statistical retrievals. They appear like the statistical method but do not require the large database. They use weighting functions like a physical approach but do not involve integration of the radiative transfer equation (Kidder and Vonder Haar, 1995: 195).

This research effort attempted to develop a physical retrieval method to solve the inverse problem. That is, given a calibrated radiance file collected by the spectrometer, use the physical method to retrieve the temperature and moisture profile. The approach used here to retrieve thermal and moisture information from radiance is discussed more in the Methodology section.

Environmental Monitoring

Part-1 of this thesis dealt mostly with meteorological applications, however the spectrometer's environmental monitoring capability was demonstrated. Emissions from the Wright-Patterson AFB Area B coal-burning plant were analyzed. Observed spectral features were compared with the HITRAN 1996 database and other references and were identified (Herget, 1981: 635).

Assumptions and Limitations

The equipment used for the meteorological applications investigated was not ideally suited for this effort. The spectrometer did not have the optional thermal stabilizer, there was no capability for zenith viewing, and the time required by the black body to stabilize

allowed only one calibration file to be collected during each data collection period which may have lasted one or more hours.

The first and third limitation effected the data accuracy. Considering an hour or more elapsed between the time when the cold and hot black body references were collected, the ambient temperature changed. This likely contributed to calibration drift error.

The spectrometer could not collect data at elevation angles greater than 45 degrees, because liquid nitrogen would spill out of the detector and cold subtraction source. An apparatus was built from lab clamps designed to place a mirror in front of the aperture at a 45-degree angle while the spectrometer was resting horizontally on the tripod. The problems observed with this apparatus are discussed in more detail in the Methodology.

A further limitation was that only one detector could be used at a time. The MCT detector was used for the spectral region from 500 cm^{-1} to 1800 cm^{-1} . The InSb detector was used to observe 1800 cm^{-1} to 6000 cm^{-1} . This did not result in any error to the data, but it did limit the spectral region observed at any one time. An option provided by the manufacturer allows both detectors to be used at one time so the entire 500 cm^{-1} to 6000 cm^{-1} band could be observed simultaneously.

There were limitations with using MODTRAN. The version of MODTRAN used in PLEXUS 2.1b was validated by comparing output with another atmospheric model, but there was no comparison with observations. Although in MODTRAN a user can select input for aerosol, type of environment, or standard atmosphere, the choices allowed cannot possibly resemble all actual atmospheric states. A perfect match between observed and calculated data was not likely, but it was reasonable to expect the shapes and characteristics of the two plots to be similar. The User-Defined Atmosphere (UDA)

prototype software capability was provided to only a select few Air Force agencies. The software developer did not have the funds to verify the UDA and accepting the possibility that the UDA functionality may have errors, they are cautious with whom they send it to. The UDA was used here with limitations accepted.

II. Literature Review

The literature review focused on previous work to retrieve atmospheric profiles from ground-based observed radiance, validate atmospheric transmittance models, and characterize smokestack emissions from spectrometric data.

The spatial and temporal resolution of upper air data is very coarse and not standardized when the global scale is considered. For example, there are only about 90 rawinsonde sites in the United States and these sites collect profiles only twice a day (*i.e.*, 0000 UTC and 1200 UTC). The worldwide standard for collecting atmospheric profiles is the balloon-borne rawinsonde sensor, but not all nations' weather services use the same rawinsonde sensors. The rawinsonde measures atmospheric temperature, moisture, wind speed and direction as a function of observed pressure and transmits the data to a ground receiver. Collecting rawinsonde data is time consuming and costly (Stankov, 1998: 1835-1837).

A goal of the Multisensor Retrieval of Atmospheric Properties (MRAP) project is to develop a means to remotely measure atmospheric information to reduce labor costs and standardize the data. The MRAP program is working towards developing an array of passive sensors to remotely retrieve atmospheric data (*i.e.*, wind speed and direction, temperature, and dewpoint) that is currently measured by rawinsondes. If successful, MRAP would also increase the spatial and temporal resolution of vertical atmospheric data. Instead of receiving data from rawinsondes once every 12 hours, a profile converted from radiance could be retrieved as often as desired *e.g.*, every ten minutes (Stankov, 1998: 1835).

Researchers at the University of Wisconsin--Madison have led the way in retrieving atmospheric temperature and moisture profiles from ground-based radiance measurements collected by a spectrometer. Using a statistical method, they have retrieved atmospheric profiles from radiance data collected by a BOMEM 100-series spectrometer. Their instrument is called the Atmospheric Emitted Radiance Interferometer (AERI). The AERI system is fully automated and capable of providing spectra at 10-minute intervals at better than 1 cm^{-1} resolution. These radiances contain valuable information about the vertical thermal and moisture structure of the atmosphere up to a height of 3 km (Feltz and others, 1998: 857).

The work done by the University of Wisconsin-Madison researchers is well documented and is summarized here. Readers desiring additional information about AERI are highly encouraged to visit the AERI homepage located at <http://cimss.ssec.wisc.edu/aeriwww/aeri/>. This web page has an abundance of information, publications, and graphics not available elsewhere that sometimes appears there in advance of publication in journals.

Smith and other researchers proposed to use ground-based observed radiance to retrieve atmospheric temperature and moisture profiles (Smith, 1970: 1993). The first promising results of this proposal came in 1988 during the Ground-based Atmospheric Profiling Experiment (GAPEX) as described below. The HIS instrument is the precursor to the AERI system.

During the week of 29 October 1988 to 4 November 1988, a Ground-based Atmospheric Profiling Experiment (GAPEX) was conducted at Denver Stapleton International Airport. The objective of GAPEX was to acquire and analyze atmospheric temperature and moisture profile data from state-of-the-art remote sensors. The sensors included a six-spectral-channel, passive Microwave Profiler (MWP), a passive, infrared High-Resolution Interferometer Sounder (HIS) that provides more than 1500 spectral channels, and an active Radio Acoustic Sounding System (RASS). The HIS instrument used in GAPEX is a Michelson interferometer developed primarily as an aircraft prototype of a new-generation satellite sounder. It operates in the region between 600 and 2600 wavenumbers (*i.e.*, 16.8-3.8 μm) using three detectors to divide the spectrum into three bands (Smith and others, 1990: 311-312).

The analysis of the HIS data showed promise for retrieving atmospheric profiles from radiance information gathered by a ground-based spectrometer. Smith believed the next step was to develop a method to retrieve atmospheric information, regardless of cloud cover, using a combination of HIS, MWP, and RASS measurements (Smith and others, 1990: 317).

Six months of AERI data and coincident rawinsonde data were collected and compared. Excellent agreement between AERI's retrieved atmospheric information and rawinsonde measurements was reported (Feltz and others, 1998: 857). An AERI configuration comprised of a BOMEM-100 Michelson interferometer collected an uncalibrated raw spectrum every two seconds and averaged them over a three-minute time period. Data were calibrated using black body references of 333 K and the ambient temperature. The temperature profile was retrieved from the 620-720 cm^{-1} spectral region of the 15 μm CO_2 absorption band up to 3 km above the ground (Feltz and others, 1998: 858-859). The method worked under a clear sky or below cloud bases during

meteorological conditions with no precipitation. The retrieval technique is described next.

The AERI retrieval is accomplished in two steps. 1) an initial temperature and water vapor profile is obtained by statistical regression based on a 2-yr collection of rawinsondes and 2) an iterative recursive physical solution of the radiative transfer equation is conducted using the results of step 1 as the initial profile to yield a final measure of the temperature and water vapor profile... A fast forward model calculation of spectral radiance as would be observed by AERI is performed for each radiosonde case to provide a radiosonde-radiance spectrum pair for the statistical regression analysis. A regression analysis is then applied to relate these theoretical calculations of radiance and the matching radiosonde temperature and water vapor profiles (Feltz and others, 1998: 859).

A retrieval technique described in detail by Smith is slated for publication in the March 1999 edition of the Journal of Atmospheric and Oceanic Technology.

In GL-TR-89-0122, the method of validating the atmospheric model MODTRAN against Low Resolution Transmittance Code (LOWTRAN) and the Fast Atmospheric Signature Code (FASCODE) was presented. Basically, the GL validated MODTRAN by comparing plots of atmospheric absorption, transmittance, and radiance for selected meteorological parameters and viewing angles against LOWTRAN and FASCODE calculations using the same parameters (Berk and others, 1989: 25-26).

Through the years, U.S. government and military agencies have contributed to the development of atmospheric models by comparing modeled output with theoretical and experimental results (Anderson and others, 1994: 1-2). These efforts will not be discussed here. It was hoped this research would add to the contribution.

III. Methodology

Summary

This section covers the method used to collect and calibrate the data. In general, the method discussed is valid for collection of data with the spectrometer whether for meteorological, environmental, or military applications. This section also explains how the kernel functions were calculated and the physical retrieval process attempted. Finally, the model validation method is discussed.

Data Collection and Calibration Technique

Once the desired target (*e.g.*, clear sky or smokestack emission) was selected and weather conditions were favorable (*e.g.*, no lightning storms or precipitation), the spectrometer was moved to the roof of Building 640 located on the Air Force Institute of Technology campus. Once outside, the spectrometer was allowed to stabilize (45 or so minutes) to the ambient conditions to decrease any calibration drift error. Either the MCT (mercury, cadmium, telluride) or InSb (indium antimonide) detector was attached. The cold subtraction source was attached to the emission port. The detector and cold source were filled with liquid nitrogen and were allowed to stabilize for approximately 15 minutes also to decrease calibration drift errors. Normally, the equipment was set up an hour prior to taking the first measurement.

Gain and aperture settings were selected based on the estimated black body temperature of the target. The resolution selected was based on the level of desired

detail. Generally, the gain was full, the aperture was at diameter of 6.4 mm, and the resolution was 1 cm^{-1} for meteorological and environmental targets.

The black body was set to a cold reference temperature (T_{cold}) that was below the estimated temperature of the target. Normally the selected T_{cold} was 0°C , which was the lowest temperature the black body could produce. Once the black body stabilized to T_{cold} , it was aligned directly in front of the aperture on the collimator of the spectrometer. This filled the spectrometer's field of view essentially eliminating stray radiance and the $M(\sigma)$ term in Equation (1). The reference at T_{cold} was collected. The black body was reset to a hot reference temperature (T_{hot}) that was higher than the estimated black body temperature of the target. For meteorological targets, a cold reference point of 0°C and hot reference of 30°C was usually appropriate.

Data were collected of the atmosphere along the azimuths and elevations desired. A radiance measurement was comprised of one or the average of up to 100 scans. Through experience and comparison of radiance measurements, it became apparent that there was generally no benefit in having more than 25 scans per radiance measurement file. The time interval between each scan was dependent on the resolution selected. At a resolution of 1 cm^{-1} , a scan was collected about every two seconds, so it took about 50 seconds to collect one measurement comprised of the average of 25 scans.

After the black body stabilized to T_{hot} , the calibration point was collected. Once both calibration points and the data were collected, either additional data were collected, or the equipment was taken down and returned to the lab. Data analysis could take place any time after the raw data and calibration files were collected.

A calibration file was quickly and easily calculated by entering the T_{hot} and T_{cold} reference files under the Compute Radiometric Correction function in the Research Acquire software. The resulting calibration file could then be applied to a raw spectrum, again using the Research Acquire software. The result was a calibrated radiance file ready for the physical retrieval, model validation, or determination of constituent gases from the source.

The method for selecting the meteorological conditions to observe was designed to maximize opportunity and minimize effort. Data were collected during some transition, so more than one condition was observed for each time the spectrometer was set up. For example, data was collected over time from when stratus covered the sky until it dissipated to compare radiance from an overcast and clear sky. In another case, data collection from dawn to daylight was done to see how radiance varied as the sunlight increased.

Determining the Kernel Functions

Recall from the "Radiative Transfer Equation and Retrieval Methods" section that the kernel functions were needed for the physical retrieval method. The kernel function represents the change in atmospheric transmittance over the change in path distance for a finite spectral interval along a unique viewing angle.

There are empirical methods of calculating atmospheric transmittance, however MODTRAN was used here to calculate atmospheric transmittance values for different path lengths along one viewing angle. The procedure for calculating these kernel functions was as follows.

All of the model inputs for MODTRAN were kept constant except the path length. The meteorological conditions input were clear sky, visibility of 23 km, no clouds, and no precipitation. The mid-latitude winter atmospheric model resident in MODTRAN was used. The geometry of the path was a 45-degree elevation angle looking towards the north. Calculations were made within the $4.3\ \mu\text{m}$ CO_2 absorption band over the spectral region from $2250\ \text{cm}^{-1}$ to $2400\ \text{cm}^{-1}$ for every $1\ \text{cm}^{-1}$. Other input parameters were latitude 39.781N and longitude 84.081W ; sensor altitude 300 m; default stratospheric background and solar activity; and, a CO_2 concentration of 360 ppm.

The transmittance for a path length of zero was assumed to be one for all frequencies. The first MODTRAN calculation determined transmittance from the sensor at the surface along the path for a distance of 10 m. The next calculation was made along that same viewing angle for a path length of 20 m, then 30 m, *etc.* to 4000 m. The calculations were done at intervals of 10 m out to a path length of 100 m, then by intervals of 100 m out to 1000 m, and finally by intervals of 1000 m out to 4000 m. Data from each calculation were input into a worksheet and sorted by wavenumber.

Although transmittance was calculated from 2250 to $2400\ \text{cm}^{-1}$ at $1\ \text{cm}^{-1}$ intervals, not all of this data was desired. The number of frequencies selected had to coincide with the same number of altitudes for which temperature information was desired. This will be discussed in the next section.

For the retrieval here, only ten frequencies were selected based on the thickness of atmosphere sampled by that frequency. For instance, look at Table 1. The transmittance values for $2305\ \text{cm}^{-1}$ fall to almost zero by 100 m, while the transmittance extends well

beyond 100 m at 2388 cm^{-1} . This demonstrates the point that different frequencies sample different thicknesses of the atmosphere.

The ten frequencies selected for the retrieval were 2309, 2310, 2311, 2314, 2316, 2318, 2322, 2326, 2335, and 2377 cm^{-1} , because they sampled the lowest 1000 m of the atmosphere. The frequencies shown in Tables 1 and 2 were not from those ten above.

Next, the kernel functions were calculated by determining the change in transmittance over the change in path length. For instance, at 2252 cm^{-1} , the transmittance for a 20 m path was 0.851 and for a 30 m path was 0.793. The resulting value for the kernel function at that point becomes $(0.851-0.793)/(30\text{m}-20\text{m})$ or 0.0058 m^{-1} . This simple calculation was done for each interval and each frequency and example output is shown in Table 2.

Table 1. Example worksheet of atmospheric transmittance values generated for discrete frequencies for specific path lengths.

Path Length (m)	Wavenumber			
	2252 cm^{-1}	2272 cm^{-1}	2305 cm^{-1}	2388 cm^{-1}
0	1.000	1.000	1.000	1.000
10	0.919	0.763	0.318	0.978
20	0.851	0.614	0.155	0.958
30	0.793	0.510	0.088	0.938
40	0.743	0.434	0.055	0.920
50	0.699	0.375	0.036	0.902
60	0.660	0.328	0.024	0.885
70	0.625	0.290	0.017	0.869
80	0.593	0.258	0.012	0.854
90	0.565	0.232	0.009	0.839
100	0.539	0.209	0.007	0.824

Table 2. Example worksheet of kernel functions found from transmittances calculated in Table 1.

Change in path length (m)	Wavenumber			
	2252 cm ⁻¹	2272 cm ⁻¹	2305 cm ⁻¹	2388 cm ⁻¹
0.1	0.00889	0.03000	0.14556	0.00222
10	0.00680	0.01490	0.01630	0.00200
20	0.00580	0.01040	0.00670	0.00200
30	0.00500	0.00760	0.00330	0.00180
40	0.00440	0.00590	0.00190	0.00180
50	0.00390	0.00470	0.00120	0.00170
60	0.00350	0.00380	0.00070	0.00160
70	0.00320	0.00320	0.00050	0.00150
80	0.00280	0.00260	0.00032	0.00150
90	0.00260	0.00230	0.00023	0.00150
100	0.00177	0.00117	0.00006	0.00121

Once the kernel functions were calculated, they were plotted as in Figure 1.6a. All kernel functions calculated from the surface looking up were a maximum at the surface. In contrast, kernel functions calculated from 45 km altitude looking down are shown in Figure 1.6b. The Results section will discuss in greater detail why the kernel functions were computed for both uplooking and downlooking scenarios. In short, no reference material provided examples of kernel functions for surface sensors. When the kernel functions for ground-based viewing as shown in Figure 1.6a were found, they did not look like kernel functions seen in reference material. It was not known if the method used here was a valid way to determine kernel functions. Then, kernel functions were calculated from 45 km looking down. The result in Figure 1.6b agreed with the reference material, so the method was considered valid and the reason for the difference between the two was examined.

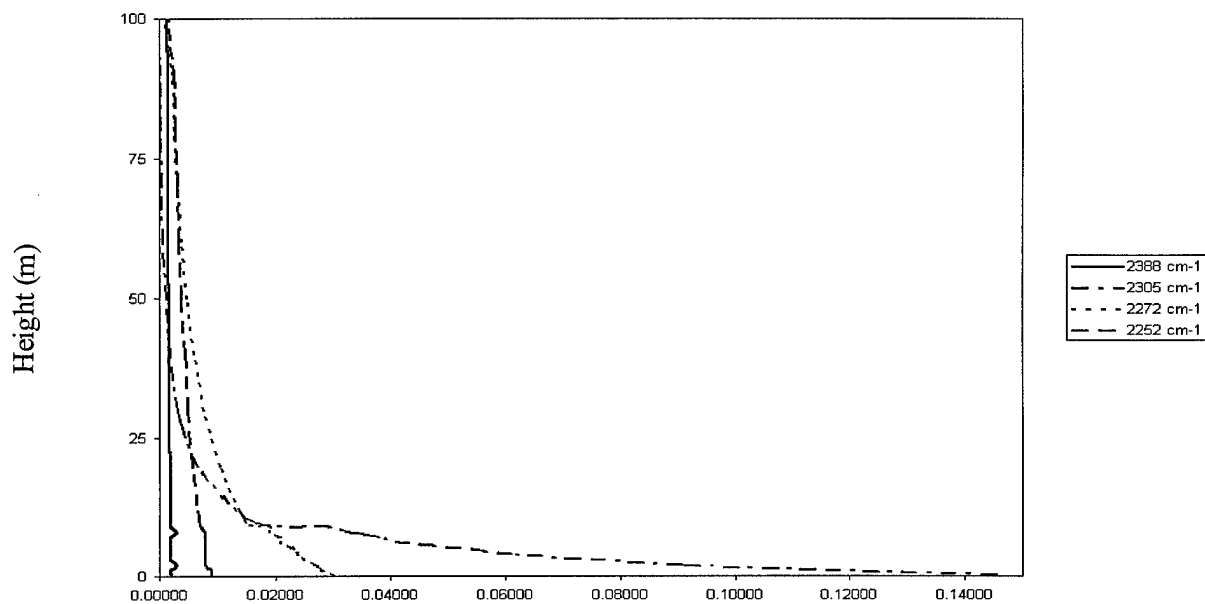


Figure 1.6a. Kernel functions calculated from the surface looking up for selected wavenumbers by height (m).

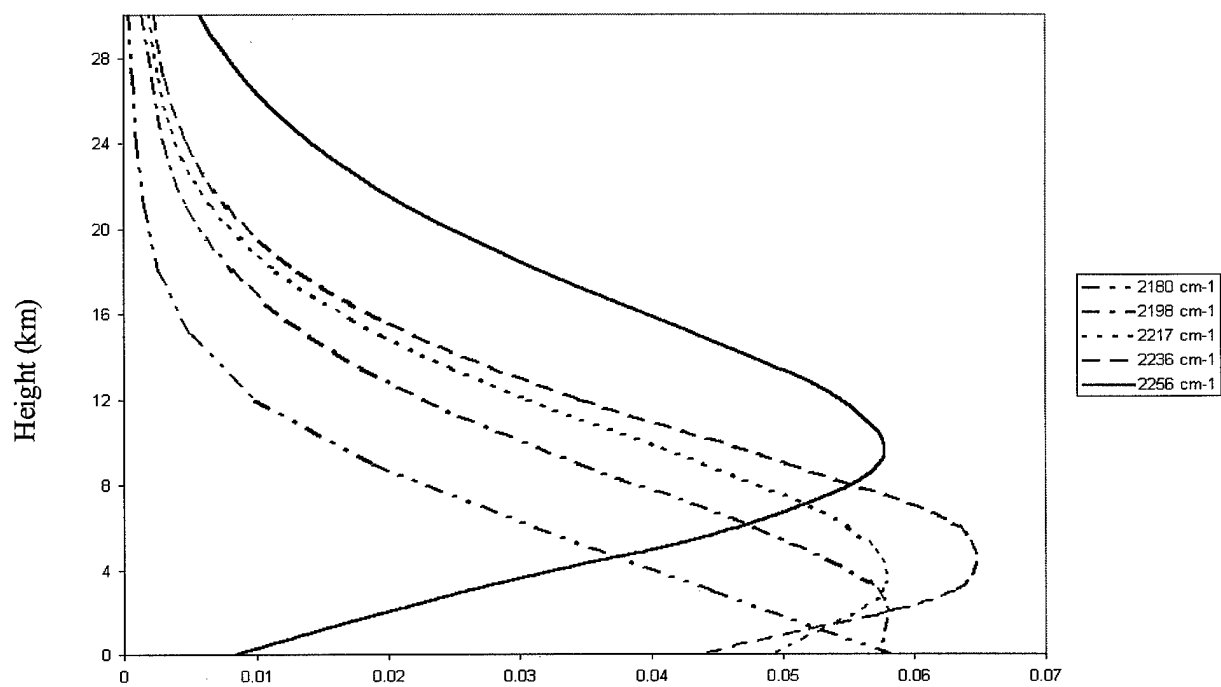


Figure 1.6b. Kernel functions calculated from 45 km altitude looking down for selected wavenumbers by height (m).

The Physical Retrieval

The physical retrieval method attempted to find a least-squares solution for atmospheric temperature from observed radiance. The equation below was taken from Goody and Yung (after Goody and Yung, 1989: 275):

$$x=(W^TW)^{-1}W^Ty \quad (3).$$

x	the retrieved radiance profile from which temperature information is extracted
W	kernel functions for the frequencies used in the retrieval
W^T	transpose of W
y	observed radiance as a function of frequency

The term W, or kernel function, was transposed to find the least-squares solution, so a symmetrical matrix was required to facilitate this. For instance, the solution could not find 12 levels of temperature information with only 10 frequencies. Additionally, the matrix could not be too unusually large either. Meaning, it would not necessarily be an easy task to try to retrieve temperature information at 200 levels using 200 frequencies.

Model Validation

Model validation involved qualitatively comparing observed, calibrated radiance files to MODTRAN calculated values for similar viewing angles and meteorological conditions. Radiance data were collected and calibrated as discussed previously under Methodology, then atmospheric radiance was calculated using MODTRAN with input parameters similar to observed conditions and reformatted rawinsonde soundings.

Surface weather observations were not recorded from the site where the radiance measurements were collected, however hourly observations from the weather stations at Wright-Patterson AFB and the Dayton Airport were saved and are listed in Appendix 1.

These observations could not be included in MODTRAN calculations, but the representative conditions could be considered to select the appropriate MODTRAN input parameters. The nearest rawinsonde site is the National Weather Service Office at Wilmington, Ohio approximately 30 miles south-southeast of the location where the spectrometric data were collected. Rawinsonde data was available only at standard collection times of 0000 and 1200 UTC daily. Rawinsonde data is listed in Appendix 1. Rawinsonde data could be used in the PLEXUS version of MODTRAN only after converting it into the format required by the User-Defined Atmosphere functionality. Once this was done, the MODTRAN calculations were made. Calculated and observed plots were qualitatively compared.

It was desired that the data be collected from directly above the spectrometer. To obtain zenith viewing, lab clamps were used to position a silver-plated lab mirror in front of the aperture. Positioning the mirror at a 45-degree angle while the spectrometer was horizontal to the ground allowed a view of local zenith. After several measurements were taken, it was noted that data collected with the mirror were not consistent with data collected without the mirror. The mirror was positioned at a 22-degree angle so an elevation angle of 44 degrees was obtained. The mirror was removed and the tripod was set so the spectrometer viewed the same 44-degree elevation. The radiance was observed to be higher in the measurements taken with the mirror in place. If the mirror did not affect the incoming signal, the two measurements would have been the same.

It was later determined in the lab that the mirror and clamps behaved like a black body and contributed to the source signal. In the lab, the mirror was attached to the spectrometer in the same manner as above. A 300-watt light bulb was placed 12 inches

from the spectrometer and away from the aperture. This heat source served to simulate sunshine from a high elevation angle. The spectrometer was set to continuously display the voltage of the incoming signal. After a few moments, the intensity of the signal started to increase. The light was removed and the signal fell to the original level. The light was again placed near the spectrometer after the mirror and clamps were removed. There was no observed increase in signal. It was concluded that the mirror and clamps made significant and undesired contributions to the incoming signal. To eliminate this, the mirror was no longer used. Radiance data were collected with the spectrometer at elevations of 0 to 45 degrees. Although zenith viewing was desired, it was not required. MODTRAN calculated radiance for any viewing angle the spectrometer would observe.

Data for the first model validation case was gathered as a stratus layer dissipated from the late morning to early afternoon of 5 October 1998. The purpose was to observe the change in radiance of the sky as an overcast stratus cloud layer dissipated. Data was collected using the MCT detector in the spectral region from 500 to 2000 cm^{-1} at 1 cm^{-1} resolution. Measurements were averaged over 50 scans and were collected at 5-minute intervals. The first scan was taken when the sky was overcast, and the last scan was taken after the stratus dissipated. A two-point calibration with reference temperatures of 0 °C and 30 °C were used to calibrate the data. The radiance measurements were plotted and compared.

The second case on 20 October 1998 compared the change in observed and modeled radiance measurements collected every 3 to 5 minutes from approximately 0700 to 0945 local daylight savings time. It was desired to see how the radiance changed during a sunrise event. The spectrometer was directed towards an azimuth of 230 degrees at an

elevation of 45 degrees to avoid direct sunlight. A two-point calibration with reference temperatures of 0 °C and 30 °C were used to calibrate the data. The MCT detector was used at 1 cm⁻¹ resolution. Radiance measurements were plotted and compared.

Data were collected on 11 November 1998 from three elevation angles at three azimuths for a total of nine viewing angles. The case was designed to compare radiance measurements from different quadrants and elevations within the quadrants of an apparent homogenous atmosphere. The azimuth angles selected were 020, 110 and 180 degrees at elevations of 15, 30 and 45 degrees at each azimuth. A two-point calibration with reference temperatures of 0 °C and 30 °C were used to calibrate the data. The MCT detector was used at a 1 cm⁻¹ resolution. Radiance measurements were plotted and compared.

Environmental Monitoring

The environmental utility of the spectrometer was demonstrated 25 November 1998. A coal-burning smokestack located approximately 1 km away was situated in the telescope's field of view such that the top of the stack was barely visible at the bottom of the view, and the emissions filled the majority of the scope's field of view. The InSb detector was used at 1 cm⁻¹ resolution with a two-point calibration of 0 °C and 30 °C. Radiance measurements comprised of the average of 50 scans were collected. The azimuth angle of the spectrometer was then turned a few degrees away from the smokestack to collect a background radiance measurement. The calibrated radiance files were plotted and compared. Identification of constituent gases was done by comparing

observed peaks from the radiance measurement of the smokestack emission with the HITRAN 1996 database and other references.

IV. Results for Part 1

Determining the Kernel Functions

The attempt to find a physical retrieval method to determine atmospheric temperature and moisture information from observed radiance was not successful and further analysis is needed to completely understand why. The kernel functions were a maximum at the surface for each frequency from 2250 cm^{-1} to 2400 cm^{-1} , and the least-squares solution could not retrieve temperature information for any altitude. A more detailed discussion of the results on the physical retrieval method follows.

As stated in the previous section, the kernel functions were a maximum at the surface when calculated from the surface looking up. Plots of kernel functions calculated here did not look like the kernel functions reviewed in the reference material, so the method appeared suspect. Kernel functions shown in the reference material were calculated for satellite-borne sensors and all peaked at some unique altitude like those shown in Figure 1.6b previously. It was originally expected that kernel functions, calculated from the surface looking up, would be the same as that shown in reference material. That was not the case.

To validate the method, the kernel functions were calculated as if to be used by a sensor above the atmosphere looking down at the earth's surface. If the method was valid, these kernel functions would peak at heights near those shown in the reference material, and they did. Qualitative comparison of the kernel functions in Figure 1.6b and a reference (Goody and Yung, 1989: 264) indicated reasonable agreement for the five

frequencies selected to test the method. The method used here for calculating kernel functions was valid, so the next step was to determine why the retrieval method failed.

The Physical Retrieval

The reason for the failure is attributed to finding all kernel functions calculated over the spectral band 2250 cm^{-1} to 2400 cm^{-1} from the surface looking up were a maximum at the surface where the CO_2 concentration is greatest. This made it difficult for the matrix to determine specific information about a layer or height. In Figure 1.7 below, the matrix was created in Mathcad® using the ten frequencies and kernel functions (W) for the lowest ten path length intervals. The determinant of this matrix is zero indicating there was no unique solution. The term δz represents the change in path distance between the two intervals where the transmittance values were used to calculate the kernel function.

$$W := \begin{bmatrix} .0536 & .0228 & .0109 & .00565 & .00301 & .00168 & .00095 & .00056 & .00033 & .0002 \\ .0784 & .01219 & .00445 & .00208 & .0011 & .00064 & .00038 & .00025 & .00016 & .00010 \\ .0724 & .0145 & .00632 & .00311 & .00163 & .00088 & .00049 & .00028 & .00016 & .00009 \\ .0837 & .00996 & .00329 & .00142 & .0007 & .00038 & .00021 & .00013 & .00007 & .00005 \\ .0672 & .0203 & .00732 & .00294 & .00123 & .00055 & .00024 & .00012 & .00005 & .00003 \\ .073 & .01828 & .00565 & .00193 & .0007 & .00027 & .0001 & .00004 & .00002 & .00001 \\ .0796 & .01531 & .0037 & .00099 & .00028 & .00008 & .00003 & .00001 & 0 & 0 \\ .0873 & .01068 & .00167 & .00028 & .00006 & .00001 & 0 & 0 & 0 & 0 \\ .09423 & .00535 & .00039 & .00003 & 0 & 0 & 0 & 0 & 0 & 0 \\ .09958 & .00042 & 0 & 0 & 0 & 0 & 0 & 0 & 0 & 0 \end{bmatrix} \cdot \delta z$$

Figure 1.7. Example of 10 by 10 matrix created using frequencies and kernel functions such as those shown in Tables 2 and 3. The determinant of this matrix was zero indicating there was no unique solution to the physical retrieval.

Model Validation

Case I--5 October 1998

When data collection began, the sky was covered with stratus, the temperature was around 17° C, and the surface visibility was restricted to 3 miles due to fog and haze. Actual surface conditions observed at Wright-Patterson AFB and the Dayton International Airport are listed in Appendix 1.

The stratus began to dissipate approximately one hour after the initial radiance observation was collected as the temperature rose due to solar heating. This decreased the relative humidity and the clouds dissipated. It is not unusual for stratus to dissipate in this manner.

Figures 1.8a, 1.8b, and 1.8c compare how the radiance of the sky changed as the stratus dissipated. The radiance in Figure 1.8a was taken when the sky was overcast. Compared to the other two plots, this plot has less absorption from 800 cm^{-1} to 1200 cm^{-1} . The radiance is greater because it includes radiant energy from the stratus when the clouds covered the sky. In this case, there is little atmospheric absorption apparent, because the stratus was a significant radiance source. As the stratus layer thinned, the radiance over the spectral region from 800 cm^{-1} to 1200 cm^{-1} decreased, because there was less cloud cover to radiate, and now more atmospheric absorption due to water vapor from 800 cm^{-1} to 1200 cm^{-1} and ozone near 1040 cm^{-1} was observed. When the sky cleared, there was no radiant energy contributed by cloud cover, and there was even more absorption due to water vapor over the spectral region from 800 cm^{-1} to 1200 cm^{-1} and ozone near 1040 cm^{-1} as shown in Figure 1.8c.

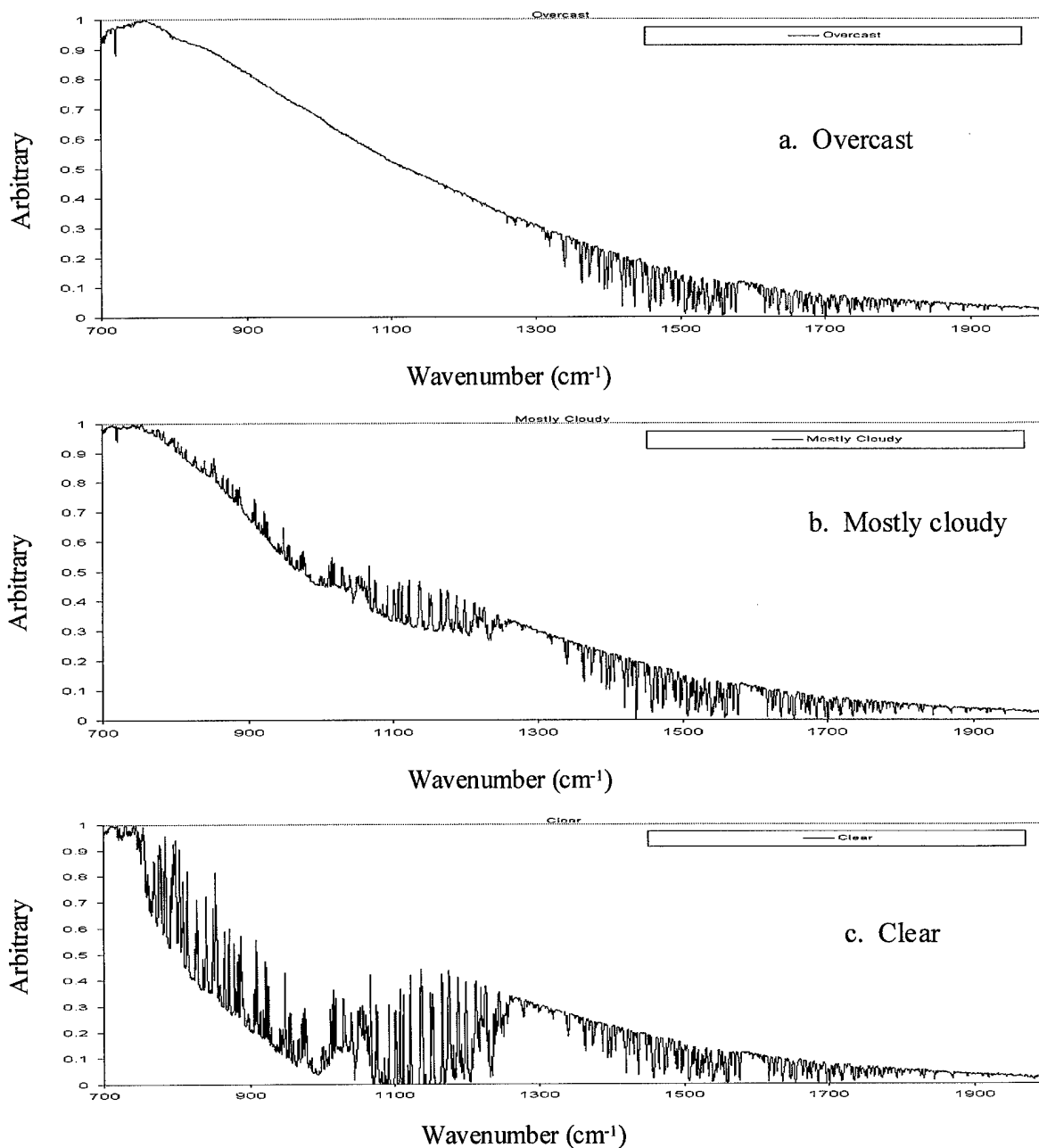


Figure 1.8a, 1.8b, and 1.8c. Comparison of observed spectral plots of cloudy, mostly cloudy, and clear sky on 5 October 1998. Plot a. was taken under overcast sky at 1218 LDT; plot b. was taken at 1233 LDT under a mostly cloudy sky; and, plot c. was taken at 1251 LDT under a clear sky.

Case II-20 October 1998

Data were collected from before sunrise to about one hour after sunrise. Differences between observed and calculated radiances are shown in Figures 1.9a through 1.9d.

Figure 1.9a compares the spectral features of the observed radiance from 500 cm^{-1} to 2000 cm^{-1} to radiance calculated by MODTRAN. The patterns are similar except for a noticeable difference over the 750 cm^{-1} to 1250 cm^{-1} spectral region where calculated radiance was much lower than observed radiance. This could have been caused by many reasons, and it was beyond the scope of this research to thoroughly examine the reason for the difference. The two likely causes could have been: 1) a difference between the actual atmospheric profiles over the spectrometer and that observed by the rawinsonde or 2) that the User-Defined Functionality did not accurately calculate atmospheric radiance using the observed rawinsonde profile.

The change in observed radiance plots from 0728 LDT to 0900 LDT is again compared to a MODTRAN calculated plot shown in Figure 1.9b only over a narrower band. There is a significant increase in observed radiance around 668 cm^{-1} over this period of time evident by an increase of radiance of about $.26\text{ W/cm}^2\text{ sr}^{-1}\text{ cm}^{-1}$ while surrounding regions did not vary by more than $.03\text{ W/cm}^2\text{ sr}^{-1}\text{ cm}^{-1}$. The MODTRAN calculated radiance did not change from 0728 LDT to 0900 LDT. The increase in observed radiance is attributed to increased molecular activity caused by collisions between the CO_2 molecules and solar radiation particles.

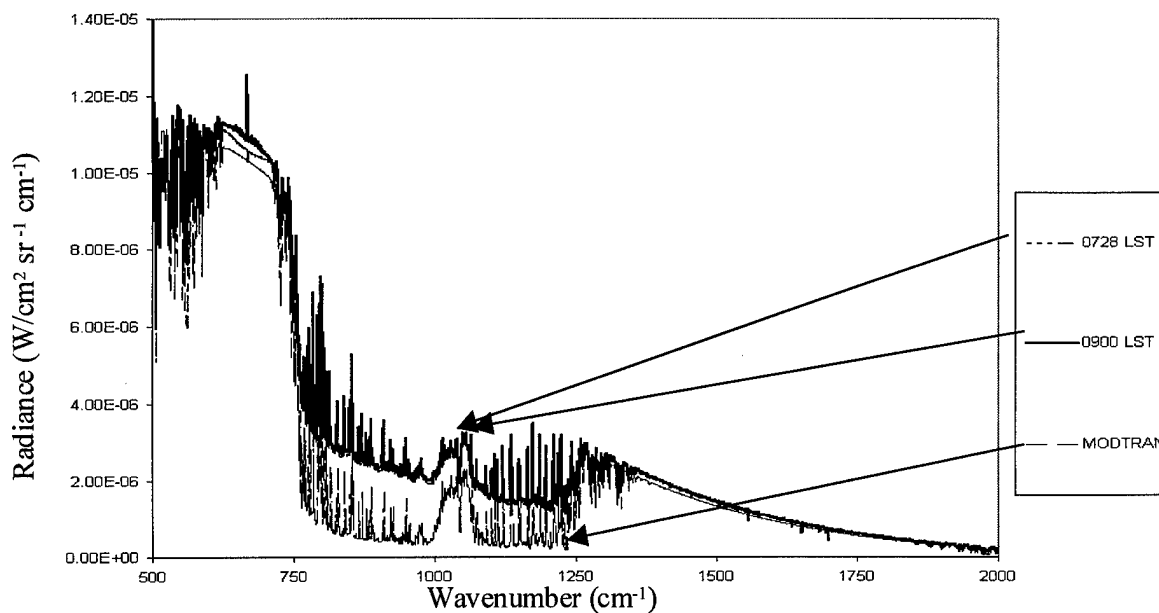


Figure 1.9a. Observed radiance from 0728 LST to 0900 LST compared to MODTRAN calculated radiance.

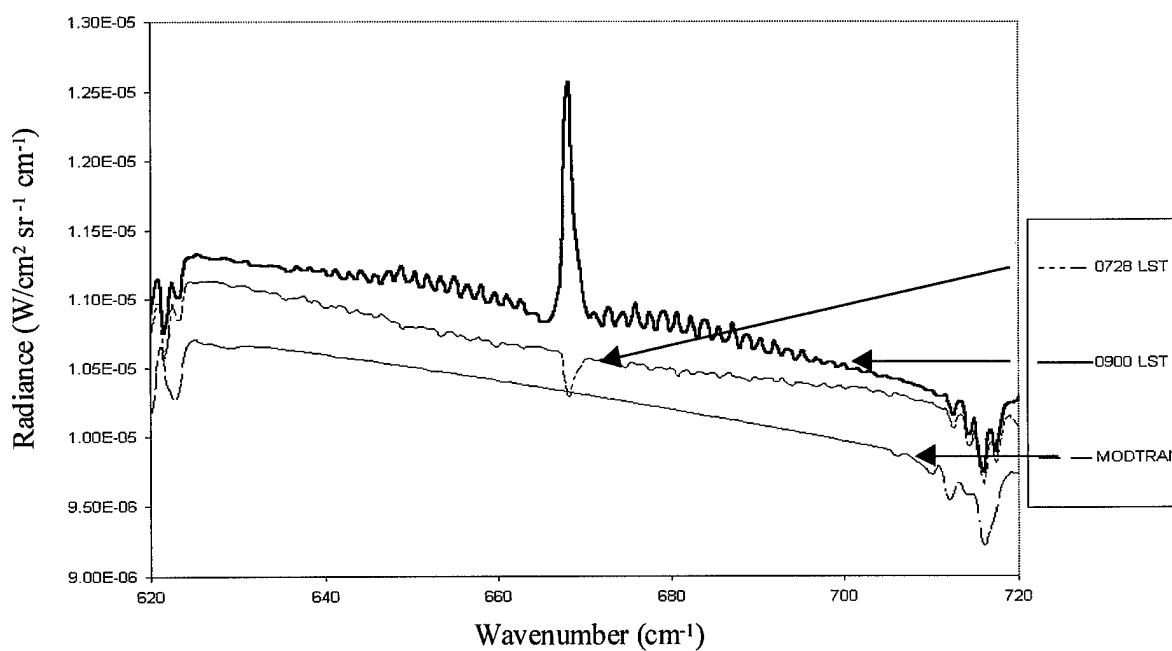


Figure 1.9b. Observed radiance from 0728 LST to 0900 LST compared to MODTRAN calculated radiance in spectral region 620 to 720 cm^{-1} .

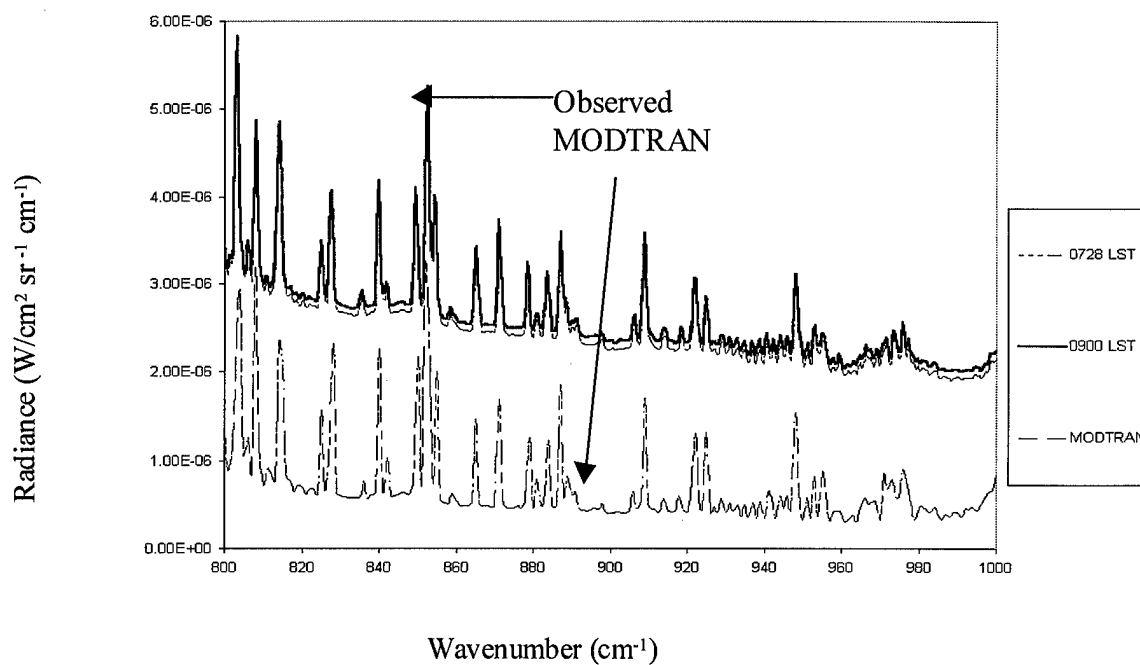


Figure 1.9c. Observed radiance from 0728 LST to 0900 LST compared to MODTRAN calculated radiance in spectral region 800 to 1000 cm^{-1} .

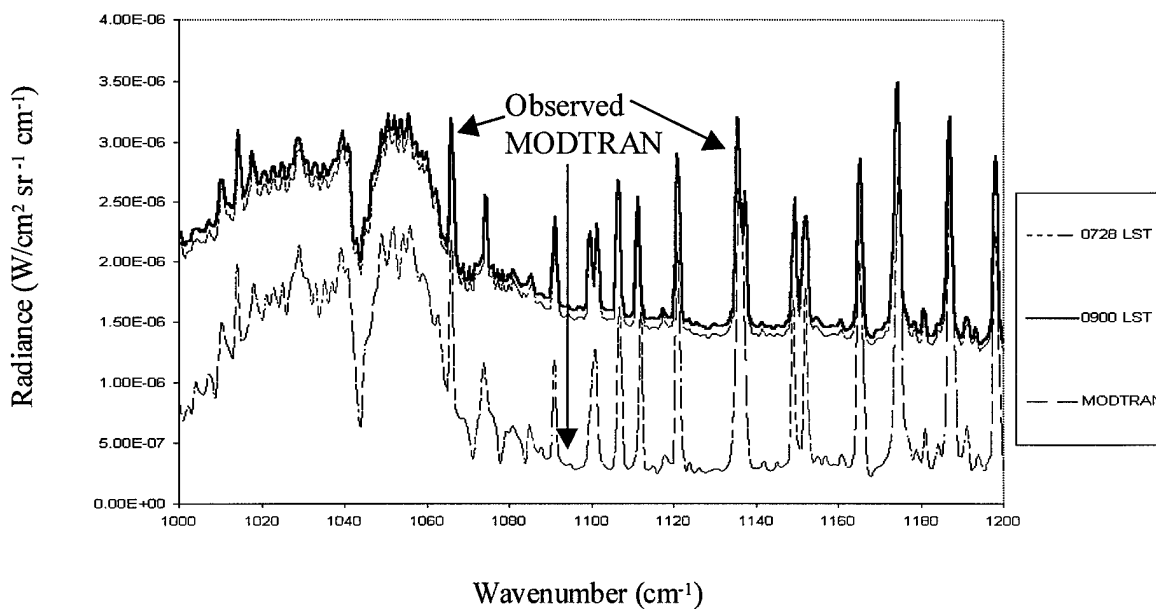


Figure 1.9d. Observed radiance from 0728 LST to 0900 LST compared to MODTRAN calculated radiance in spectral region 1000 to 1200 cm^{-1} .

In Figures 1.9c and 1.9d, of particular interest is how well the spectral features compare between the observed and calculated radiance. There is a line-for-line similarity between the observed and calculated spectral features. The main difference between the observed and calculated radiance plots is the magnitude of the radiance. Again, it was beyond the scope of this research to determine the cause for this difference. However, it is likely attributable to the differences in atmospheric profiles over the spectrometer at the observation time and that observed by the rawinsonde 30 miles away or due to the way the User-Defined Atmosphere functionality calculated radiance with rawinsonde data.

Case III-11 November 1998

Radiance observations were again compared to calculated atmospheric radiances. Figure 1.10a compares the observed radiance using the MCT detector with calculated atmospheric radiance from MODTRAN. Results similar to Case II are noted here. The observed radiance in Figure 1.10a differs from MODTRAN calculated radiance over the 750 cm^{-1} to 1250 cm^{-1} region. In Figure 1.10b, the observed spectral feature in the center of the $15\text{ }\mu\text{m}$ CO_2 absorption band at 668 cm^{-1} differs from that calculated by MODTRAN.

In Figures 1.10c and 1.10d, another very good match between the observed spectral features and those calculated using MODTRAN was found with differences noted in the overall radiance values similar to that found in Case II.

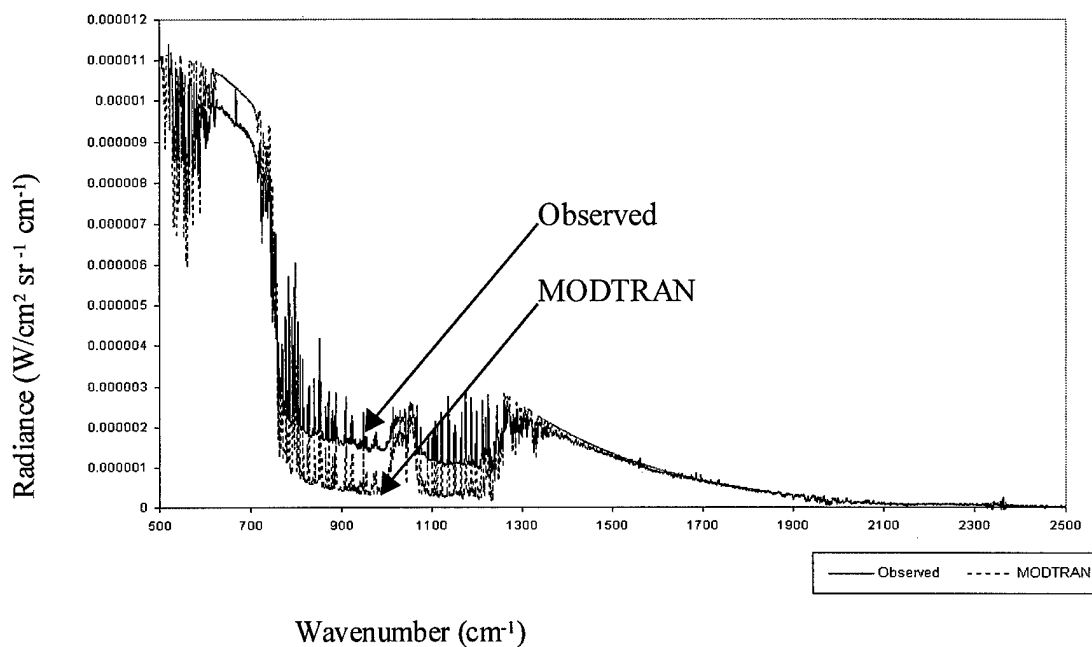


Figure 1.10a. Radiance observed at 0900 LST 11 November 1998 compared to MODTRAN calculated radiance using 1200 UTC rawinsonde from Wilmington OH.

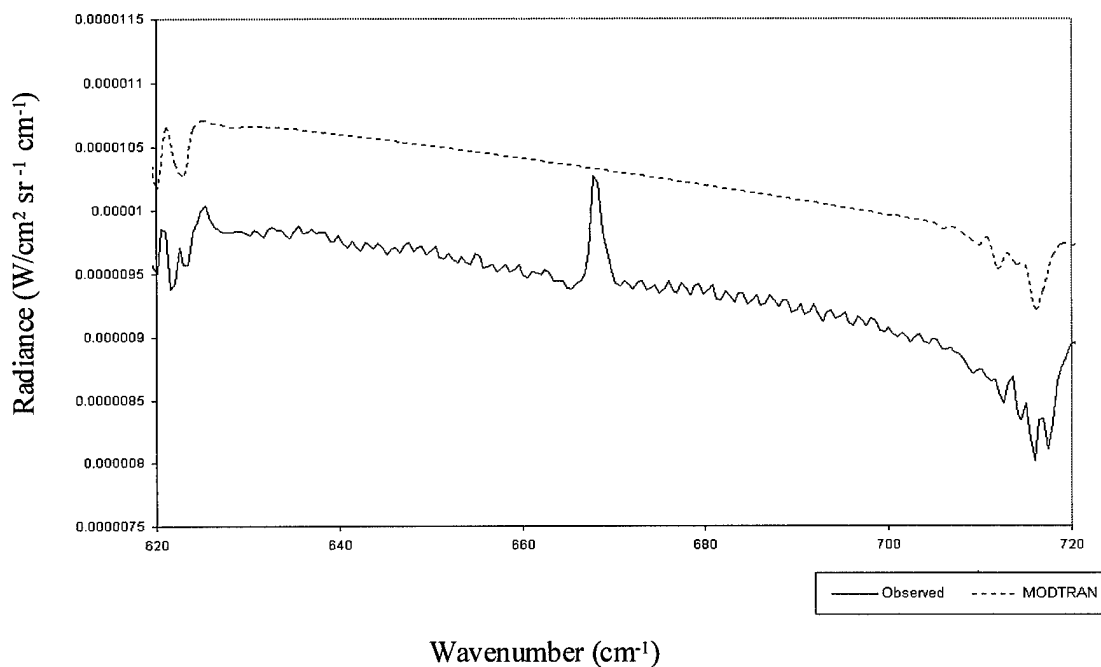


Figure 1.10b. Radiance observed at 0900 LST 11 November 1998 compared to MODTRAN calculated radiance using 1200 UTC rawinsonde from Wilmington OH.

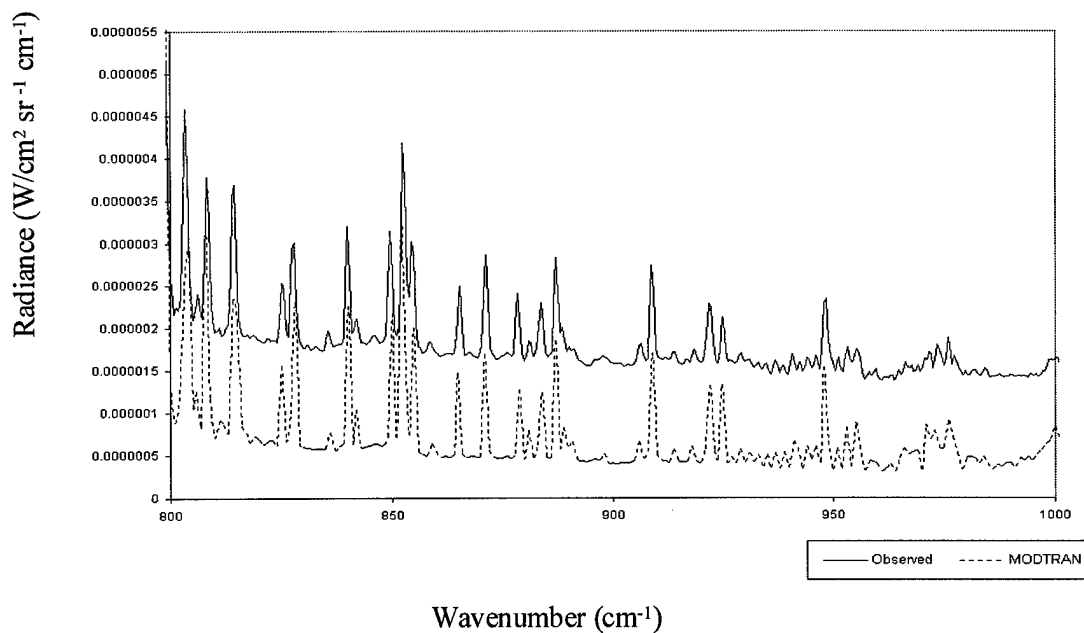


Figure 1.10c. Radiance observed at 0900 LST 11 November 1998 compared to MODTRAN calculated radiance using 1200 UTC rawinsonde from Wilmington OH.

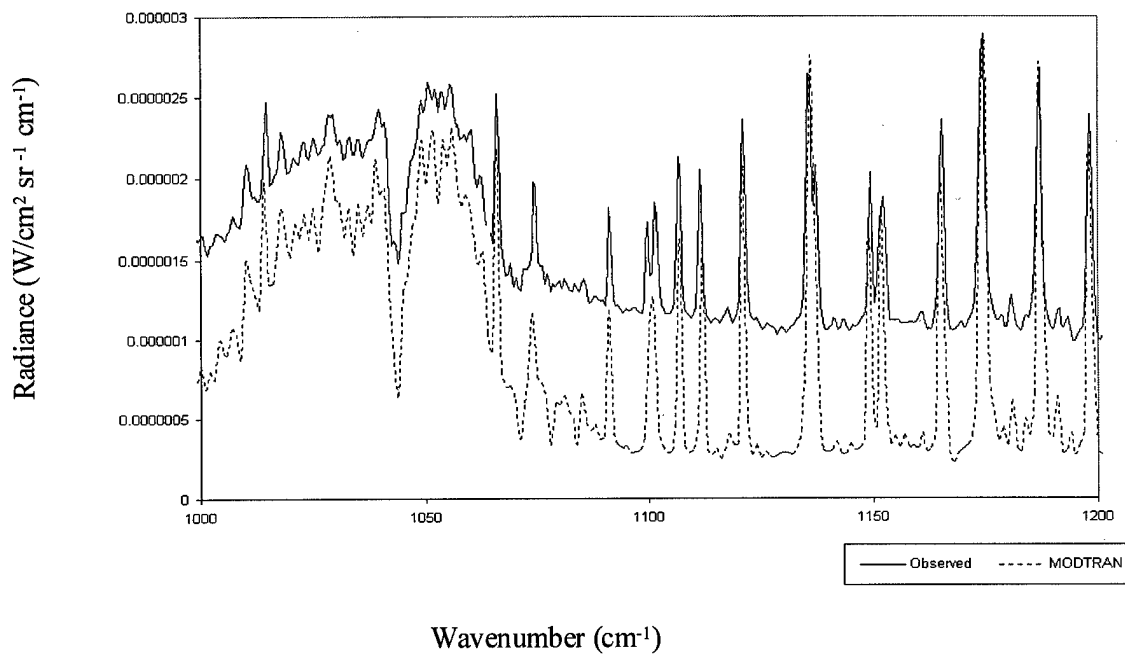


Figure 1.10d. Radiance observed at 0900 LST 11 November 1998 compared to MODTRAN calculated radiance using 1200 UTC rawinsonde from Wilmington OH.

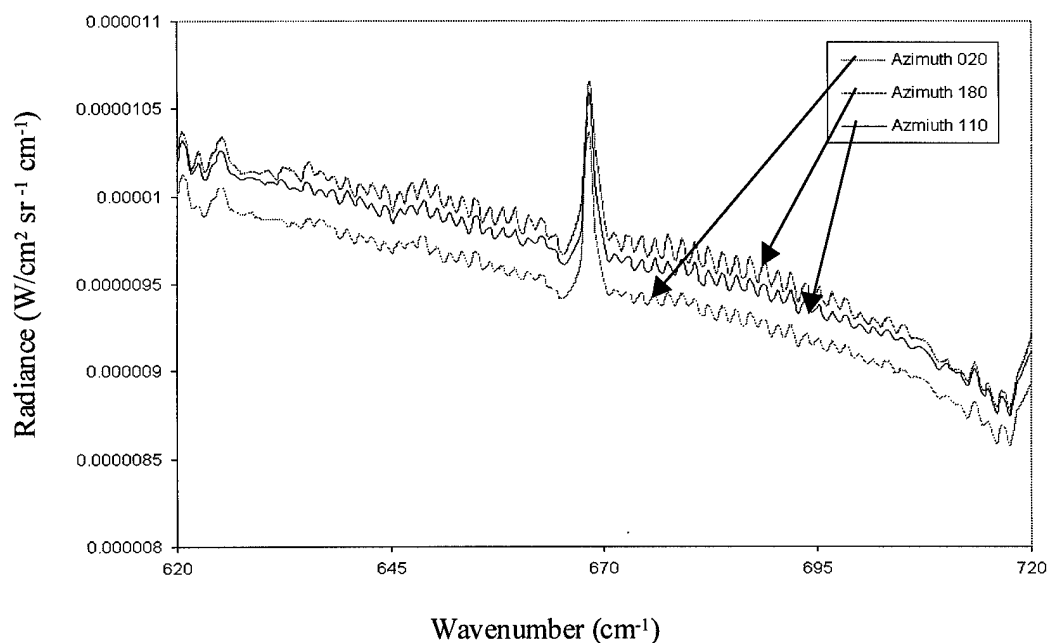


Figure 1.10e. Radiance observed 11 November 1998 at the same elevation angle along three different azimuth angles.

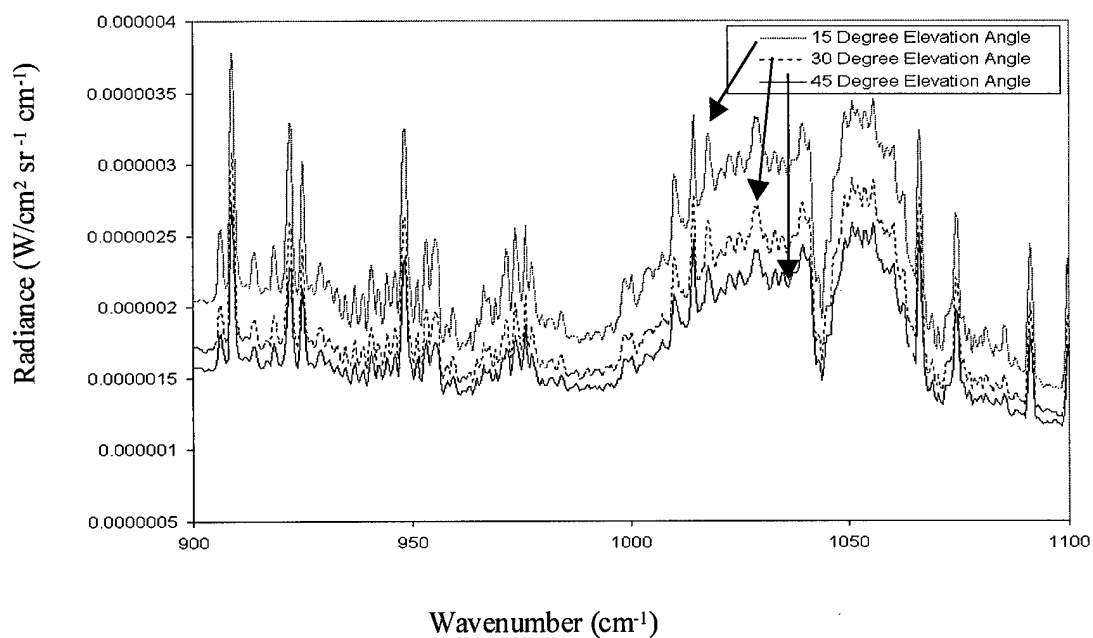


Figure 1.10f. Radiance observed 11 November 1998 at the same azimuth at different elevations.

In Figure 1.10e, plots of radiance measured along three different azimuth angles at a constant elevation angle are shown. In Figure 1.10f, the azimuth angle remained constant and the radiance was measured along three different elevation angles.

In Figure 1.10e, radiance was collected at azimuth angles of 020 (northerly), 110 (easterly), and 180 (southerly) degrees. The radiance measured along the northerly azimuth was the lowest observed between the three directions. The next lowest radiance was of that measured towards the east. The radiance of the southerly view was the greatest of the three. These results should be interpreted to mean that the actual temperature profile to the north was colder than the profiles to the east and south, and that the profile to the south was the warmest. This is consistent with general observations that the colder air is usually to the north. There was no attempt to calculate the magnitude of the temperature different between the northerly and southerly radiance measurements or verify these observations.

In Figure 1.10f, radiance measurements from three different elevation angles above the horizon, 015, 030, and 045 degrees, along the same azimuth of 110 degrees are compared. In this case, the measured radiance was greatest at the lowest elevation, second coldest at 030 degrees, and coldest at 045 degrees. Intuitively, it should be this way. The warmest temperatures in atmospheric profiles are generally observed in the lowest levels of the atmosphere, so a radiance measurement that samples this region should return the greatest radiance. As the elevation angle increased, the radiance decreased, meaning the colder air at higher altitudes was sampled.

Environmental Monitoring

Case IV--25 November 1998

The environmental utility of the FTIR spectrometer for environmental monitoring was successfully demonstrated. Figure 1.11 compares the difference between the radiance of the background and the radiance of emissions from the Wright-Patterson AFB Area B coal-burning plant smokestack. Prominent peaks in the smokestack radiance plot were compared with the HITRAN 1996 database and other references. The wavenumbers and constituent gases most likely attributable to the identified features are: 2224 cm^{-1} (N_2O); 2348 cm^{-1} (CO_2); and three peaks near 2078 cm^{-1} , 2094 cm^{-1} , and 2125 cm^{-1} (O_3). A weak band of HCl is centered near 2886 cm^{-1} and another weak feature at 2504 cm^{-1} may be due to SO_2 . Although expected, spectral features associated with NO_2 were not noted but may have overlapped with other observed signatures.

It was beyond the scope of this research to identify the temperature of the emissions or the concentration of each constituent gas, although this could be done and compared with measurements taken from within the facility.

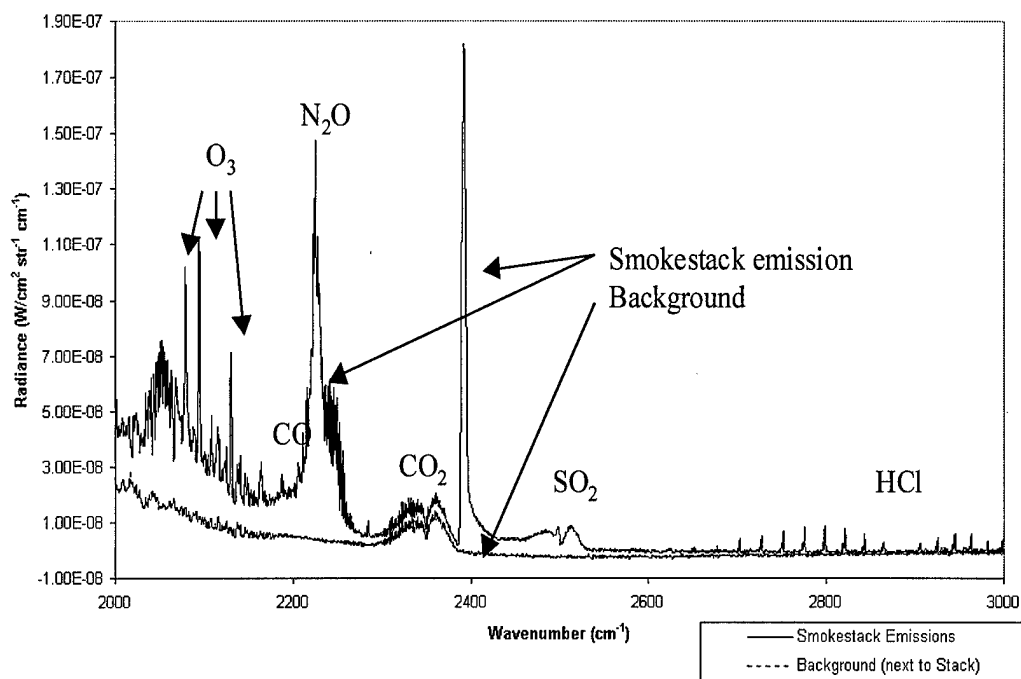


Figure 1.11. Spectral plot of emissions from a coal-burning plant smokestack located near Area B Wright-Patterson AFB compared to background radiance. Data was observed 25 November 1998.

V. Conclusions for Part 1

The physical method analyzed to retrieve atmospheric temperature and moisture information from ground-based radiance observations was not successful. Atmospheric absorption due to carbon dioxide is greatest at the surface where the concentration of carbon dioxide is the greatest. As a result, the kernel functions calculated for a ground-based sensor maximized at the surface and decreased with height, so a least-squares solution could not determine a unique retrieval. Although this physical method was unsuccessful here, it may still be possible to find a physical retrieval method to invert radiance observed at the surface into temperature profiles. The solution will likely be very complex and may not work for all radiance observations such as those with temperature inversions. Still, additional research on the physical method is recommended. Temperature retrieval using a statistical method similar to that used by the University of Wisconsin-Madison on radiance observations AERI should be considered, if all efforts to find a physical method fail.

In the model validation cases considered, the atmospheric model MODTRAN represented spectral features of the atmosphere extremely well. A minor exception was observed in the 15 μm CO_2 absorption band when during a sunrise event, the observed radiance at 668 cm^{-1} increased by $0.26\text{ W/cm}^2\text{ sr}^{-1}\text{ cm}^{-1}$. Other frequencies within the spectral region from $600\text{--}700\text{ cm}^{-1}$ did not vary more than $.03\text{ W/cm}^2\text{ sr}^{-1}\text{ cm}^{-1}$. The modeled output showed no variation of the 668 cm^{-1} radiance over the same time period. The increased observed radiance was attributed to increased molecular activity due to increased collisions between CO_2 molecules and solar radiation particles. Spectral features calculated from $800\text{--}1200\text{ cm}^{-1}$ lined up exceptionally well with the observed

features. The difference in radiance was not fully examined but was attributed to either the difference between the atmospheric profile used to calculate the atmospheric radiance in MODTRAN and the actual profile above the spectrometer during data collection or due to the UDA itself. Its functionality was useful, but its validity is questionable. Differences, between observed radiance compared to radiance calculated by MODTRAN using the UDA functionality and a representative atmospheric profile, were noted. Validation of the UDA is suggested.

The FTIR spectrometer demonstrated its capability for environmental monitoring. The plot of a calibrated radiance measurement of the Wright-Patterson AFB Area B coal-burning smoke stack showed numerous spectral features. Comparing these features to reference information led to the identification of CO_2 , CO , N_2O , O_3 , HCl , and SO_2 , all common byproducts from coal combustion. This would be an interesting follow-on research project for an environmental student to quantify the concentration of the constituents of the emission and track the concentration over time for comparison with measurements taken within the power facility.

Part 2-Spectral Features of Conventional Warhead Explosions

I. Introduction

Summary

A BOMEM MR-154 spectrometer was used to collect spectral data of controlled detonations of statically displayed Mk 82, Mk 83, and Mk 84 bombs; High-speed Anti-Radiant Missiles (HARM); Tomahawk Land-Attack Missiles (TLAM); and C-4 plastic explosives. The warheads were detonated on Bravo 20 Bomb Range, Fallon Naval Air Station NV from 7 December 1998 to 11 December 1998. Data were collected over the 1800 cm^{-1} to 6000 cm^{-1} spectral region at a resolution of 16 cm^{-1} . Spectral plots of the explosions were compared. Unique spectral features associated with explosions of the individual types of warheads were revealed. The preliminary results suggest it may be possible to identify the type of warhead detonated by examining its spectral signature.

Background

Engineers from Wyle Laboratories working for the Infrared Sensors Laboratory within Air Force Research Lab Sensors Branch (AFRL/SN), Wright-Patterson AFB, Ohio, collected radiometric data of controlled detonations of conventional warheads. The test was part of ongoing research conducted to assess the capability of remote sensors to determine information about the battlespace. For this phase of testing, the primary task was to use a radiometer to measure the radiant intensity of each detonation to serve as ground truth for comparison with other remote sensors. Spectrometric data was desired, but the AFRL/SN spectrometer was inoperative.

The Air Force Institute of Technology School of Engineering (AFIT/EN) had just acquired a BOMEM MR-154 spectrometer and was asked to collect spectrometric data for the test. Initially, it was planned to compare radiant intensity measured by the spectrometer to that measured with the AFRL radiometer.

The spectrometer data collection rate varied with resolution. For instance, at a resolution of 2 cm^{-1} , the data collection rate was $0.9\text{ scans sec}^{-1}$, and the data collection rate was only $5.4\text{ scans sec}^{-1}$ at 128 cm^{-1} resolution. The 16 cm^{-1} resolution and $3.6\text{ scans sec}^{-1}$ scan rate was selected based on a trade off between resolution and scanning speed. In comparison, the radiometer retrieved 2000 scans sec^{-1} over four, smaller spectral bands.

It was believed the explosion events would not exceed two seconds in duration and the peak intensity would be very short lived. Considering the low spectrometer scan rate and short duration of the event, it was unlikely the spectrometer would collect a scan at the moment of peak radiant intensity. Comparison of peak radiant intensity observed by the spectrometer and radiometer was probably not worthwhile, but the spectrometer offered the advantage of temporal and spectral resolution not provided by the radiometer or considered previously. The spectrometer's temporal resolution allowed each event to be examined for changes in emissions at intervals of approximately 0.27 seconds. If the spectrometric data revealed unique spectral signatures of each type of warhead detonated, this could prove useful to the intelligence community. Potentially, the type of warhead detonated could be identified remotely by examining the spectral plot of the explosion.

Assumptions and Limitations

The first assumption was that the detonation of a warhead would generate a spectral signature unique to the explosive or warhead and that the signature would be observable at a resolution of 16 cm^{-1} within the sensitivity of the InSb detector.

It was not known what the temperature of and near the explosion would be. It was assumed a calibration file using cold and hot radiometric reference temperatures of 0°C and 700°C included the temperature of the explosion. Further, it was assumed one calibration file was sufficient to calibrate all events for the day regardless of the change in ambient conditions. Additional radiometric reference points could not have been collected due to the time required for the black body to stabilize and constraints of the event schedule.

It was assumed the background radiance did not need to be subtracted from the radiance observations of the explosions. The peak radiance of the explosion observed by the spectrometer was three orders of magnitude greater than the background radiance.

The spectrometer was not equipped with a video capability to record each event. So, there was no objective record to show how much of each event filled the field of view (FOV). Further, there was no exact method to determine how much of the event filled the FOV compared to any background radiance. This made it difficult to accurately calculate temperature of the events. The impact of this limitation may have been minimal to this research effort, since the spectral signatures themselves were to be examined and not necessarily radiant intensity.

II. Methodology

Data were collected from 7 December 1998 to 11 December 1998 at Range Bravo 20 located at Fallon Naval Air Station, Nevada. Geographically, the range is located approximately 75 miles east-northeast of Reno, Nevada or 30 miles north-northeast of Fallon, Nevada. The range is on a dry lakebed between two mountain ranges. The lakebed is 4000 feet above sea level, and the highest mountain peak is 7000 feet above sea level. Since the lakebed is very flat, there was an unobstructed view of the entire bomb range. In Figure 2.1, the spectrometer is in the left center and is partially hidden by a black body set on a tripod. The snow-covered bomb range is in the background. A second black body is seen in the lower left. The objects to the lower right are empty bomb cases stored near the west tower. Figure 2.2. shows the computer used to operate the spectrometer. The makeshift desk is the spectrometer's transit case.

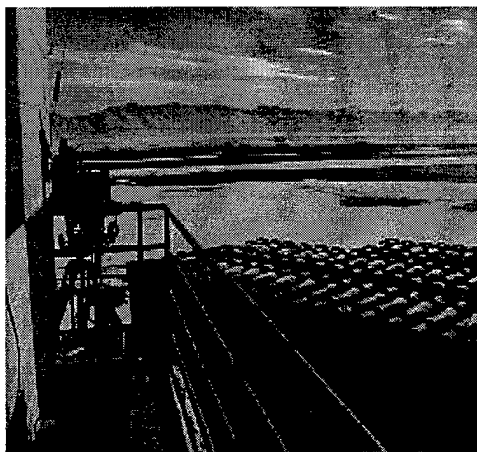


Figure 2.1. Spectrometer's view of the bomb range.

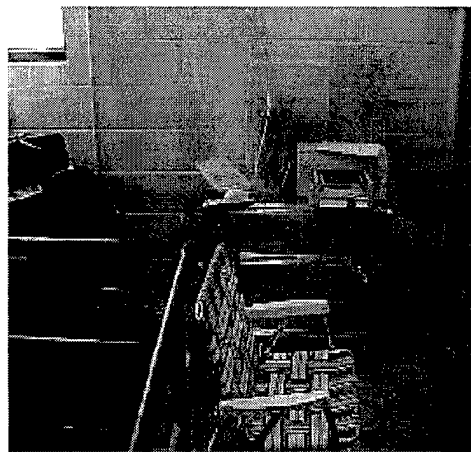


Figure 2.2. Computer used to operate the spectrometer.

Explosive Ordnance (EOD) personnel arranged the ordnance the week prior to data collection. All of the explosives were oriented in predetermined configurations and on

various surfaces. Some bombs were placed on the ground while others were partially buried. The instruments collected data from the West Tower shown in Figure 2.3.

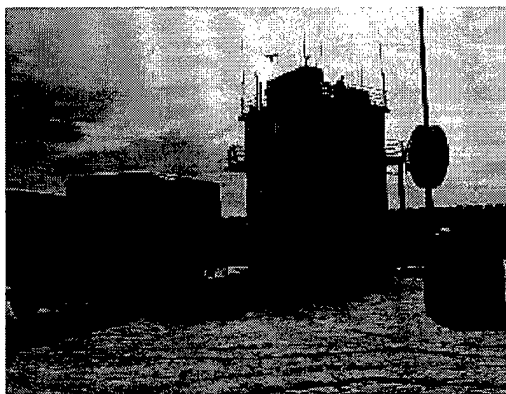


Figure 2.3. West Tower located on Bravo 20 bomb range.

The explosives were detonated at distances ranging from approximately 300 meters to 5000 meters away from the West Tower depending on the quantity of explosive. The larger quantities were detonated further away. The detonations, or events, were numbered from 1 to 64, and the four detonations of plastic explosives were labeled from A to D. The test was planned such that two consecutive events had similar configurations. For example, event 1 and 2 involved the same warhead oriented in the same manner in similar soil. This provided the opportunity to collect the first of the two events at 16 cm^{-1} and the second at 2 cm^{-1} resolution for comparison. Only the data at the resolution of 16 cm^{-1} were analyzed here. Configurations and distances of each test event are listed in Appendix 2. The data collection was divided into four days of testing. The first 16 events began in the afternoon of day 1 of testing and continued until after sunset.

The remaining events began after sunset and were completed before sunrise of day 2, day 3, and day 4.

Typical sequence of events for a day of testing was as follows. Before testing, the spectrometer was set on its tripod up to one hour prior to start time and allowed to stabilize to the ambient temperature. The InSb detector and cold subtraction source were attached, filled with liquid nitrogen, and allowed to stabilize. The black body was set at the cold reference temperature and allowed to stabilize. Without the telescope attached, the black body was aligned with the spectrometer such that the black body filled the spectrometer's entire FOV. Alignment involved positioning the black body on the tripod so the black body's cavity lined up with the collimator on the spectrometer as shown in Figure 2.4.

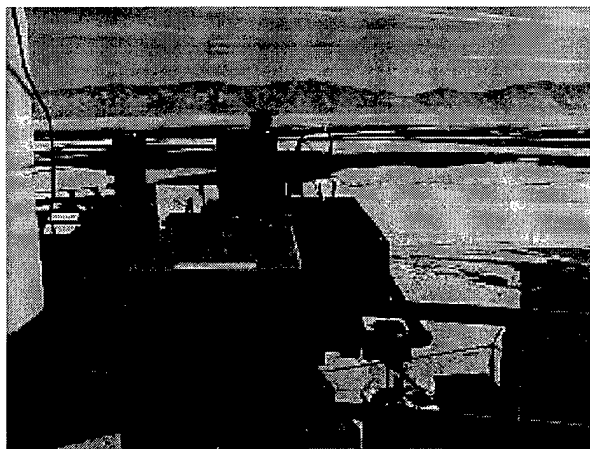


Figure 2.4. Aligning the black body with the spectrometer.

Prior to the first detonation, the cold radiometric reference was collected. The telescope was installed on the collimator. The black body temperature was then

increased to the hot reference temperature. At this point, the spectrometer was prepared for data collection. Before each detonation, EOD personnel drove four-wheel drive, all-terrain vehicles to the site of the next planned event. From this site, EOD personnel directed their headlights toward the West Tower. Each team sighted their instrument on these headlights and waited for detonation. The EOD personnel cleared the range and detonated the ordnance using remote transmitters. Each team ensured data for the event was captured then prepared for the next event. After the final event, the hot reference was collected. A calibration file was created using the reference temperatures recorded and applied to each raw data file and saved for post analysis.

III. Results for Part 2

The spectral plots of selected events are provided in this section. Spectral and temporal features distinguishable on signatures of each type of ordnance were noted and examples are shown in this section. Visual comparison of the plots reveals differences between the different explosives detonated. It is important to note that the radiance plots are not scaled the same for all events.

Information about each event, *e.g.*, type of explosive, quantity, range, and resolution of data collected, are listed in Appendix 2. Plots of additional events are provided in Appendix 3.

In Figures 2.5 through 2.8, the spectral plots of selected events are shown. The peaks in these plots are labeled by the BOMEM Grams/32® software package. These peaks were compared with the HITRAN 1996 database and other references for identification of the gas constituents most likely to be responsible for the emission at that frequency. The similarities and differences between the plots are discussed next.

The CO₂ absorption band from approximately 2250 to 2400 cm⁻¹ is distinguishable on every plot. This feature is marked by the observed radiance of zero over this spectral region. This CO₂ absorption feature is a well-known atmospheric absorption band and is not unique to any explosion events. Other similarities between the plots are intensity peaks at approximately the same frequencies. For example, peaks are observed at or near 2006, 2032, 2051, and 3043 cm⁻¹ for all four plots. These are not the only peaks that are observed in each event, but they are listed here to demonstrate a point. These peaks are

associated with O_3 , H_2O , and CH_4 , and it should not seem unusual that explosive events would excite or generate some of the same gas constituents.

There were occasions when peaks or spectral features were unique to a particular type of explosive. For example, a peak is observed at 2154 cm^{-1} for a Mk 82 and 2172 cm^{-1} for a HARM missile. Identification of bomb type was simplified when peaks occurred at different frequencies, however when the same peaks were observed on plots of two or more different types of explosives, it was necessary to compare observed radiances quantitatively at these peaks and qualitatively over the entire spectral plots. Shown in Figure 2-5 is a plot of a Mk 82 event. Emissions from gases, inferred by the observed peaks, included O_3 , N_2O , CH_4 , NO_2 , and CH_3Cl . And as stated previously, these gases were not necessarily unique to the Mk 82 bomb. However, qualitative comparison of the spectral feature of the Mk 82 to either of the other explosive types in Figures 2.6 or 2.8 shows the signature and radiance of the Mk 82 was rather unique. The maximum observed intensity was approximately $65 \times 10^{-6}\text{ W/cm}^2\text{ sr}^{-1}\text{ cm}^{-1}$ or at least 20 to 30% more than the observed radiance in the other three plots.

Figure 2-6 shows an example of the spectral plot of a HARM missile explosion. The peak radiance at 2172 cm^{-1} was unique to the HARM missile. The CO_2 absorption band is again observed, as are the peaks at or near 2006, 2032, 2051, and 3043 cm^{-1} as seen on the Mk 82 plot. Qualitatively, the signature does not look like the Mk 82. The peak intensity at 2172 cm^{-1} is approximately twice that as the intensity over the 2500 cm^{-1} to 3000 cm^{-1} spectral band. In the Mk 82, the radiance at 2154 cm^{-1} was approximately the same as the radiance observed over 2500 cm^{-1} to 3000 cm^{-1} . For the HARM missile, this

difference in radiance was likely due to the smaller quantity of explosive in the warhead compared to the Mk 82.

A spectral plot of a TLAM missile (WDU-25) is shown in Figure 2.7. At first glance, it is difficult to tell the difference between the plot of a TLAM missile explosion and the Mk 82 event in Figure 2.5. It is important to note that the Mk 82 and TLAM are plotted against different radiance scales. If the two charts were overlaid, it would be observed that the spectral features match. The only obvious, distinguishable difference between the TLAM and the Mk 82 is the radiance itself where the radiance of the TLAM is approximately half that of the Mk 82.

In Figure 2-8, the C-4 plastic explosive event displays less defined peaks and lower radiance most likely due to the considerably smaller quantity of explosive when compared to the other events. The CO₂ absorption band exists but is not as strong as shown in the other plots. One may observe that the CO₂ absorption feature appears weaker and less broad for the C-4 plastic explosive event shown in Figure 2.9 than it does for the Mk 82 in Figure 2.5. The difference in absorption is due more to the fact that the C-4 event occurred only 304 meters away from the spectrometer while the Mk 82 event occurred 4312 meters away. Simply put, there was more atmospheric absorption due to CO₂ over the greater distance for the Mk 82 event than there was for the C-4 event. Peaks observed in the three previous plots exist but are not as prominent with the C-4. The radiance is about 15 % of the Mk 82 event.

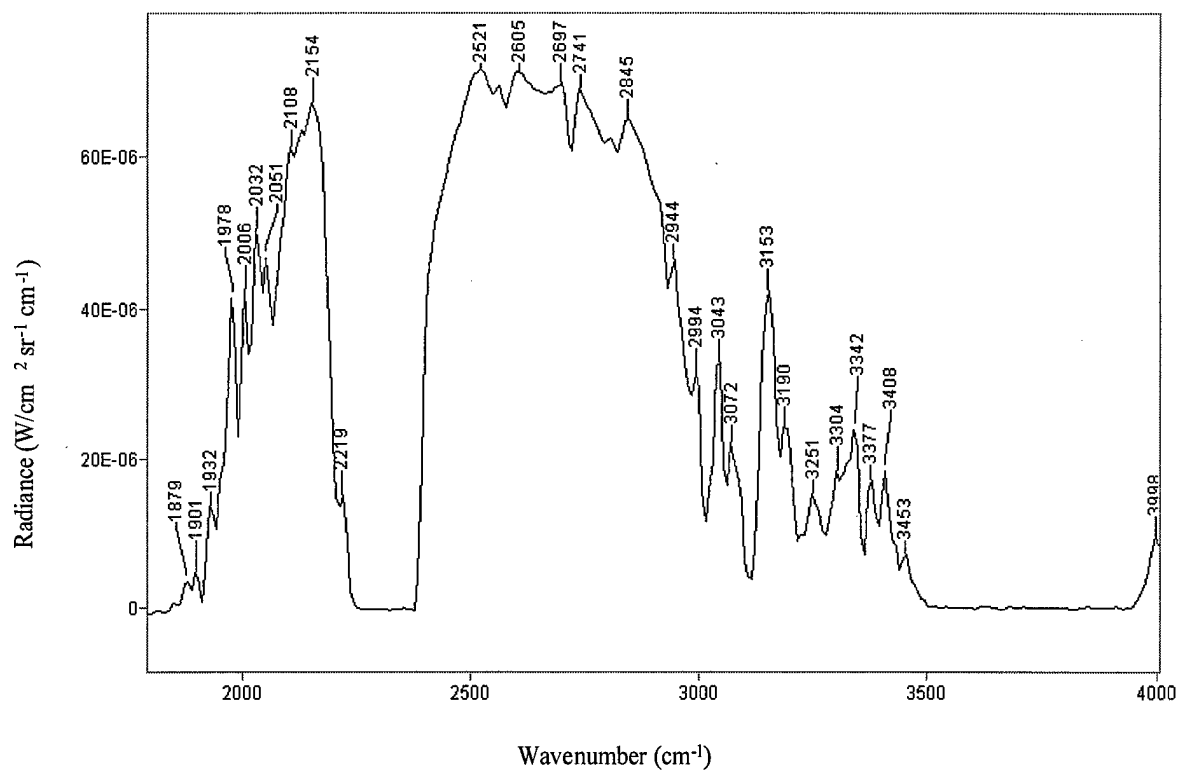


Figure 2.5. Initial spectral signature of event 1, Mk 82 bomb explosion.

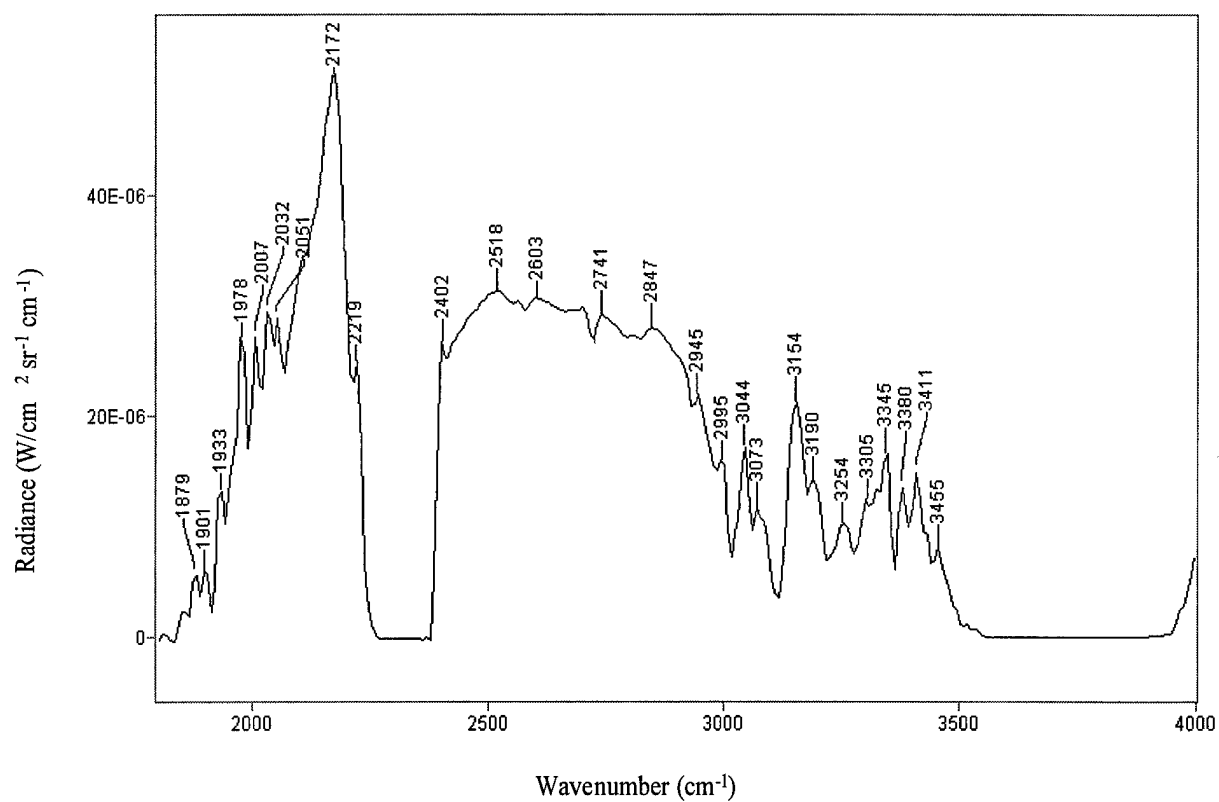


Figure 2.6. Initial spectral signature retrieved of event 34, HARM missile explosion

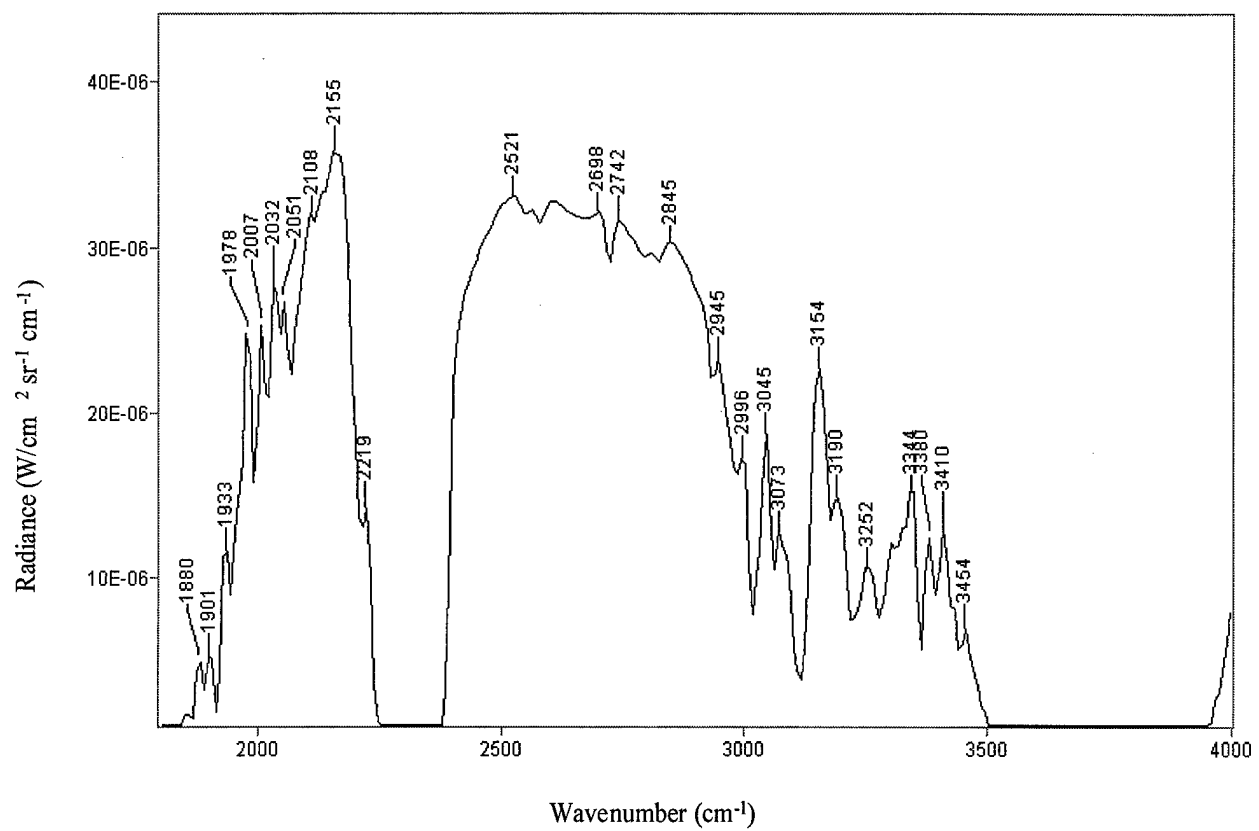


Figure 2.7. Initial spectral signature retrieved of event 43, TLAM (WDU-25) missile explosion.

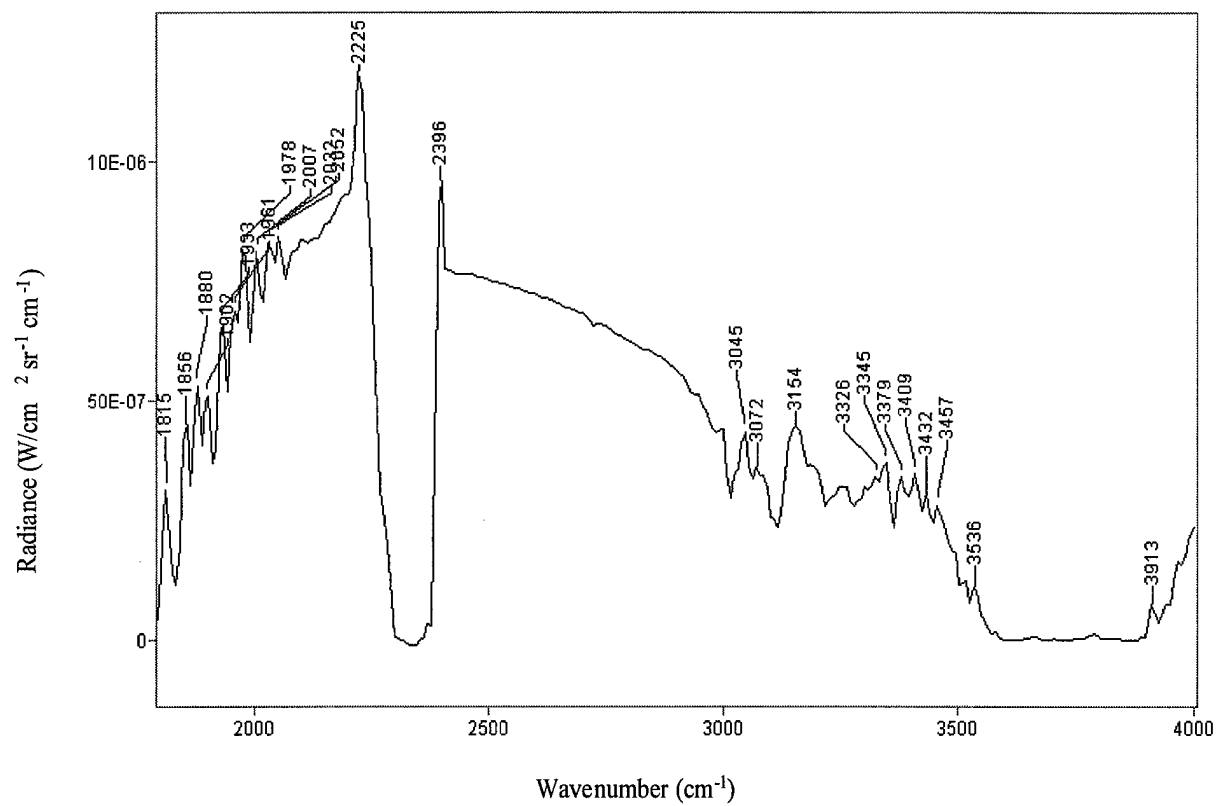


Figure 2.8. Initial spectral signature retrieved of event A, C-4 plastic explosive detonation.

V. Conclusions for Part 2

Spectral signatures of detonations of a Mk 82 bomb, a HARM missile, a TLAM missile, and C-4 plastic explosives were examined and compared. Spectral plots of these detonations displayed peaks at different frequencies that were sometimes unique to the explosive and sometimes common to other explosives. When spectral peaks were different, it was possible to identify an explosive event by its observed peaks. For example, the observed peaks near 2154 cm^{-1} for the Mk 82 and 2172 cm^{-1} for the HARM missile seem to be characteristic of the respective ordnance. When the observed peaks were the same or within one wavenumber, explosive types could be distinguished by comparing the value of the measured radiance at that frequency. For example, by comparing the observed radiance of $65 \times 10^{-6}\text{ W/cm}^2\text{ sr}^{-1}\text{ cm}^{-1}$ for the Mk 82 at 2154 cm^{-1} to that of the TLAM radiance of approximately $35 \times 10^{-6}\text{ W/cm}^2\text{ sr}^{-1}\text{ cm}^{-1}$ at 2155 cm^{-1} .

Some of these peaks common to all events were observed at 2006, 2032, 2051, and 3043 cm^{-1} and were attributed to O_3 , H_2O , and CH_4 when the peaks were compared to the HITRAN 1996 database. It did not seem unusual that these peaks and gas constituents were common to all events.

Results here show promise but are not conclusive after one test. Further research should be considered and should include detailed analysis of the finer resolution data (*i.e.*, 2 cm^{-1}). The lists in Appendix 2 shows data were collected at 2 cm^{-1} , but this data was not analyzed here and needs to be reviewed. Additional information is available from the radiometric data collected by the Wyle Laboratory engineers. For instance, for a Mk 84 event, the spectral data revealed a slow increase then decrease in observed radiance that lasted for about 3 seconds. After reviewing only the spectrometric data, it

was believed this was characteristic of that explosive, however the radiometric data revealed the true story. The slow increase and decrease over several seconds was actually the fireball that occurred after the peak radiance of the explosion that lasted only 0.10 seconds. The peak of this event happened so quickly, the spectrometer did not see the peak but could see the fireball that lasted several seconds afterwards. Analysis of the spectrometric and radiometric data should be completed simultaneously.

For future research, it may be useful to determine chemically what gases would be emitted or excited during an explosion, determine what spectral region these emissions could be observed over, and use a detector designed to observe that region. It is also recommended a spectrometer with a scan rate faster than 3.6 scans per second be used to collect data. This will insure data with greater temporal resolution is collected.

It also may be helpful for experts in the field of chemistry and spectroscopy to review the data and offer suggestions on how to fully exploit the capability of FTIR spectroscopy for battlespace assessment. Specifically, it seems reasonable to assume that the spectral signature of an explosion can be used to determine the type and quantity of explosive detonated and characterization of secondary fires. Once a reliable spectroscopic database of explosions is created either by field collection, laboratory analysis, or simulation, this could be useful to field commanders requiring detailed information of the battlespace. A spectrometer could collect data from the battlespace and characterize explosions and secondary fires. Also consider the potential involved in identification of the detonation of an enemy's bomb or missile used to inject chemical or biological material. A field commander could respond even before the chemical or biological material was detected using current detection methods.

Appendix 1: Weather Data

Surface weather observations and rawinsonde data are provided for Part 1. The identifier KFFO identifies the observations for the airfield at Wright-Patterson AFB. The identifier KDAY is the Dayton International Airport. Rawinsonde data is from Wilmington OH which is located approximately 30 miles south-southeast from the site where radiance data was collected.

Weather Data for 5 October 1998

```
KFFO 051255Z 09008KT 1SM R05/4000FT BR OVC004 11/11 A3019 RMK SLP229 8/6// 9/8//
KFFO 051655Z 11007KT 3SM BR BKN010 BKN250 17/12 A3018 RMK SLP223 BKN010 V SCT 8/501 9/501
KFFO 051718Z 12008KT 4SM HZ FEW010 SCT250 18/12 A3017
KFFO 051755Z 13006KT 4SM HZ FEW010 OVC030 19/13 A3018 RMK SLP223 8/500 9/800 56012

KDAY 051351Z 13010KT 1/2SM R06L/3000V3500FT FG OVC002 14/14 A3020 RMK AO2 SLP226
KDAY 051414Z 12012KT 1 1/4SM R06L/4000V5000FT BR OVC002 14/14 A3021 RMK AO2
KDAY 051434Z 13012KT 2SM R06L/5500VP6000FT BR OVC002 15/14 A3021 RMK AO2
KDAY 051451Z 12012KT 2 1/2SM BR OVC004 16/14 A3021 RMK AO2 SLP228 T01560144 52010
KDAY 051551Z 12011KT 4SM BR OVC006 17/15 A3020 RMK AO2 SLP224 T01670150
KDAY 051535Z 12010KT 4SM BR OVC006 17/14 A3020 RMK AO2
KDAY 051510Z 12012KT 3SM BR OVC004 16/14 A3021 RMK AO2
KDAY 051651Z 13011KT 5SM HZ BKN008 19/16 A3018 RMK AO2 SLP217 T01890156
KDAY 051700Z 14012KT 5SM HZ BKN010 19/16 A3018 RMK AO2 CIG 009V012
KDAY 051719Z 15009KT 5SM HZ SCT012 20/16 A3018 RMK AO2
KDAY 051751Z 12007KT 6SM HZ CLR 21/16 A3018 RMK AO2 SLP217 T02110161 10211 20133 55009
```

Rawinsonde data was not saved for this experiment.

Weather Data for 20 October 1998

```
KFFO 200955Z 21002KT 7SM SKC 02/02 A3026 RMK SLP255
KFFO 201055Z 22003KT 7SM SKC 01/00 A3028 RMK SLP261
KFFO 201155Z 22004KT 7SM MIFG SKC 01/00 A3029 RMK SLP265 53010
KFFO 201255Z 22004KT 7SM SKC 04/01 A3031 RMK SLP272
KFFO 201355Z 25005KT 7SM SKC 08/02 A3032 RMK SLP274
KFFO 201455Z 27006KT 7SM SKC 10/M01 A3032 RMK SLP274 51010

KDAY 200951Z 29008KT 10SM CLR 08/03 A3027 RMK AO2 SLP249 T00830028
KDAY 201051Z 28008KT 10SM CLR 07/02 A3028 RMK AO2 SLP254 T00720017
KDAY 201151Z 29009KT 10SM CLR 07/01 A3029 RMK AO2 SLP259 T00670011 10111 20067 53010
KDAY 201251Z 29010KT 10SM CLR 08/01 A3030 RMK AO2 VIS 2 1/2 RWY 6L SLP263 T00780011
KDAY 201351Z 29010KT 10SM CLR 10/02 A3031 RMK AO2 VIS 2 1/2 RWY 6L SLP268 T01000017
KDAY 201451Z 30010KT 10SM CLR 12/01 A3032 RMK AO2 SLP268 T01220011 51010
```

UPPER AIR DATA FOR: Wilmington OH, KILN FOR 12Z, 20-OCT-98

LEVEL (MB)	HEIGHT (FT)	TMP (F)	DPT (F)	DDFF (KTS)
472		2.3	-44.5	29538
500	18827	8.8	-42.9	31534
700	10207			32522
714		31.5	-33.3	
850	5074	41.7	-5.6	04012
852		42.1	-6.6	
871		44.2	-14.2	
880		43.5	-25.6	
885		43.2	-23.4	
896		42.4	-18.2	
918		44.4	-11.7	
925	2801	45.0	-9.8	04013
953		46.9	-3.9	
978		48.6	1.2	
987	SURF	42.8	4.1	04007
1000	690			

Weather Data for 11 November 1998

KFFO 110955Z 24015G21KT 7SM SKC 06/M03 A2999 RMK PK WND 25029/00 SLP160
KFFO 111055Z 25019G26KT 7SM SKC 05/M04 A3001 RMK PK WND 25027/14 SLP169
KFFO 111155Z 26014G22KT 10SM SCT250 05/M03 A3005 RMK PK WND 26026/14 SLP183 70032 8/008
9/003 53029
KFFO 111255Z 25017G22KT 10SM FEW040 FEW250 04/M03 A3008 RMK PK WND 27026/23 SLP194 8/508
9/101
KFFO 111355Z 26021G26KT 10SM FEW040 05/M04 A3012 RMK PK WND 26027/28 SLP206 8/500 9/100
KFFO 111455Z 26013G24KT 10SM FEW030 06/M03 A3016 RMK PK WND 26028/1357 SLP218 8/500 9/100
53034

KDAY 110951Z 24015G23KT 10SM CLR 04/M04 A2999 RMK AO2 PK WND 23029/0914 SLP158 T00441039
KDAY 111051Z 25028G34KT 10SM CLR 04/M04 A3002 RMK AO2 PK WND 25035/1036 SLP168 T00441039
KDAY 111151Z 25021G27KT 10SM CLR 03/M03 A3006 RMK AO2 PK WND 24035/1052 SLP181 70050
T00331033 10078 20033 53028
KDAY 111251Z 25022G32KT 10SM CLR 03/M03 A3008 RMK AO2 PK WND 25032/1243 SLP190 T00331033
KDAY 111351Z 25022G30KT 10SM CLR 04/M03 A3013 RMK AO2 PK WND 25034/1252 SLP207 T00391028
KDAY 111451Z 25021G24KT 10SM CLR 05/M02 A3016 RMK AO2 PK WND 25034/1352 SLP218 T00501022
53036

UPPER AIR DATA FOR: ILN FOR 12Z, 11-NOV-98

LEVEL (MB)	HEIGHT (FT)	TMP (F)	DPT (F)	DDFFF (KTS)
214	TROP	-88.1	-125.9	
100	53215	-74.7	-116.1	28044
135		-77.6	-117.2	29052
141		-74.7	-112.5	
150	44980	-65.0	-110.0	29550
173		-65.7	-101.7	
200	38976	-65.0	-101.2	30547
250	34219	-56.0	-88.4	30542
300	30249	-43.8	-83.4	29538
333		-35.9	-79.1	
400	23688	-18.6	-67.2	31534
500	18274	4.1	-42.7	
519		8.6	-45.9	
579		15.3	-27.9	32522
601		9.5	-60.7	
665		18.9	-54.9	
683		18.1	-44.9	04012
700	9800	20.3	-42.7	
763		26.1	-29.7	
850	4777	27.1	9.1	04013
871		26.4	13.8	
925	2568	34.2	16.2	04013
974		41.7	18.3	
979	SURF	42.1	24.8	04007
1000	1080			

Weather Data for 25 November 1998

KFFO 250955Z 18004KT 10SM FEW250 05/M03 A3008 RMK SLP192 8/008 9/001
 KFFO 251055Z 14003KT 10SM FEW250 04/M04 A3004 RMK SLP181 8/008 9/002
 KFFO 251155Z 17003KT 10SM FEW120 SCT250 04/M04 A3004 RMK SLP180 8/071 9/021 57015
 KFFO 251255Z 16004KT 7SM SCT100 BKN130 BKN250 05/M04 A3003 RMK SLP176 8/071 9/051
 KFFO 251355Z 17002KT 7SM BKN130 BKN150 OVC200 05/M02 A3002 RMK SLP174 8/077 9/062
 KFFO 251455Z 16005KT 7SM BKN130 BKN150 OVC200 07/M02 A2999 RMK SLP162 8/077 9/062 58017

 KDAY 250951Z 15010KT 10SM CLR 04/M04 A3008 RMK AO2 SLP188 T00441039
 KDAY 251051Z 14010KT 10SM CLR 03/M04 A3004 RMK AO2 SLP175 T00281039
 KDAY 251151Z 16009KT 10SM CLR 04/M04 A3003 RMK AO2 SLP174 T00441039 10050 20017 58018
 KDAY 251251Z 14009KT 10SM BKN200 04/M03 A3002 RMK AO2 SLP171 T00441033
 KDAY 251351Z 16009KT 10SM FEW095 OVC200 06/M03 A3001 RMK AO2 SLP166 T00561028
 KDAY 251451Z 16010KT 10SM OVC200 07/M03 A2998 RMK AO2 SLP158 T00721028 58016
 KDAY 251551Z 18011KT 10SM BKN060 09/M02 A2996 RMK AO2 SLP150 T00941017

98112512100 Data for ILN:

LEV	PR (mb)	H (m)	T (C)	TD (C)	DIR	SPD (kt)	THETA (K)	THETA E (K)	W (g/kg)
SFC	979.0		3.0	-3.0	150	11	277.83	286.52	3.13
1	975.0		4.8	-8.2			279.97	285.99	2.11
2	962.0		9.8	-9.2			286.10	291.92	1.98
3	943.0		11.4	-12.6			289.37	294.01	1.54
4	925.0	796	11.2	-11.8			290.76	295.81	1.67
5	901.0		10.8	-36.2			292.54	293.19	0.19
6	886.0		10.4	-16.6			293.54	297.20	1.18
7	876.0		10.2	-36.8			294.28	294.92	0.19
8	850.0	1498	9.6	-37.4	215	32	296.20	296.82	0.18
9	821.0		8.8	-37.2			298.31	298.97	0.19
10	791.0		7.8	-14.2			300.44	305.50	1.61
11	700.0	3086	1.0	-16.0	235	33	303.59	308.60	1.57
12	674.0		-1.5	-19.5			304.10	308.92	1.21
13	667.0		-2.1	-15.1			304.33	309.98	1.77
14	647.0		-3.5	-30.5			305.41	307.00	0.47
15	627.0		-5.5	-15.5			305.88	311.71	1.82
16	613.0		-5.5	-23.5			307.86	310.98	0.94
17	608.0		-5.5	-20.5			308.58	312.64	1.23
18	588.0		-8.1	-20.1			308.52	312.85	1.32
19	579.0		-7.3	-40.3			310.82	311.53	0.20
20	565.0		-7.7	-40.7			312.53	313.24	0.19
21	500.0	5710	-15.5	-41.5	260	37	314.14	314.88	0.20
22	447.0		-21.9	-45.9			316.31	316.84	0.14
23	400.0	7350	-27.7	-56.7	265	57	318.99	319.16	0.04
24	354.0		-32.9	-58.9			323.33	323.48	0.04
25	346.0		-34.3	-45.3			323.56	324.29	0.19
26	331.0		-37.1	-48.1			323.84	324.41	0.15
27	324.0		-37.5	-43.5			325.28	326.22	0.25
28	300.0	9360	-41.7	-45.8	260	72	326.59	327.40	0.21
29	250.0	10570	-51.1	-57.1	260	67	330.10	330.37	0.07
30	200.0	11990	-62.9	-67.9	270	80	333.15	333.24	0.02
31	191.0		-65.1	-70.0			334.04	334.10	0.02
32	174.0		-66.5	-71.5			340.75	340.81	0.01
33	150.0	13740	-63.3	-70.3	275	75	361.03	361.12	0.02
34	125.0		-66.7	-76.7			374.20	374.24	0.01
35	100.0	16200	-65.9	-78.9	285	53	400.40	400.44	0.01
36	70.0	18370	-65.7	-82.7	280	32	443.83	443.86	0.01
37	50.0	20420	-61.5	-83.5	270	21	498.55	498.60	0.01
38	30.0	23590	-58.9	-82.9	250	11	584.07	584.16	0.01
39	20.0	26160	-54.3	-80.3	260	22	669.96	670.22	0.03
TROP	174.0		-66.5	-71.5	260	71			

Appendix 2: Event Information for Part 2

In this Appendix, Tables A2.1 through A2.4 list information about each event for the four days of testing. Information includes the type of ordnance, the amount and type of explosive, the number of scans or measurements collected for that event, the resolution of the data, and the aperture and gain setting.

Table A2.1. Information on the explosion events that occurred on day 1.

<u>Event Number</u>	<u>Type of Ordnance</u>	<u>Distance (m)</u>	<u>Ordnance Properties</u>	<u>Number of Scans</u>	<u>Resolution (cm-1)</u>	<u>Aperture Gain</u>
1	Mk 82	4312	192 lbs of Tritonal	10	16	.8 / A
2	Mk 82	4311	192 lbs of Tritonal	2	2	.8 / A
3	Mk 82	4314	192 lbs of Tritonal	4	16	.8 / A
4	Mk 82	4309	192 lbs of Tritonal	1	2	.8 / A
5	Mk 82	4319	192 lbs of Tritonal	5	16	.8 / A
6	Mk 82	4306	192 lbs of Tritonal	2	2	.8 / A
7	Mk 82	4306	192 lbs of Tritonal	5	16	.8 / A
8	Mk 82	4314	192 lbs of Tritonal	1	2	.8 / A
9	Mk 82	4248	192 lbs of Tritonal	5	16	.8 / A
10	Mk 82	4257	192 lbs of Tritonal	2	2	.8 / A
11	Mk 82	4257	192 lbs of Tritonal	10	16	.8 / A
12	Mk 82	4278	192 lbs of Tritonal	2	2	.8 / A
13	Mk 82	4332	192 lbs of Tritonal	7	16	.8 / A
14	Mk 82	4378	192 lbs of Tritonal	1	2	1.1 / A
15	Mk 82	4444	192 lbs of Tritonal	5	16	1.6 / A
16	Mk 82	4505	192 lbs of Tritonal	2	2	3.2 / A

Table A2.2. Information on the explosion events that occurred on day 2.

<u>Event Number</u>	<u>Type of Ordnance</u>	<u>Distance (m)</u>	<u>Ordnance Properties</u>	<u>Number of Scans</u>	<u>Resolution (cm-1)</u>	<u>Aperture Gain</u>
17	Mk 82	4713	192 lbs of Tritonal	13	16	3.2 / A
18	Mk 82	4714	192 lbs of Tritonal	2	2	3.2 / A
19	Mk 82	4771	192 lbs of Tritonal	1	16	3.2 / A
20	Mk 82	4785	192 lbs of Tritonal	3	2	3.2 / A
21	Mk 82	4789	192 lbs of Tritonal	12	16	3.2 / A
22	Mk 82	4801	192 lbs of Tritonal	3	2	3.2 / A
23	Mk 82	4814	192 lbs of Tritonal	13	16	3.2 / A
24	Mk 82	4844	192 lbs of Tritonal	3	2	3.2 / A
25	Mk 82	4862	192 lbs of Tritonal	14	16	3.2 / A
26	Mk 82	4867	192 lbs of Tritonal	3	2	3.2 / A
27	Mk 82	4777	192 lbs of Tritonal	10	16	3.2 / A
28	Mk 82	4819	192 lbs of Tritonal	2	2	3.2 / A
29	Mk 82	4876	192 lbs of Tritonal	9	16	3.2 / A
30	Mk 82	4920	192 lbs of Tritonal	2	2	3.2 / A
31	Mk 82	4997	192 lbs of Tritonal	11	16	3.2 / A
32	Mk 82	5064	192 lbs of Tritonal	2	2	3.2 / A

Table A2.3. Information on the explosion events that occurred on day 3.

<u>Event Number</u>	<u>Type of Ordnance</u>	<u>Distance (m)</u>	<u>Ordnance Properties</u>	<u>Number of Scans</u>	<u>Resolution (cm-1)</u>	<u>Aperture Gain</u>
33	HARM	2586	45 lbs PBXN-107	No Data	No Data	No Data
34	HARM	2598	45 lbs PBXN-107	13	16	3.2 / A
35	HARM	2602	45 lbs PBXN-107	1	2	3.2 / A
36	HARM	2613	45 lbs PBXN-107	6	16	3.2 / A
37	HARM	2608	45 lbs PBXN-107	No Data	No Data	No Data
38	HARM	2600	45 lbs PBXN-107	No Data	No Data	No Data
39	HARM	2588	45 lbs PBXN-107	No Data	No Data	No Data
40	HARM	2541	45 lbs PBXN-107	No Data	No Data	No Data
41	TLAM (WDU-36)	2708	268 lbs PBXN- 107 Type 2	1	16	3.2 / A
42	TLAM (WDU-36)	2733	268 lbs PBXN- 107 Type 2	21	16	3.2 / A
43	TLAM (WDU-25)	2733	375 lbs PBXW- 109 1	15	16	3.2 / A
44	TLAM (WDU-25)	2757	375 lbs PBXW- 109 1	4	2	3.2 / A
45	Mk 84	3578	945 lbs H-6	11	16	3.2 / A
46	Mk 84	3490	945 lbs H-6	1	2	3.2 / A
47	Mk 84	3433	945 lbs H-6	18	16	3.2 / A
48	Mk 84	3378	945 lbs H-6	3	2	3.2 / A

Table A2.4. Information on the explosion events that occurred on day 4.

<u>Event Number</u>	<u>Type of Ordnance</u>	<u>Distance (m)</u>	<u>Ordnance Properties</u>	<u>Number of Scans</u>	<u>Resolution (cm-1)</u>	<u>Aperture Gain</u>
49	TLAM (WDU-36)	3293	268 lbs PBXN- 107 Type 2	9	16	3.2 / A
50	TLAM (WDU-36)	3233	268 lbs PBXN- 107 Type 2	2	16	3.2 / A
51	Mk 84	3275	945 lbs H-6	8	16	3.2 / A
52	Mk 83	3239	375 lbs H-6	7	16	3.2 / A
53	TLAM (WDU-36)	3156	268 lbs PBXN- 107 Type 2	9	16	3.2 / A
54	TLAM (WDU-25)	3083	375 lbs PBXW- 109 Type 1	10	16	3.2 / A
55	Mk 84	3192	945 lbs H-6	13	16	3.2 / A
56	Mk 83	3158	375 lbs H-6	12	2	3.2 / A
57	2 x Mk 82	3663	2 x 192 lbs of Tritonal	11	16	3.2 / A
58	2 x Mk 82	3569	2 x 192 lbs of Tritonal	9	16	3.2 / A
59	2 x Mk 82	3466	2 x 192 lbs of Tritonal	9	16	3.2 / A
60	Mk 82	3354	192 lbs of Tritonal	11	16	3.2 / A
61	Mk 82	3214	192 lbs of Tritonal	8	16	3.2 / A
62	6 x Mk 82	3194	6 x 192 lbs of Tritonal	No Data	No Data	No Data
63	6 x Mk 82	3276	6 x 192 lbs of Tritonal	14	16	3.2 / A
64	6 x Mk 82	3429	6 x 192 lbs of Tritonal	14	16	3.2 / A
A	C-4	437	16 lbs C-4	6	16	3.2 / A
B	C-4	438	16 lbs C-4	6	16	3.2 / A
C	C-4	304	8 lbs C-4	4	16	3.2 / A
D	C-4	304	8 lbs C-4	1	2	3.2 / A

Appendix 3: Additional Spectral Plots of Explosion Events

Figures A3-1a through A3-1c are the plots of event 1 involving a Mk 82 bomb. It is unusual that Figure A3-1a and Figure A3-1b have the same intensity over the 0.279 seconds between the two scans. It is believed the peak occurred between these two data points. Figure A3-1c shows that after 0.555 seconds, the radiance decreased by a factor of six, but the observed peaks are similar to those seen in the first two scans. Two more Mk 82 events are shown in Figures A3-2a and A3-2b and Figures A3-3a and A3-3b for which only two scans per event are shown. There is a strong similarity between the observed peaks and overall shape. There was also a uniform decrease in radiance in the bands on either side of the CO₂ absorption band. Figures A3-4 through A3-7 are plots of additional Mk 82 events. These four plots were selected to provide further comparison of Mk 82 events. These plots are not necessarily of the peak of the event, but they are the plots of the scan containing the greatest radiance measured for the respective event.

Figures A3-8a through A3-9b are spectral plots of the High-speed Anti-Radiant Missile (HARM) missile explosions. The shape is noticeably different from the Mk 82 signature as the radiance between 2500 and 3000 cm⁻¹ is about half that of the peak near 2172cm⁻¹ as opposed to the Mk 82 plot where the radiance was approximately the same on either side of the CO₂ absorption feature. The radiance between 2500 to 3000 cm⁻¹ is significantly lower than that of the Mk 82, likely due to a smaller quantity of explosive (Appendix 2). Two additional differences are the peaks observed at 2172 and 2402 cm⁻¹ attributable to O₃ and CH₄ respectively. These were not identified on Mk 82 plots, but

there are numerous peaks observed on the HARM that were also observed on the Mk 82 events (*e.g.*, 2219 cm^{-1} due to CO_2).

The spectral plots of the Tomahawk Land Attack Missile or TLAM (WDU-36) are displayed in Figures A3-10a through Figure A3-11. It is difficult to tell the difference between this warhead and the Mk 82 by comparing observed peaks or spectral features alone. It is necessary to compare the measured radiance values of the TLAM (WDU-36) with the other bomb types for identification.

Temporal characteristics of the TLAM (WDU-25) are seen in Figures A3-12a through A3-12c and A3-13a through A3-13d. In both cases the TLAM (WDU-25) spectral plots were characterized by a slower decrease in radiance around the peak at 2155 cm^{-1} when compared to the spectral band between $2500\text{--}3000\text{ cm}^{-1}$ as seen for the HARM missile. For example, Figures A3.8a and A3.12b are very similar.

Plots of only two Mk 84 events were available. Plots of these two events were inconsistent. In Figures A3-14a through A3-14f, the uniform buildup of observed radiance that was actually the fireball generated after the short-lived peak intensity that occurred between scans of the spectrometer as determined by the radiometer data. In Figure A3-14d, the peak around 2156 cm^{-1} increased to almost twice that of the peaks between 2500 and 3000 cm^{-1} . The second Mk 84 event could be confused with a Mk 82 event, and it does not display the same temporal characteristic as the first Mk 84 event. No useful means for identification of the Mk 84 was determined with data from these two events. Further comparison with radiometric data is needed to determine if the radiance measured by the spectrometer was associated with the explosion or with the fireball after the peak.

Data for only one Mk 83 event is available as shown in Figures A3-16a to A3-16g. The relatively slow increase in radiance in the 2500 cm^{-1} to 3000 cm^{-1} is again likely due to the fireball after the explosion. The radiometric data showed the peak intensity occurred in 0.1 sec that likely occurred between scans taken by the spectrometer.

Figures A3-17a through A3-18b display spectral plots for C-4 plastic explosives. The carbon dioxide absorption is less, because the explosions occurred only 300 meters from the spectrometer as opposed to 3000 to 5000 meters for the other events. Also, in Figure A3-17a through A3-17c, 16 pounds of C-4 was detonated. The lower radiance compared to other events over $2500\text{-}3000\text{ cm}^{-1}$ is due to the lesser quantity of explosive discharged.

The final two figures are provided to show what was believed to be radio frequency interference (RFI). At times, a scan was rendered useless by what was believed to be RFI caused by the remote detonators used by EOD. It is believed these plots are RFI. Examples of RFI are shown in Figure A3-19a. Figure A3-19b, is provided to show that the background radiance was negligible when compared to typical scale of radiance observed during an explosion.

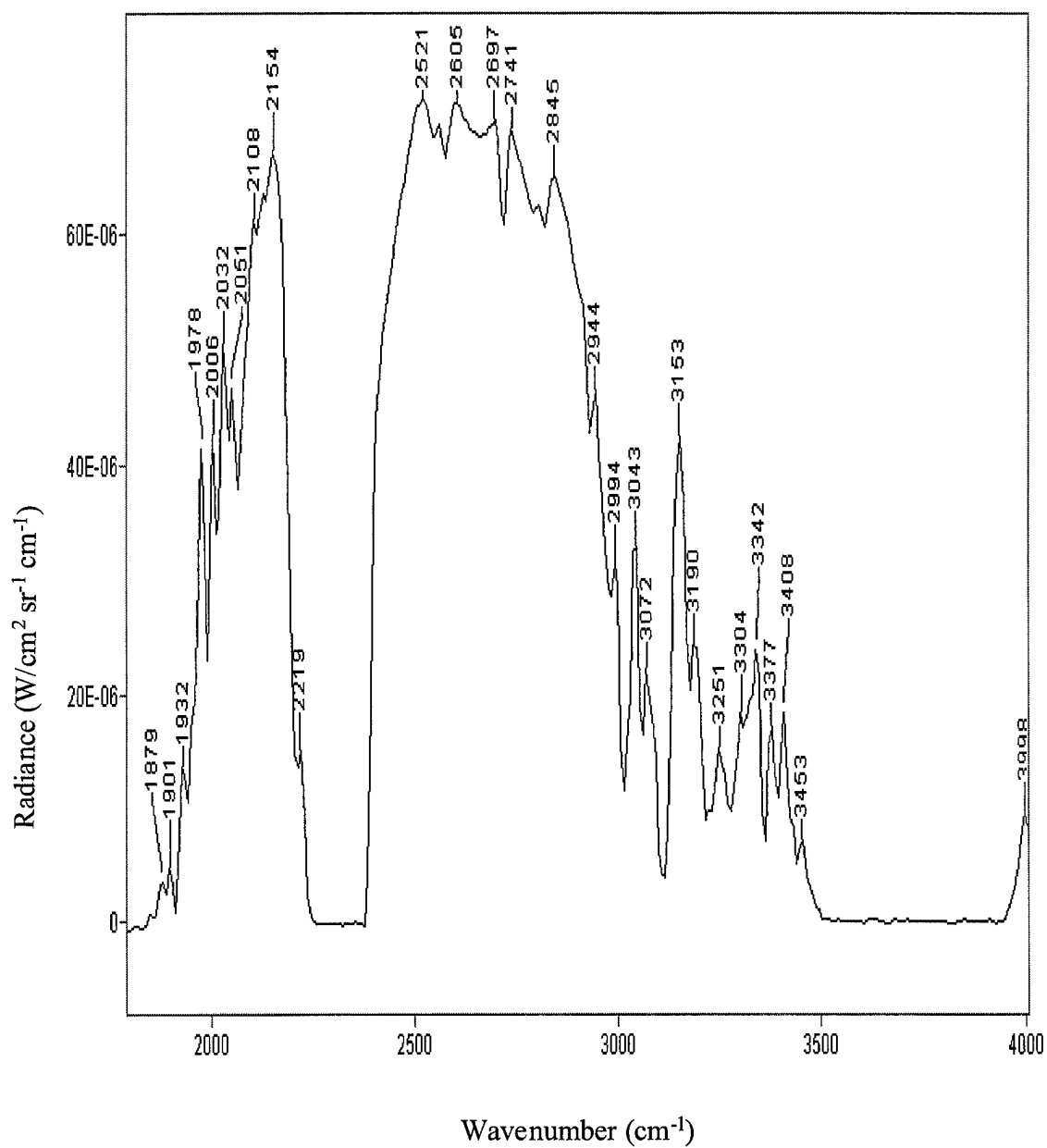


Figure A3.1a. Initial spectral signature of event 1, Mk 82 bomb explosion.

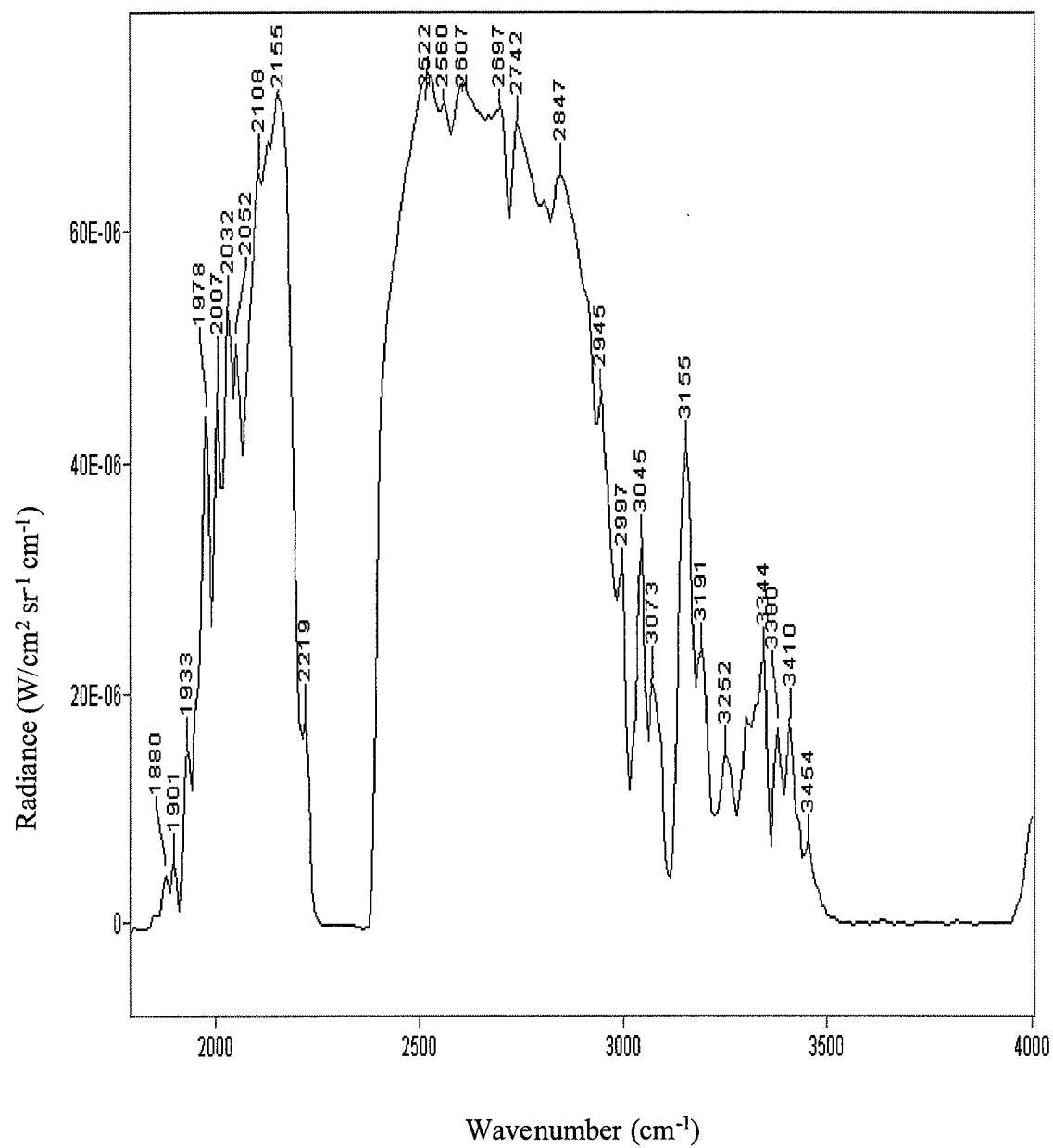


Figure A3.1b. Spectral signature of event 1, Mk 82 bomb explosion 0.279 seconds after Figure A3.1a.

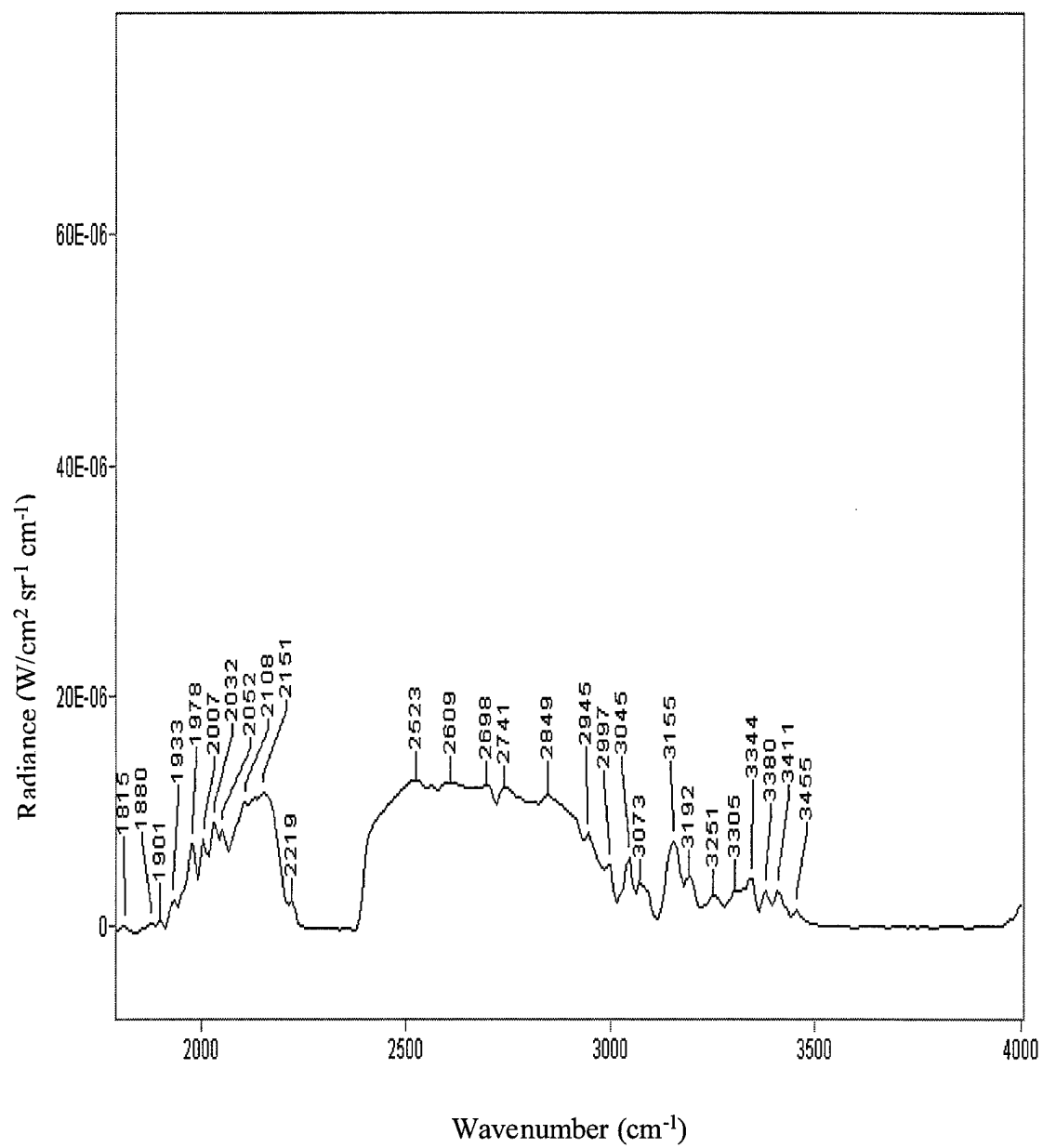


Figure A3.1c. Spectral signature of event 1, Mk 82 bomb explosion 0.555 seconds after Figure A3.1a.

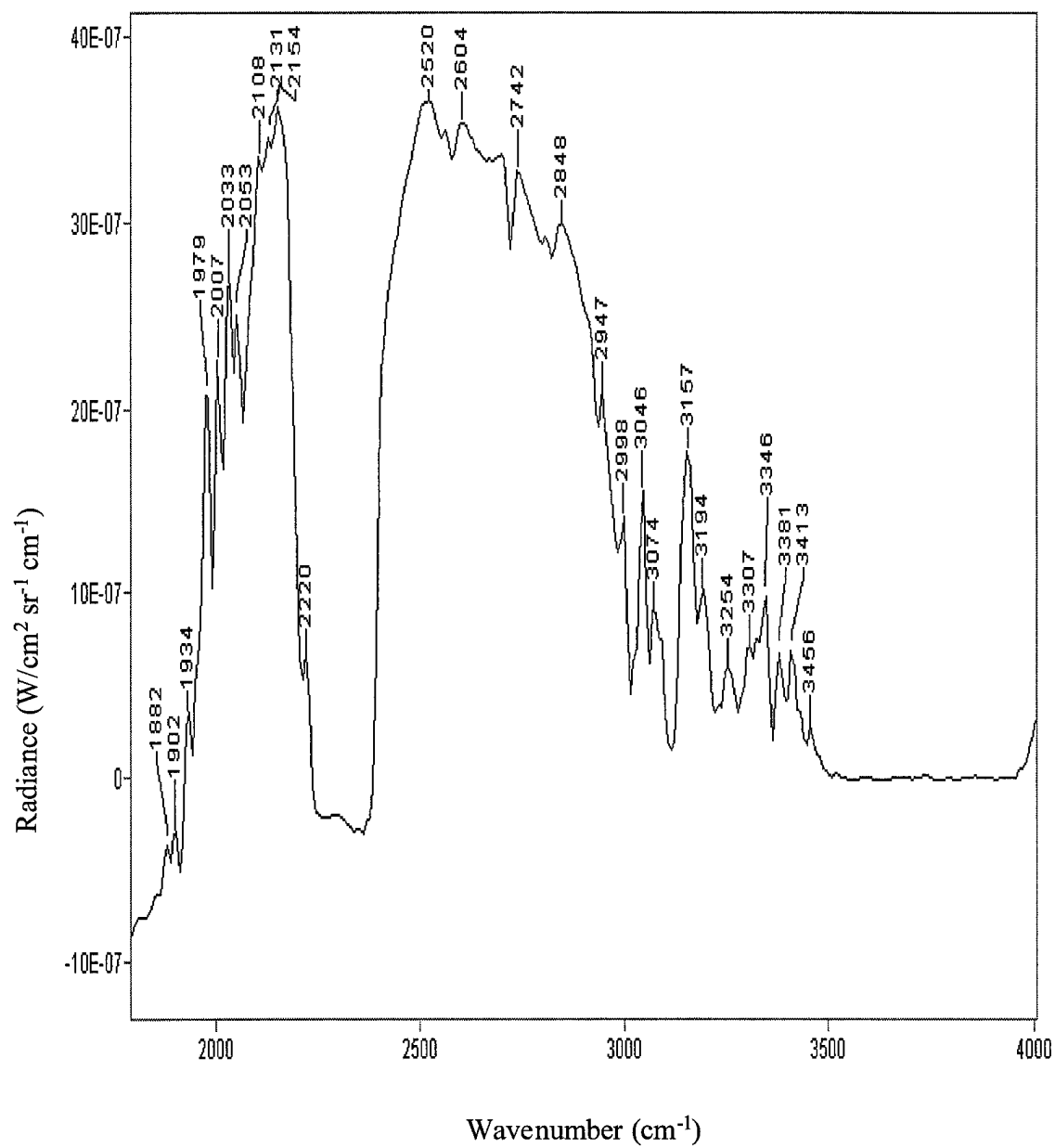


Figure A3.2a. Initial spectral signature retrieved of event 5, Mk 82 bomb explosion.

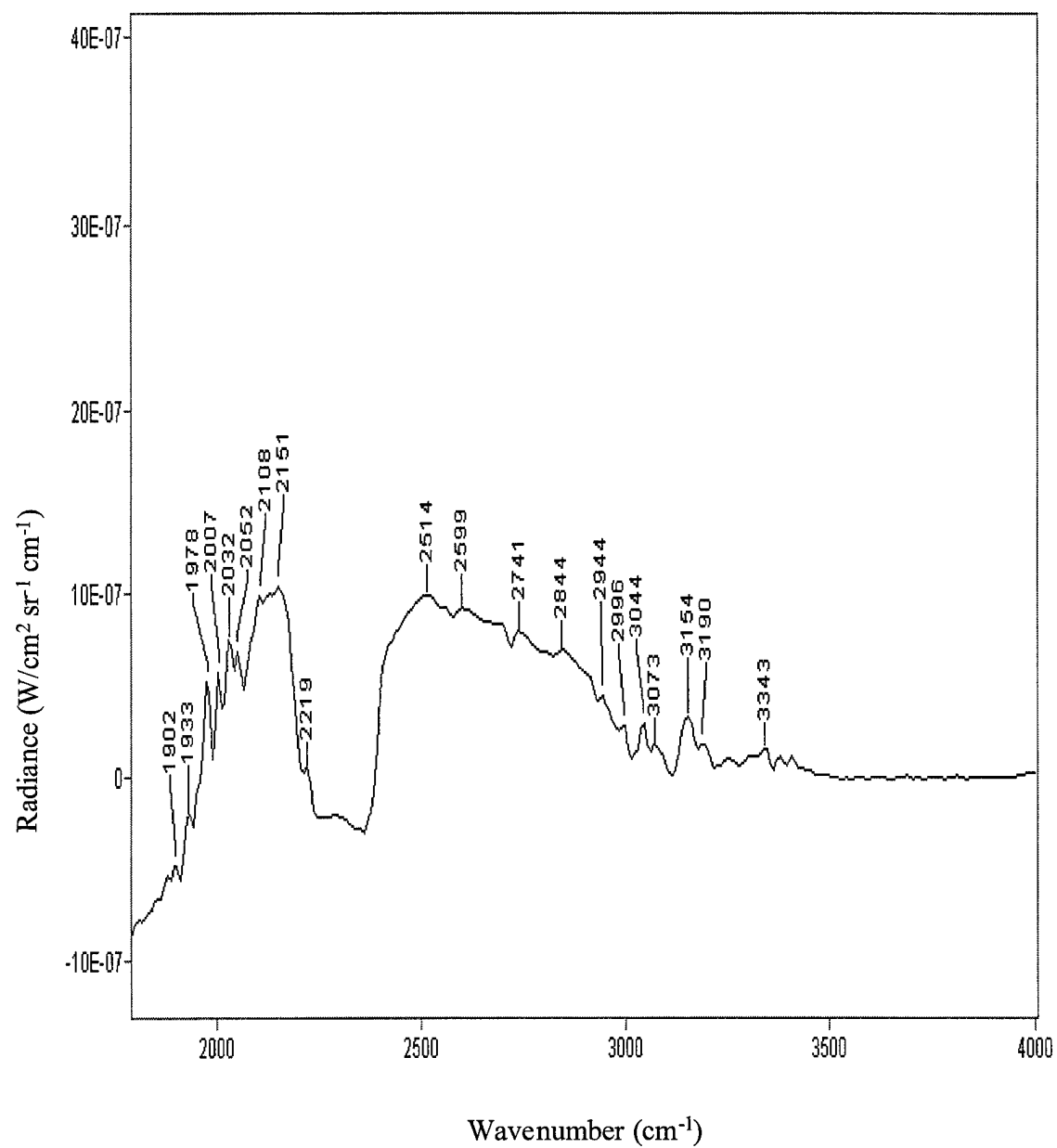


Figure A3.2b. Spectral signature of event 5, Mk 82 bomb explosion 0.279 seconds after Figure A3.2a.

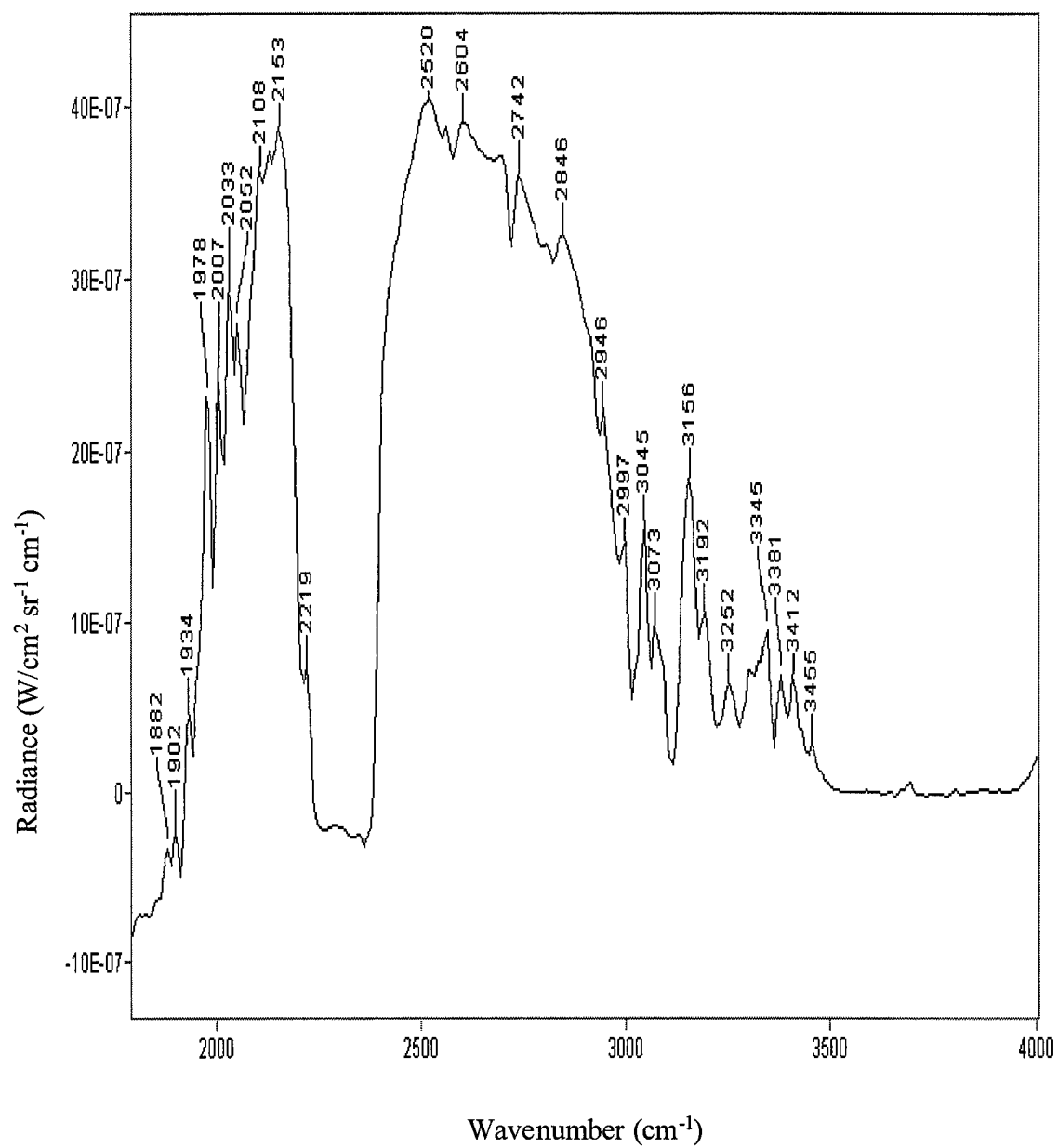


Figure A3.3a. Initial spectral signature retrieved of event 9, Mk 82 bomb explosion.

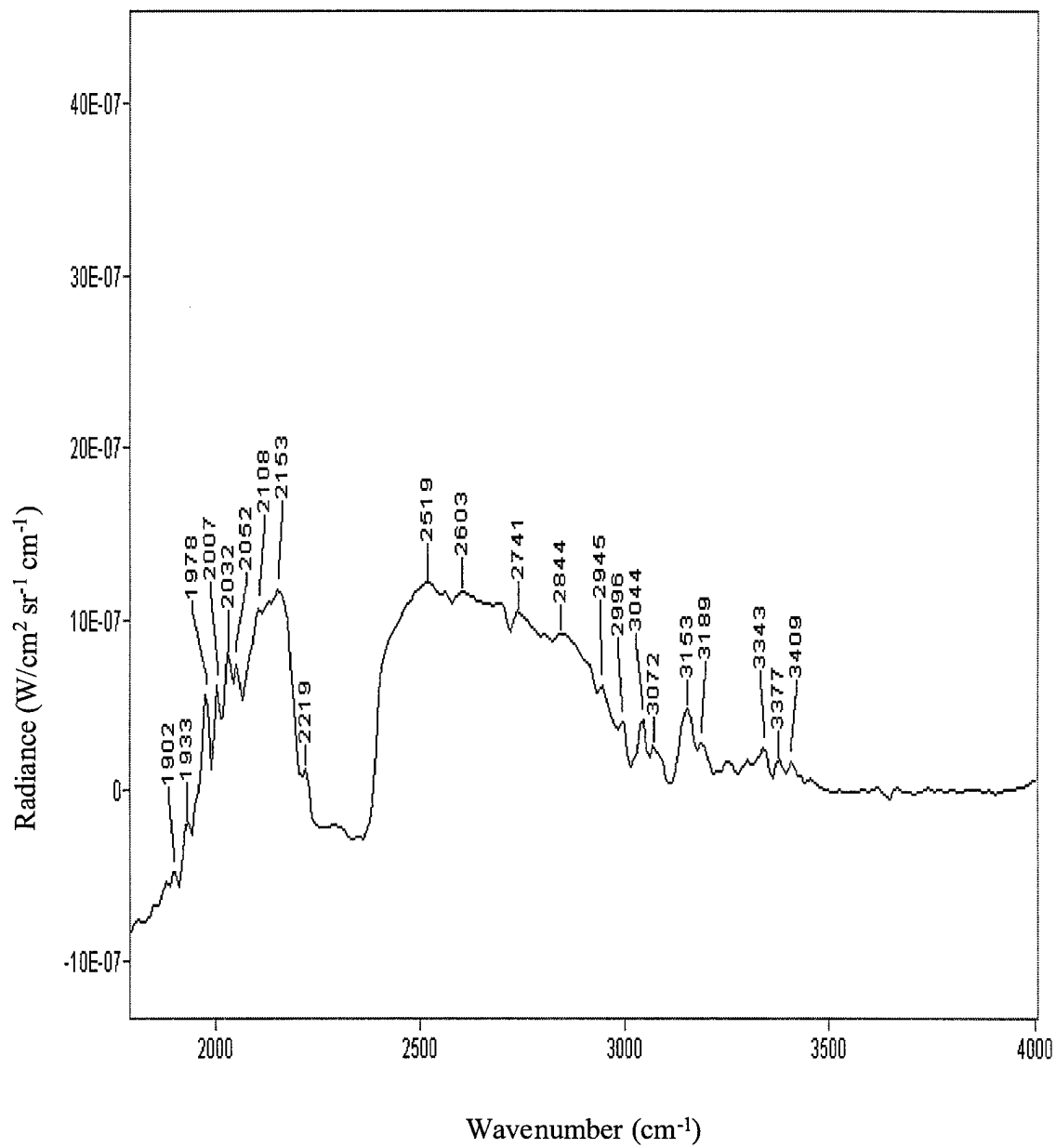


Figure A3.3b. Spectral signature of event 9, Mk 82 bomb explosion 0.278 seconds after Figure A3.3a.

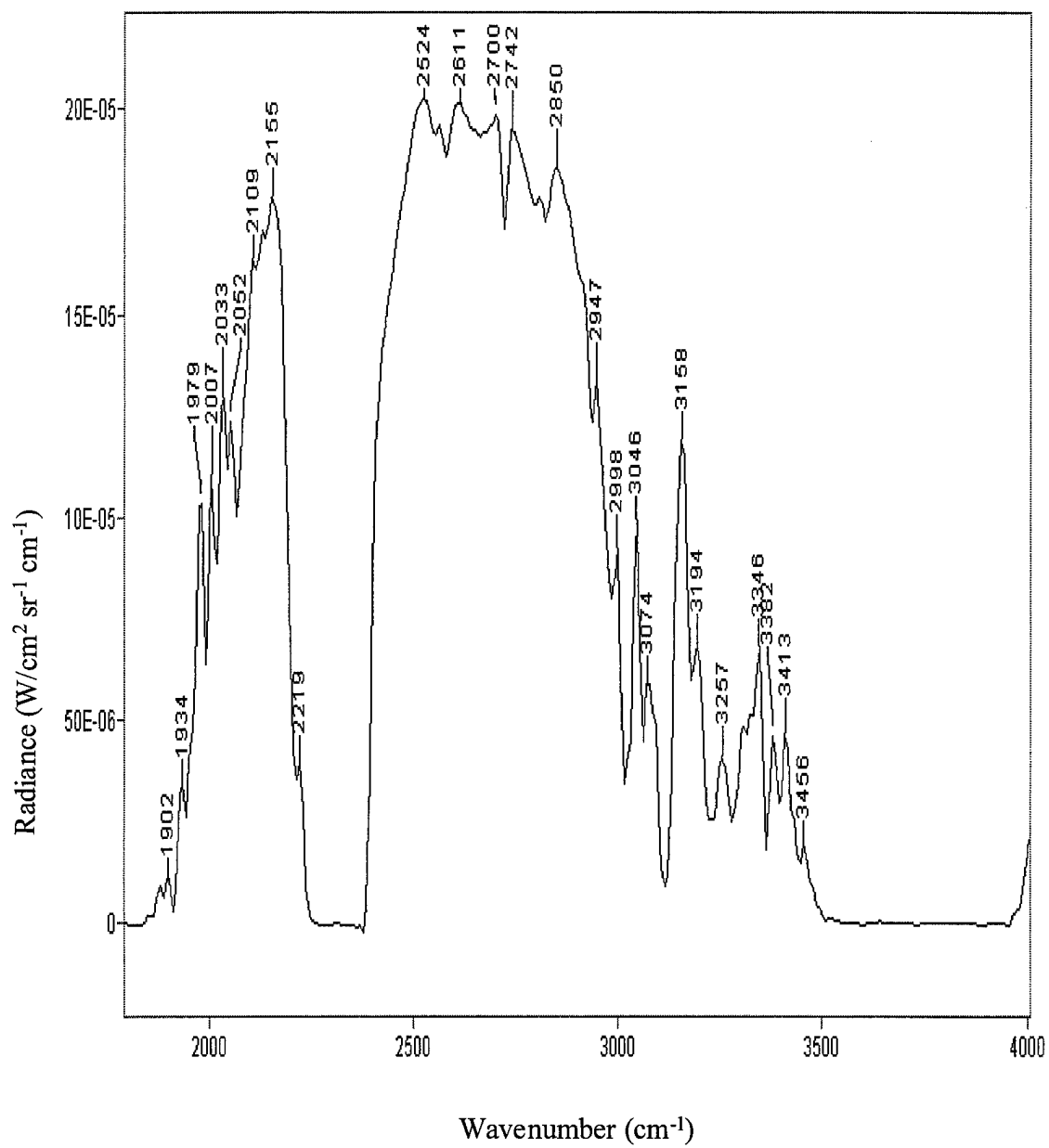


Figure A3.4. Spectral signature of peak radiance observed for event 11, Mk 82 bomb explosion.

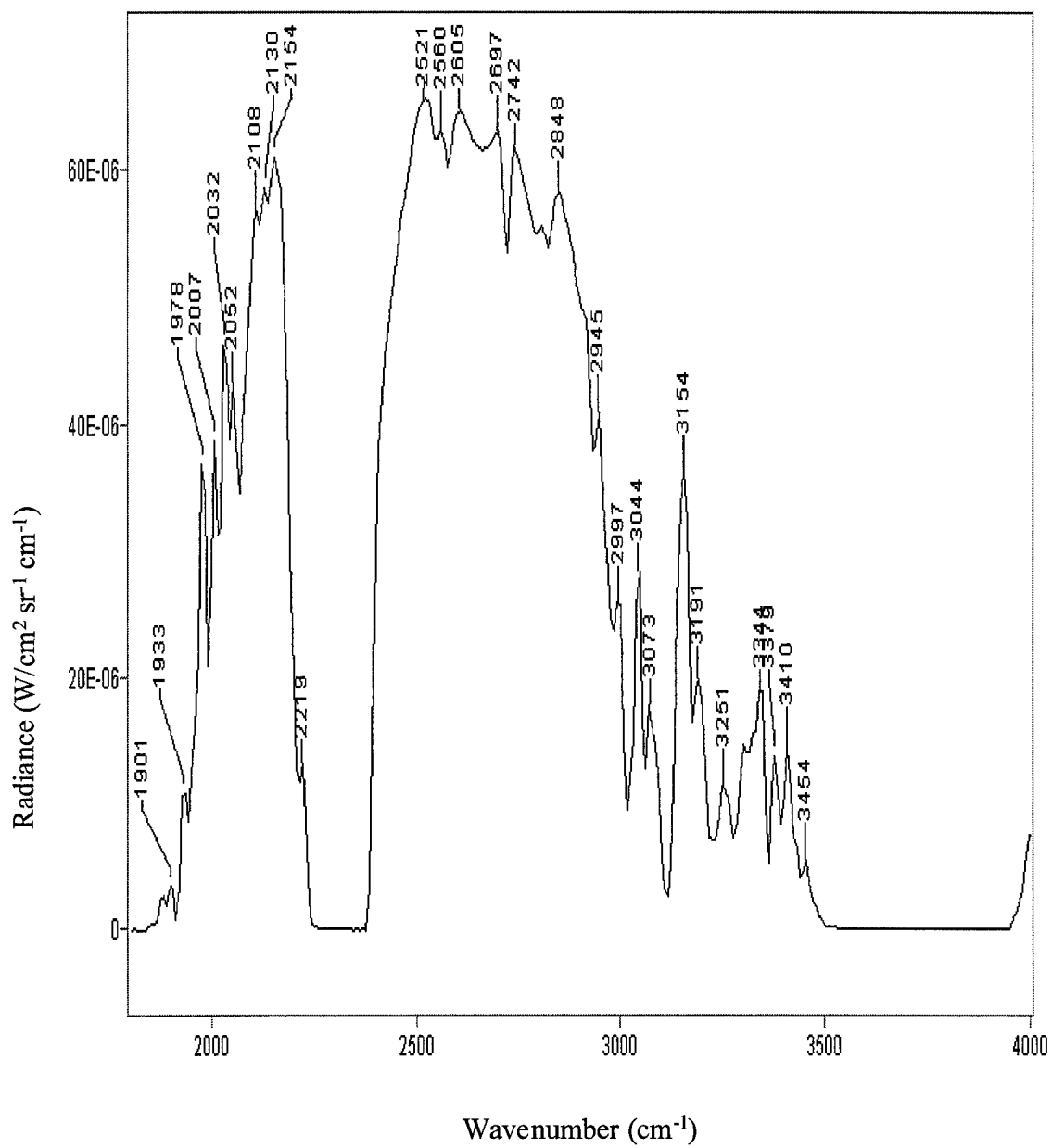


Figure A3.5. Spectral signature of peak radiance observed for event 21, Mk 82 bomb explosion.

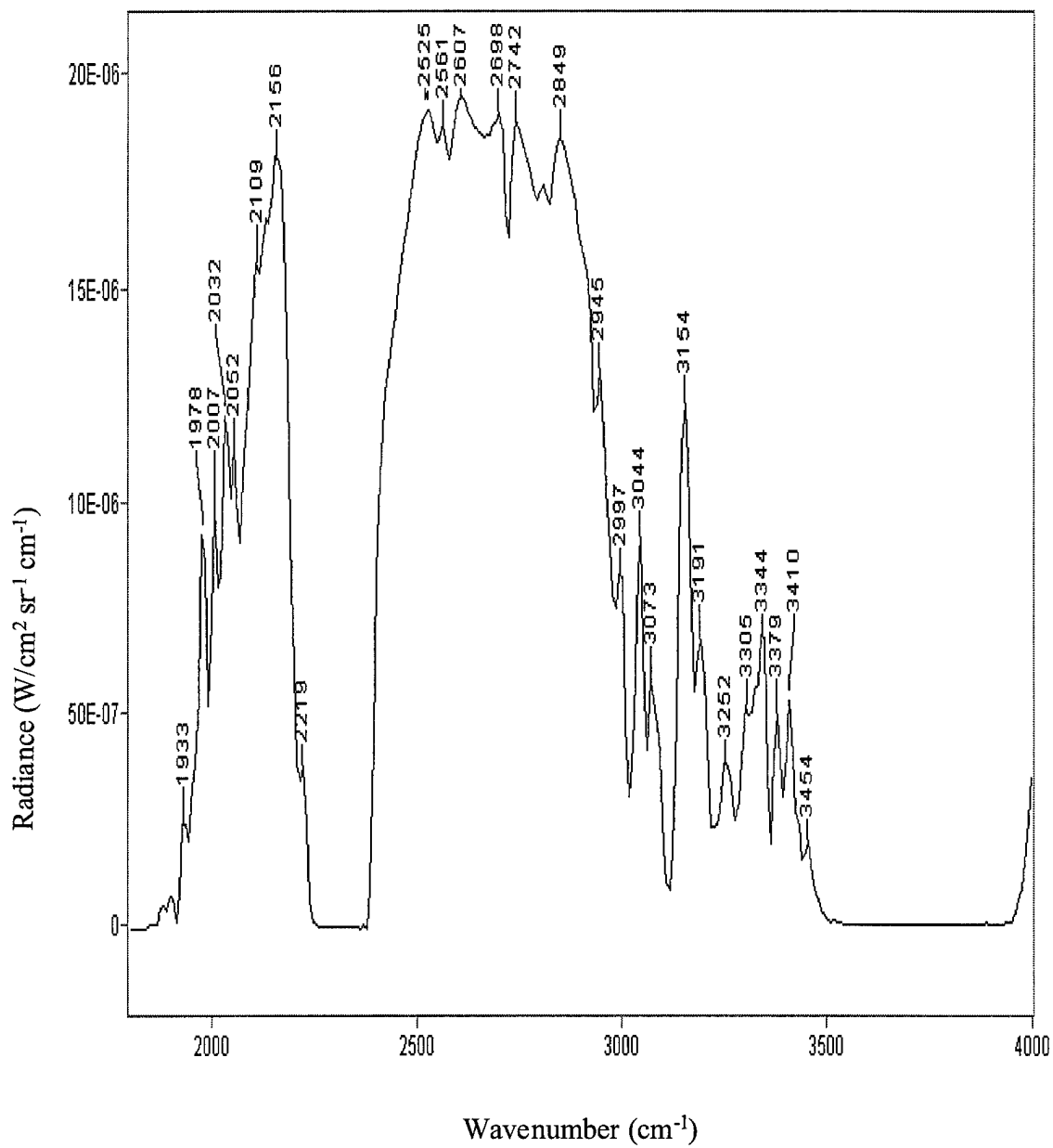


Figure A3.6. Spectral signature of peak radiance observed for event 23, Mk 82 bomb explosion.

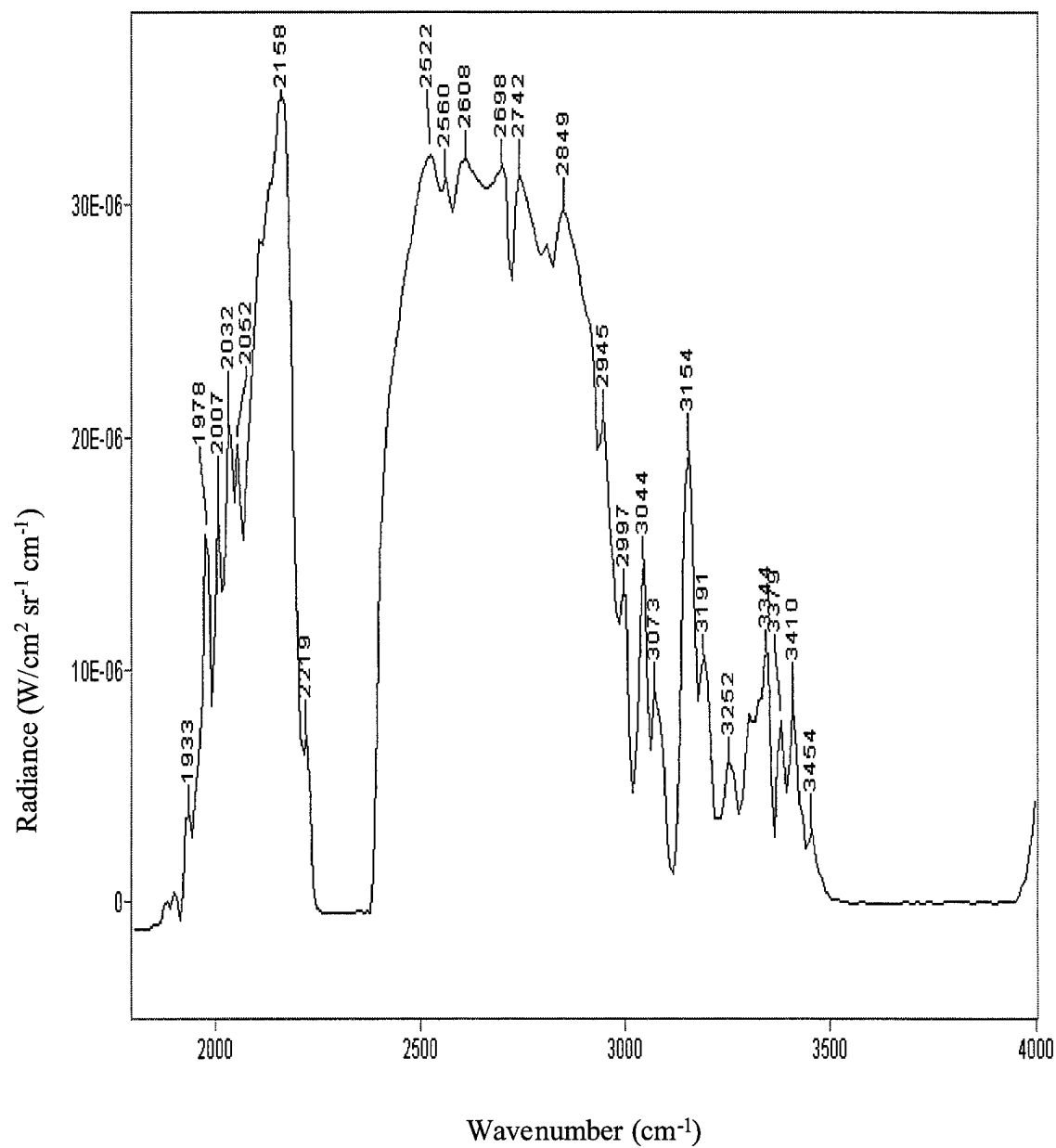


Figure A3.7. Spectral signature of peak radiance observed for event 29, Mk 82 bomb explosion.

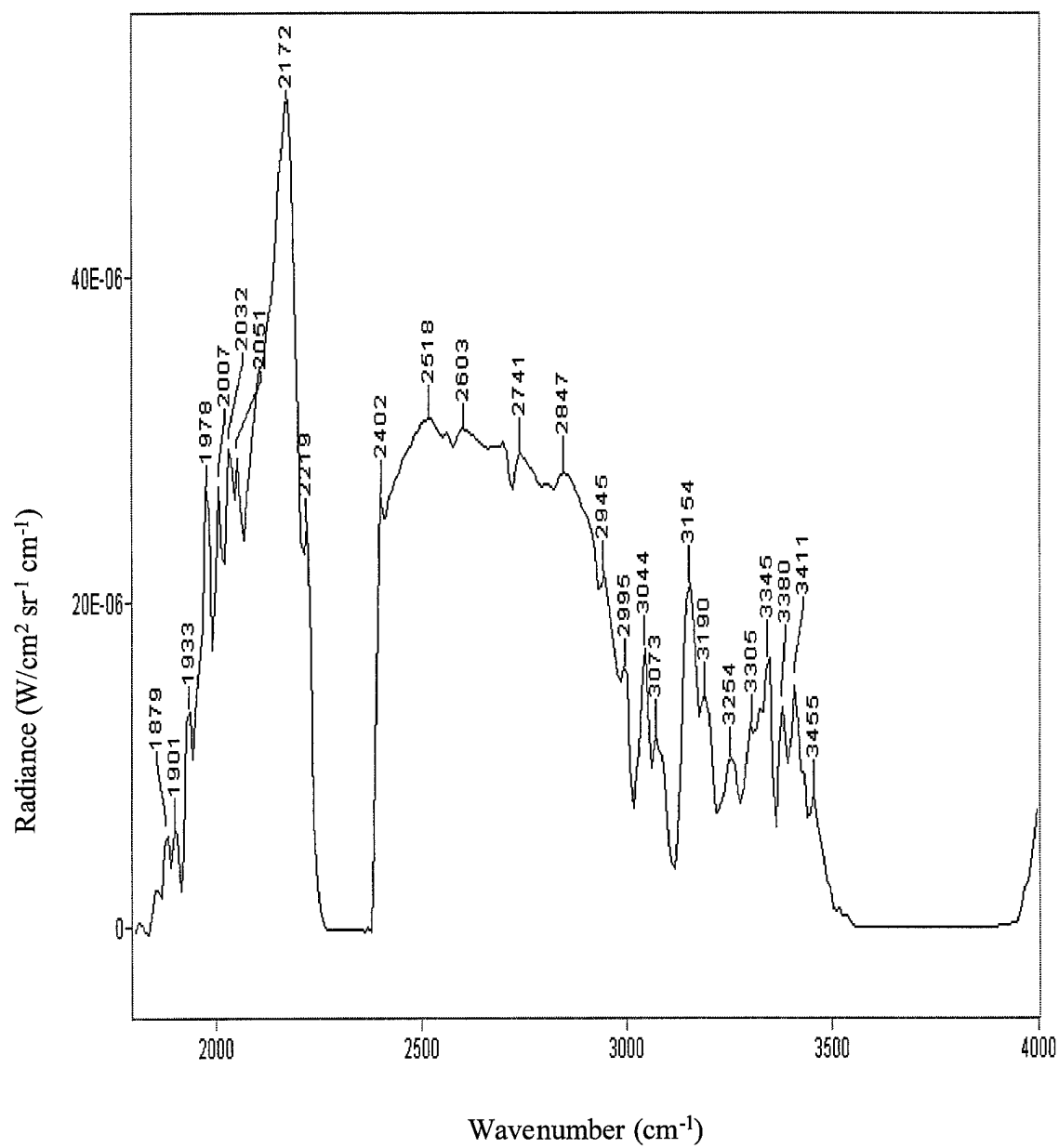


Figure A3.8a. Initial spectral signature retrieved of event 34, HARM missile.

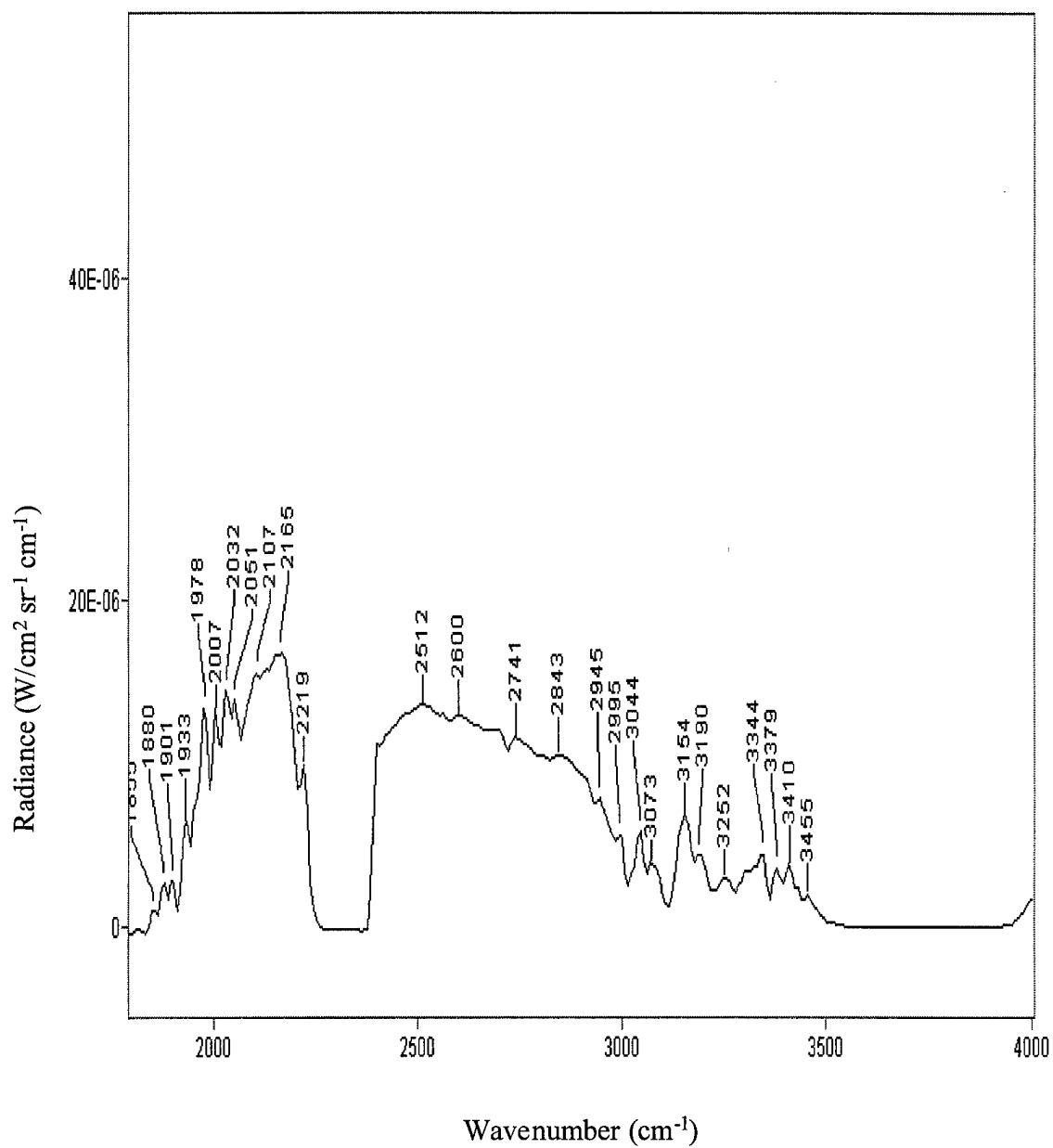


Figure A3.8b. Spectral signature of event 34, HARM missile explosion 0.278 seconds after Figure A3.8a.

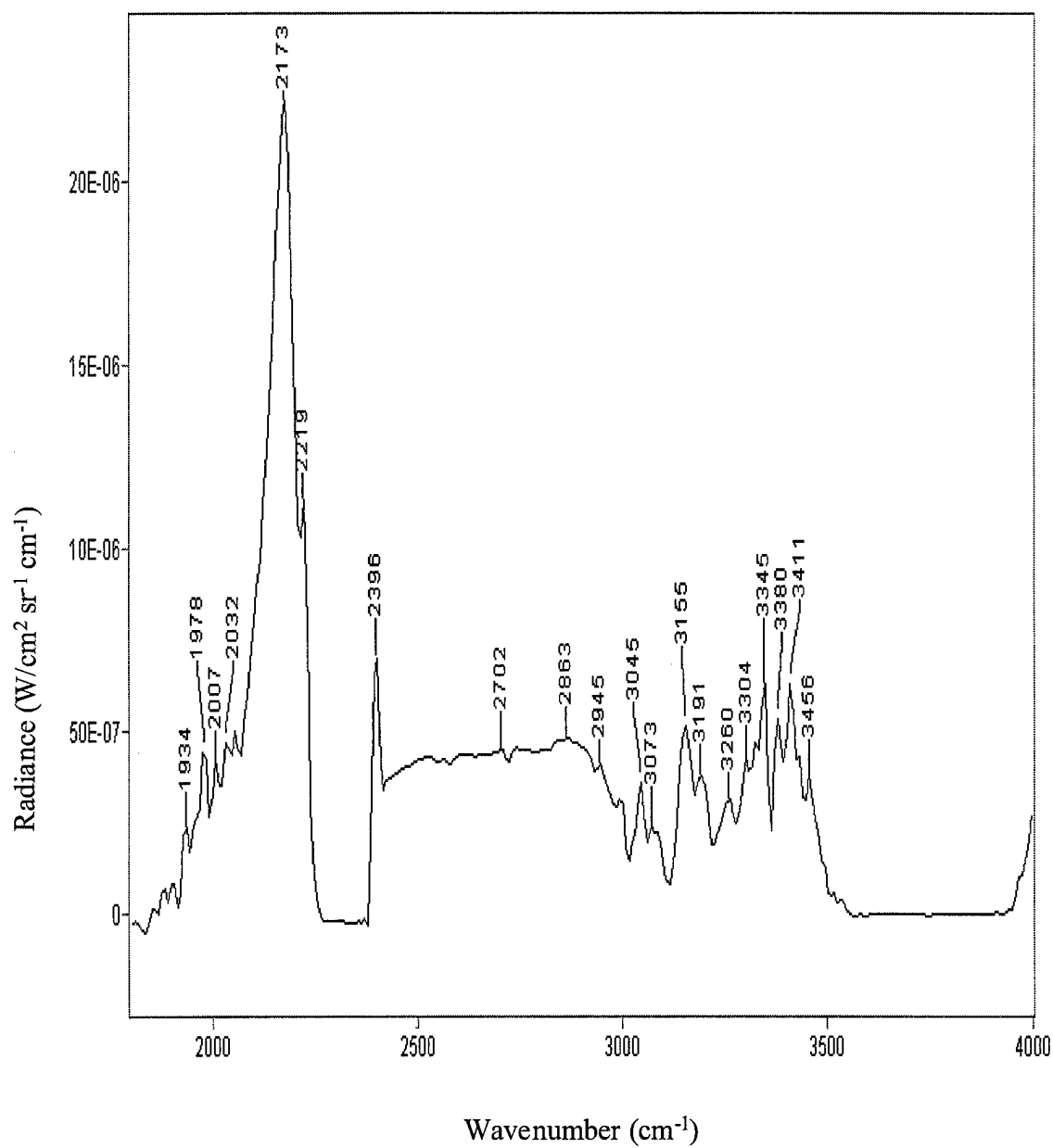


Figure A3.9a. Initial spectral signature retrieved of event 36, HARM missile explosion.

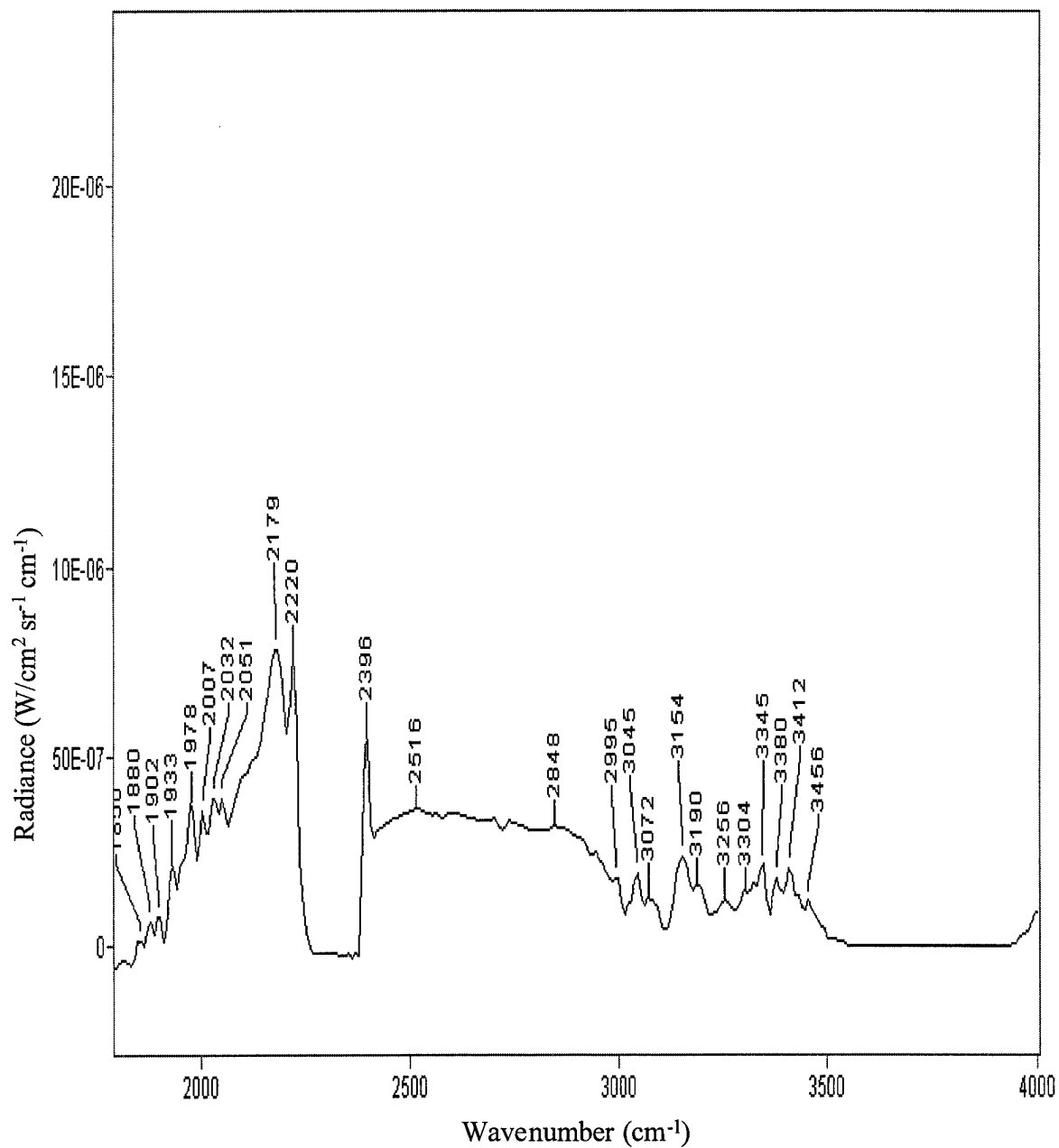


Figure A3.9b. Spectral signature of event 36, HARM missile explosion 0.278 seconds after Figure A3.9a.

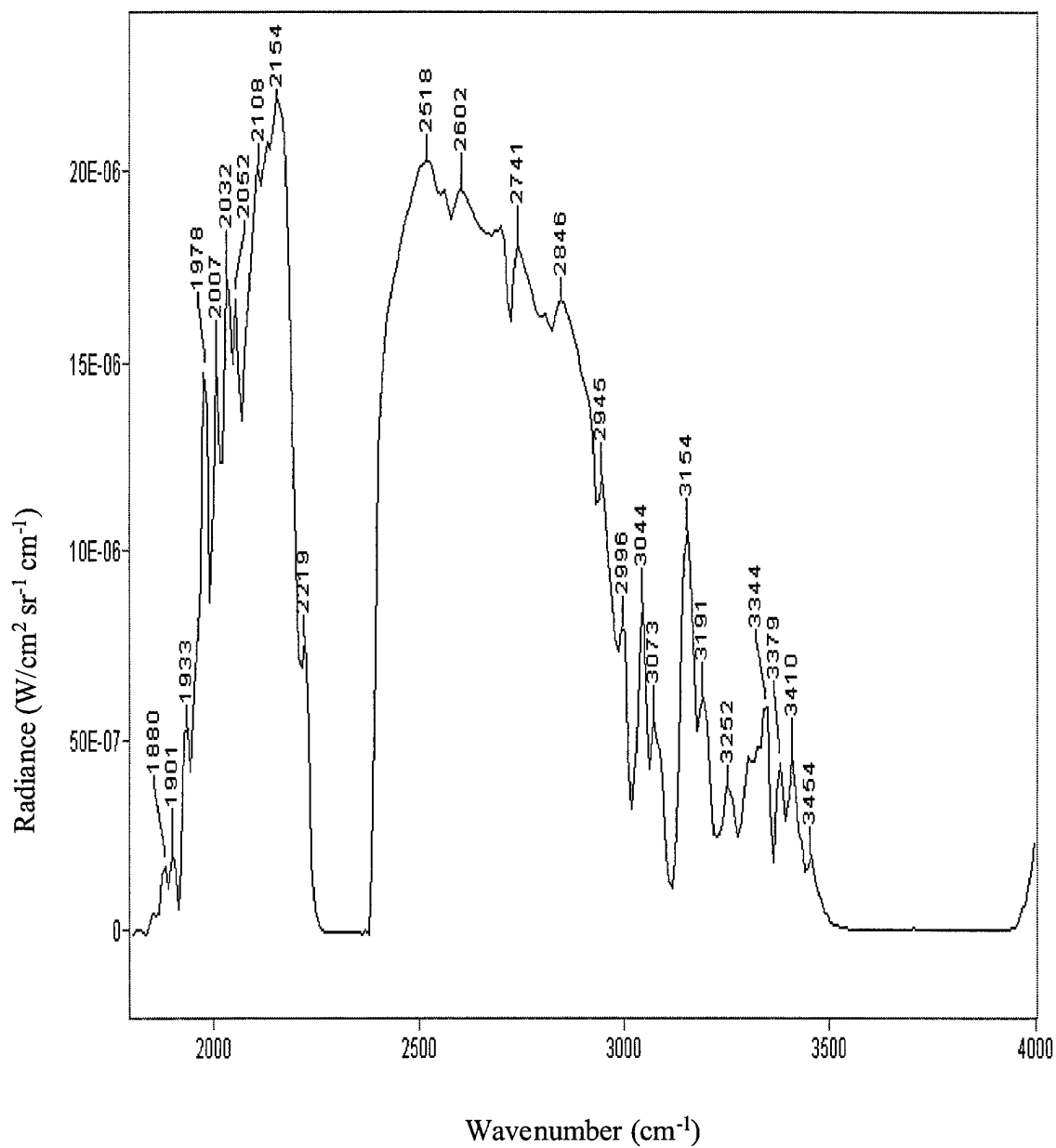


Figure A3.10a. Initial spectral signature retrieved of event 49, TLAM (WDU-36) missile explosion.

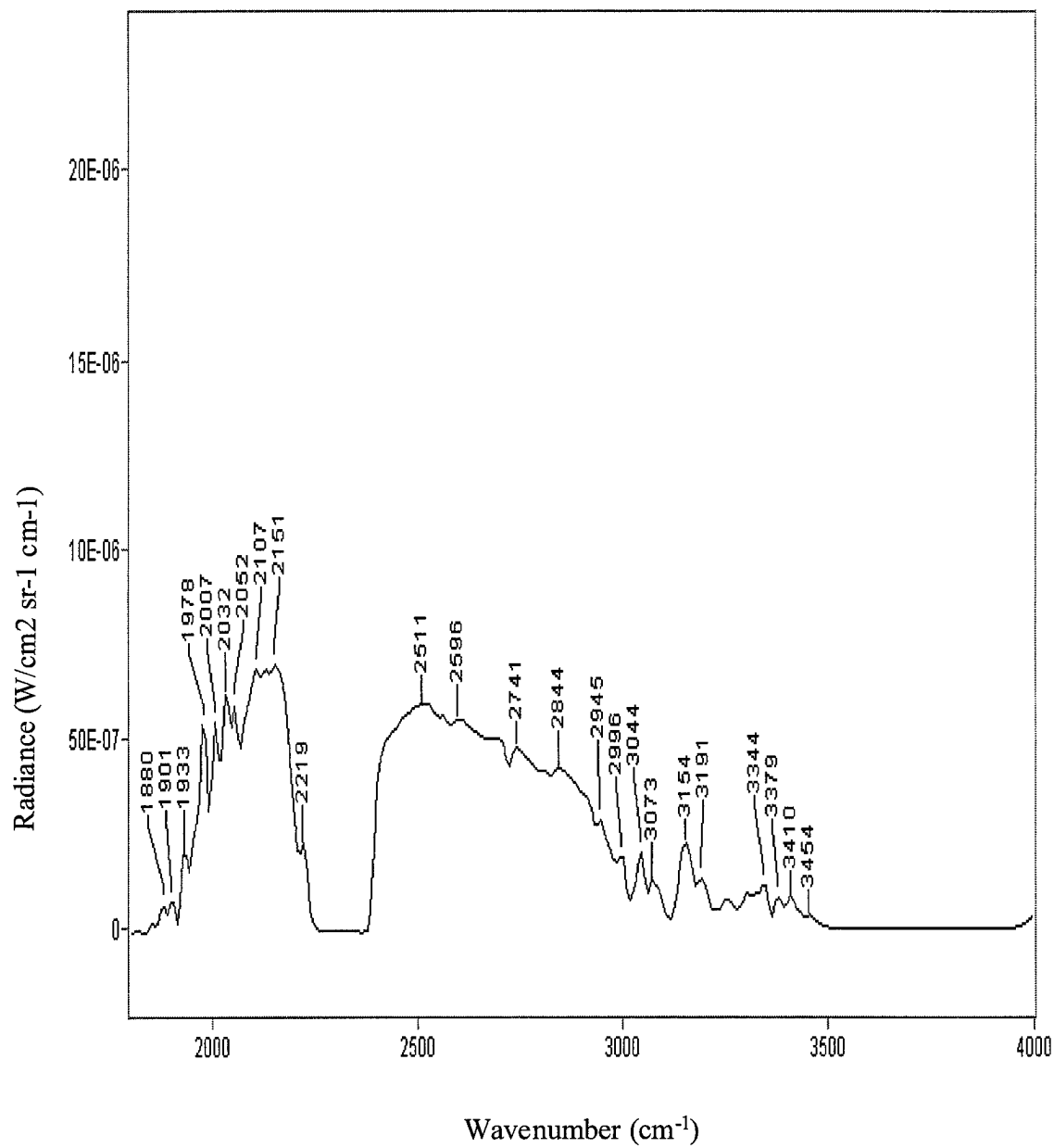


Figure A3.10b. Spectral signature of event 49, TLAM (WDU-36) missile explosion 0.269 seconds after Figure A3.10a.

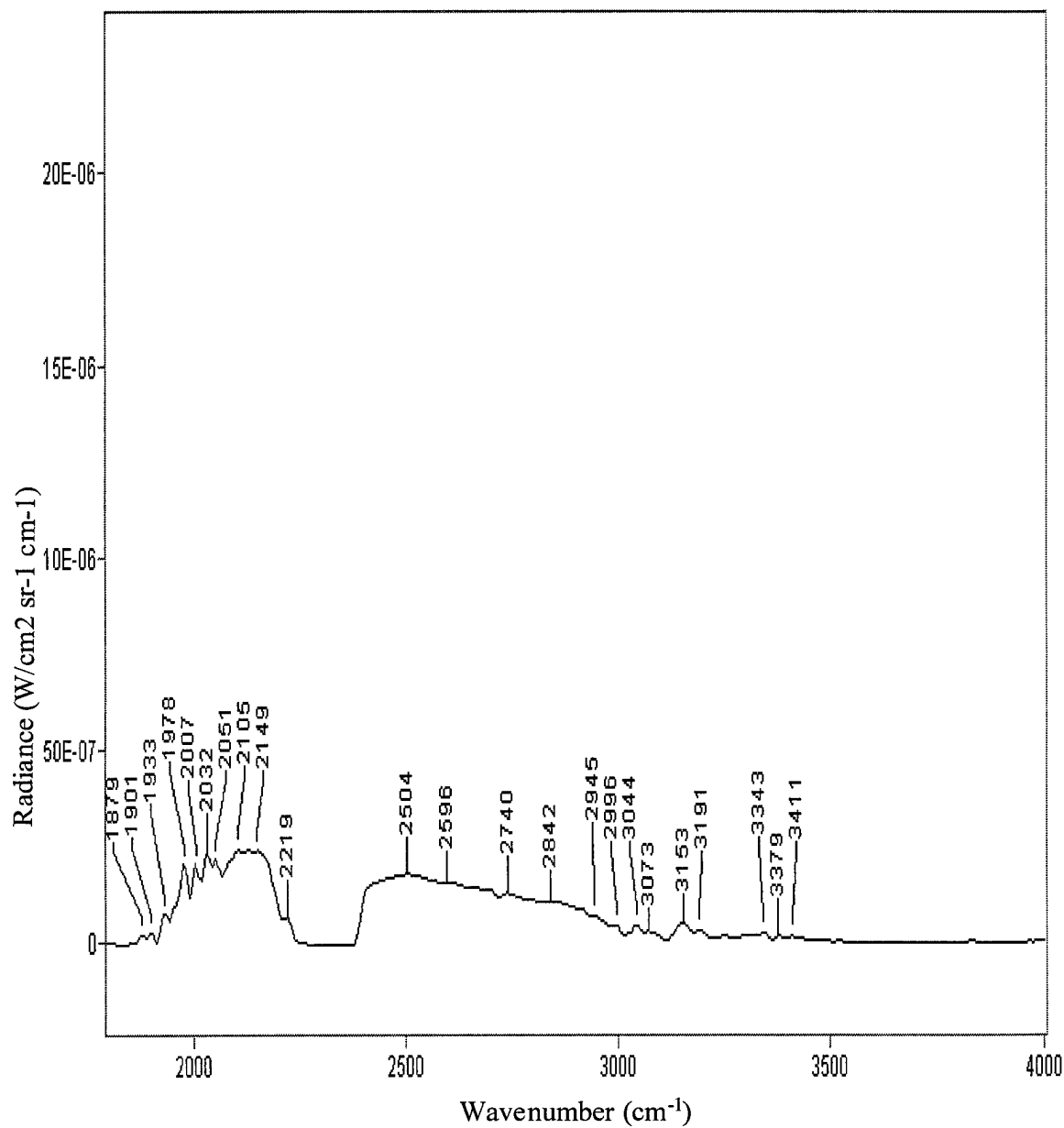


Figure A3.10c. Spectral signature of event 49, TLAM (WDU-36) missile explosion 0.538 seconds after Figure A3.10a.

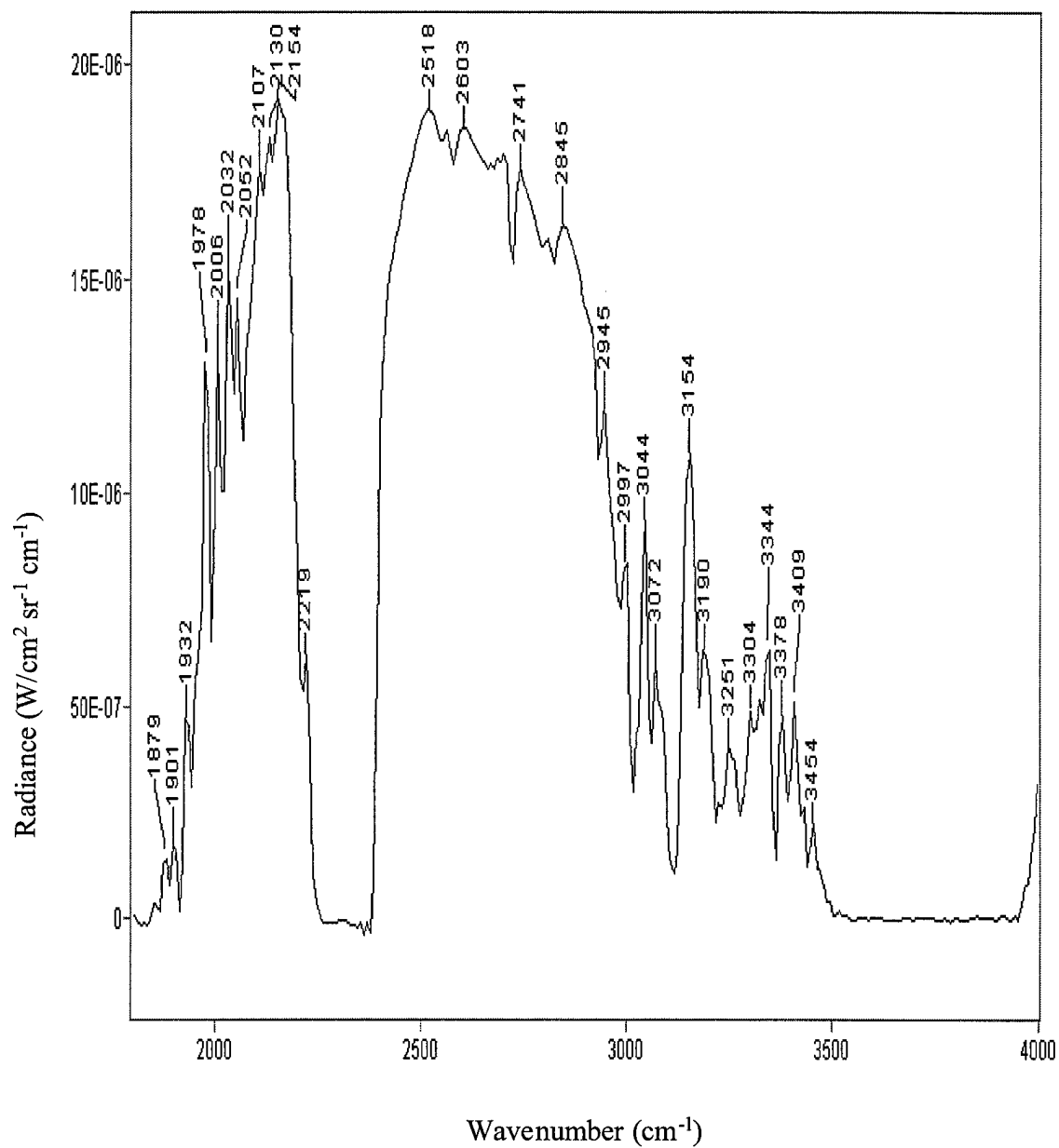


Figure A3.11. Spectral signature of peak radiance observed for event 53, TLAM (WDU-36) missile explosion.

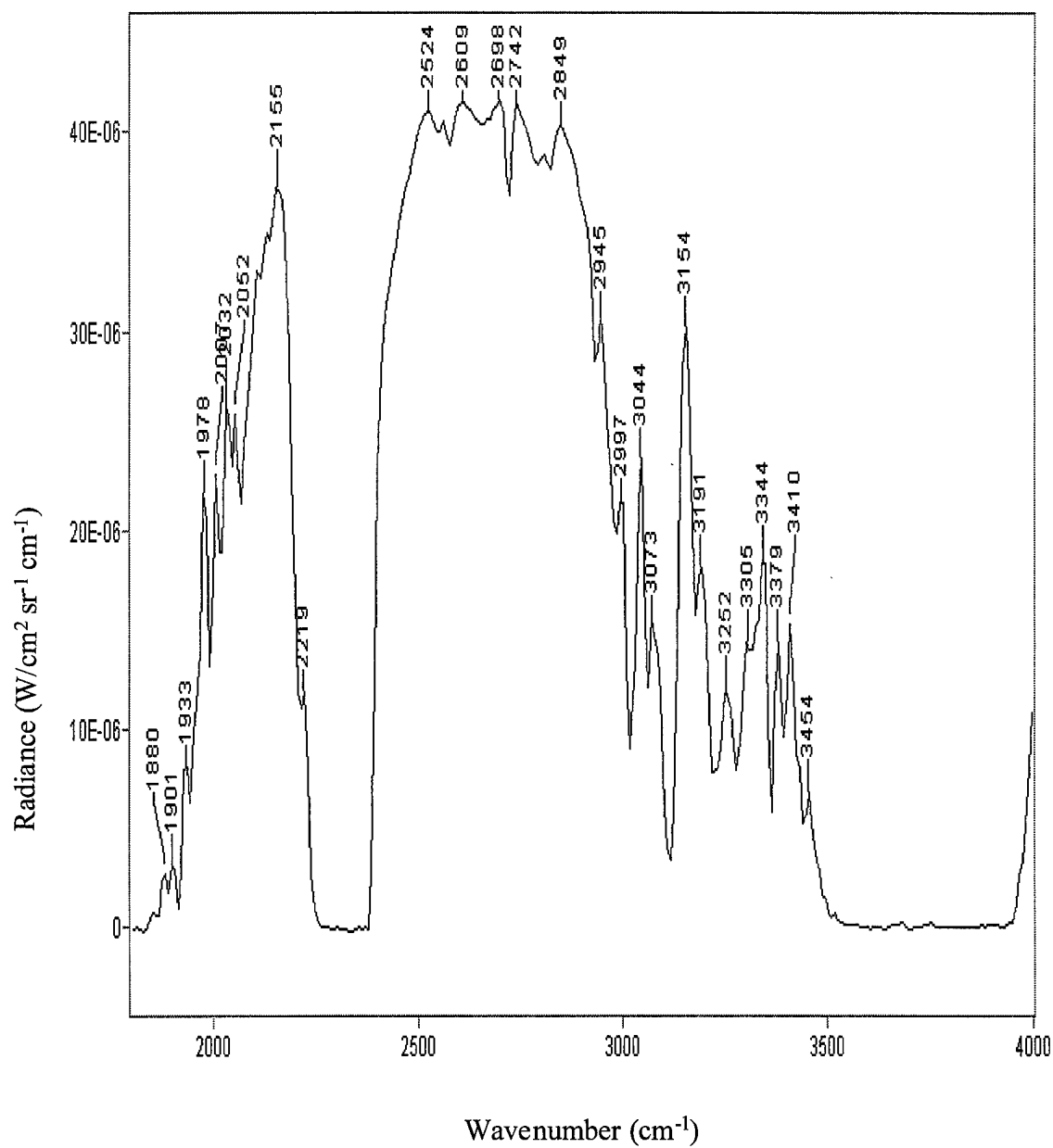


Figure A3.12a. Initial spectral signature retrieved of event 54, TLAM (WDU-25) missile explosion.

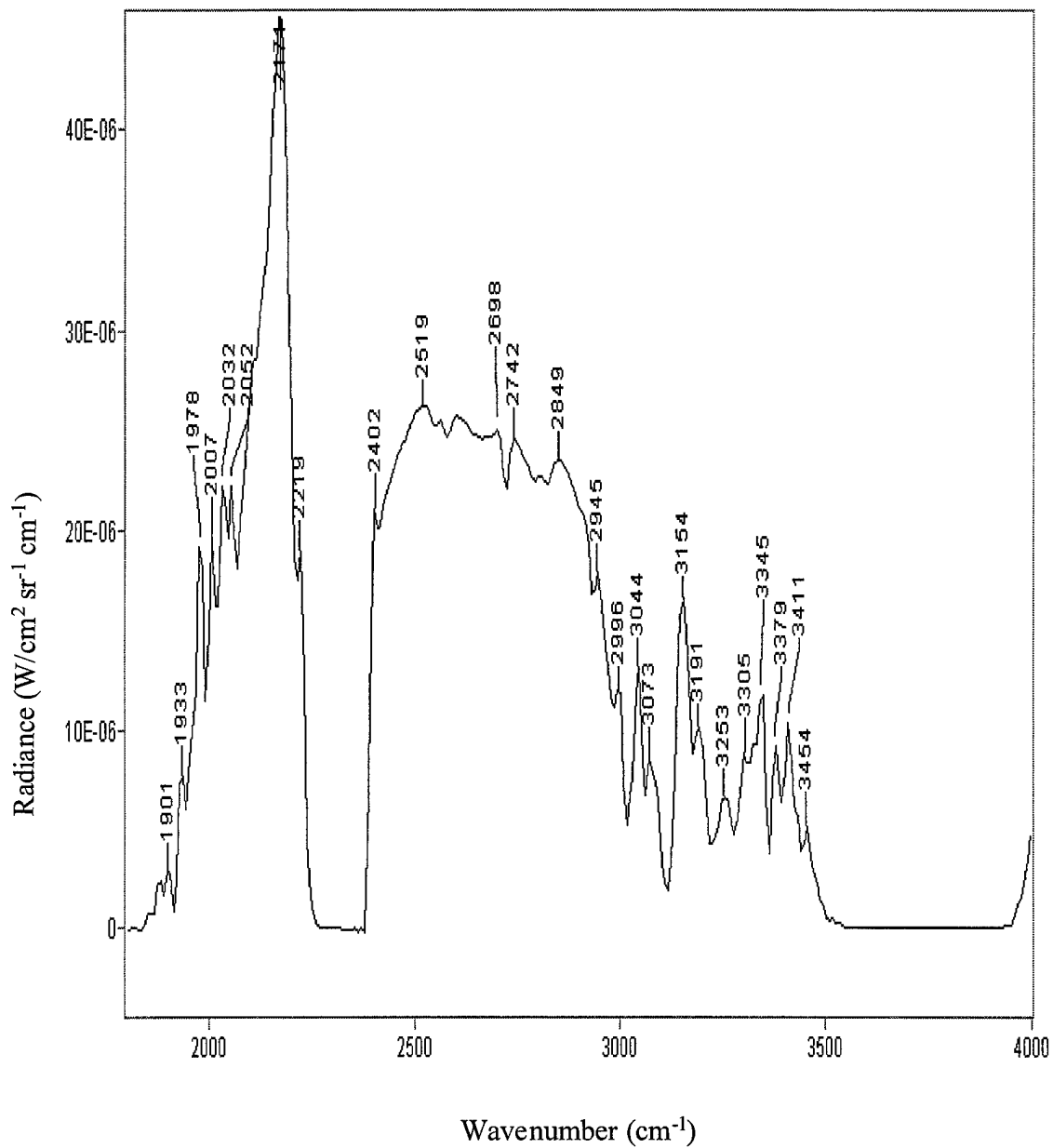


Figure A3.12b. Spectral signature of event 54, TLAM (WDU-25) missile explosion 0.807 seconds after Figure A3.12a.

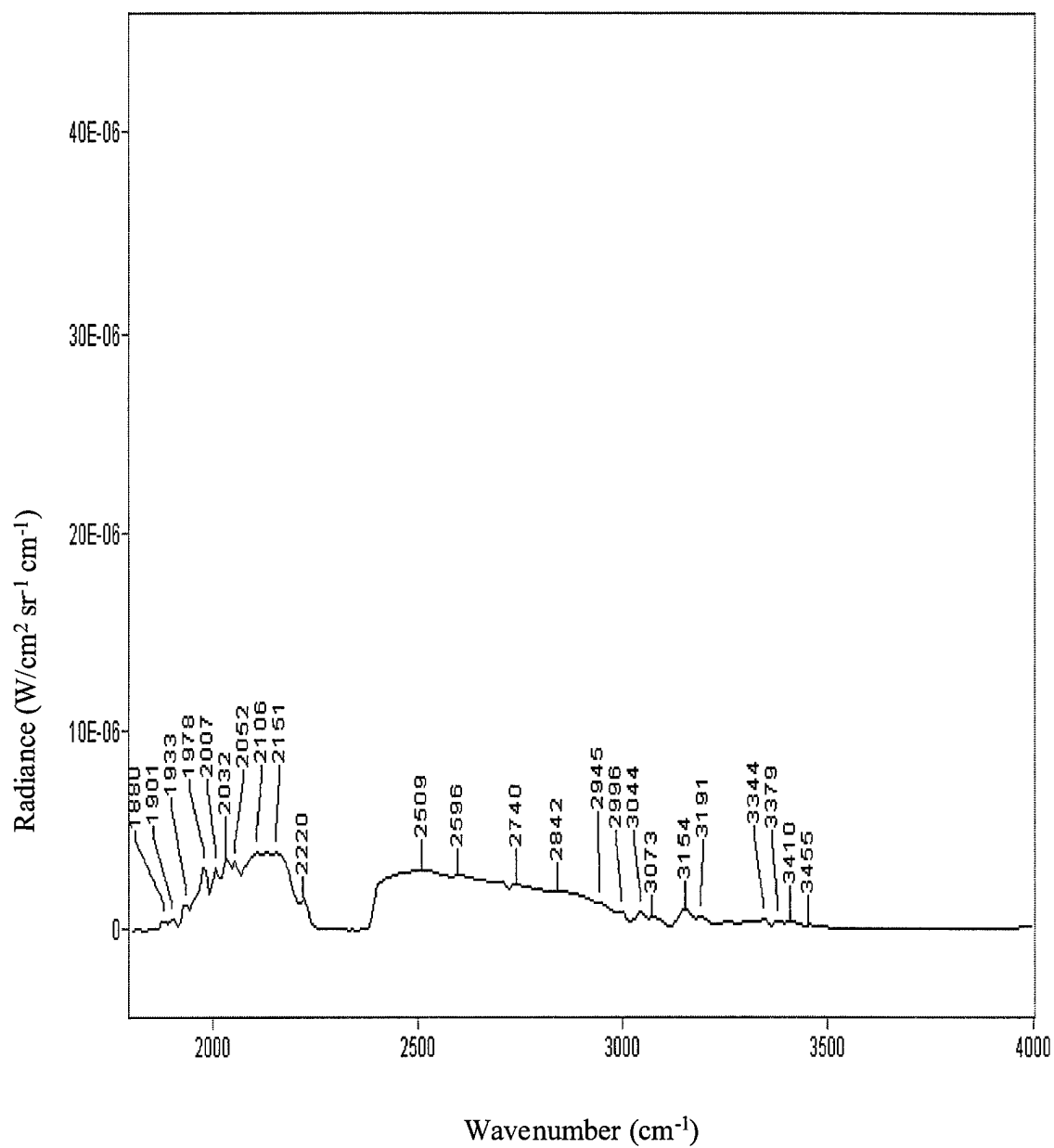


Figure A3.12c. Spectral signature of event 54, TLAM (WDU-25) missile explosion 1.347 seconds after Figure A3.12a.

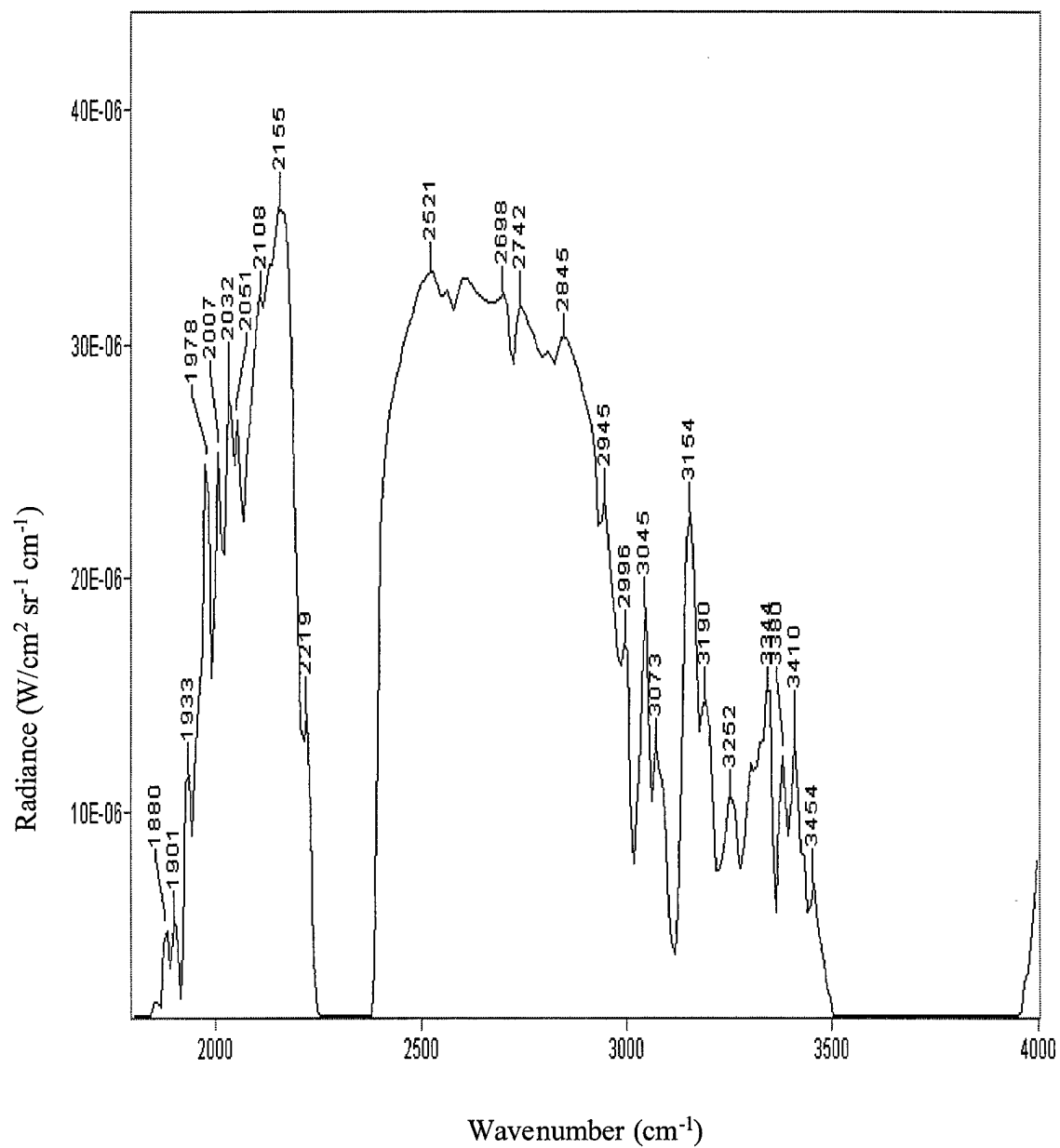


Figure A3.13a. Initial spectral signature retrieved of event 43, TLAM (WDU-25) missile explosion.

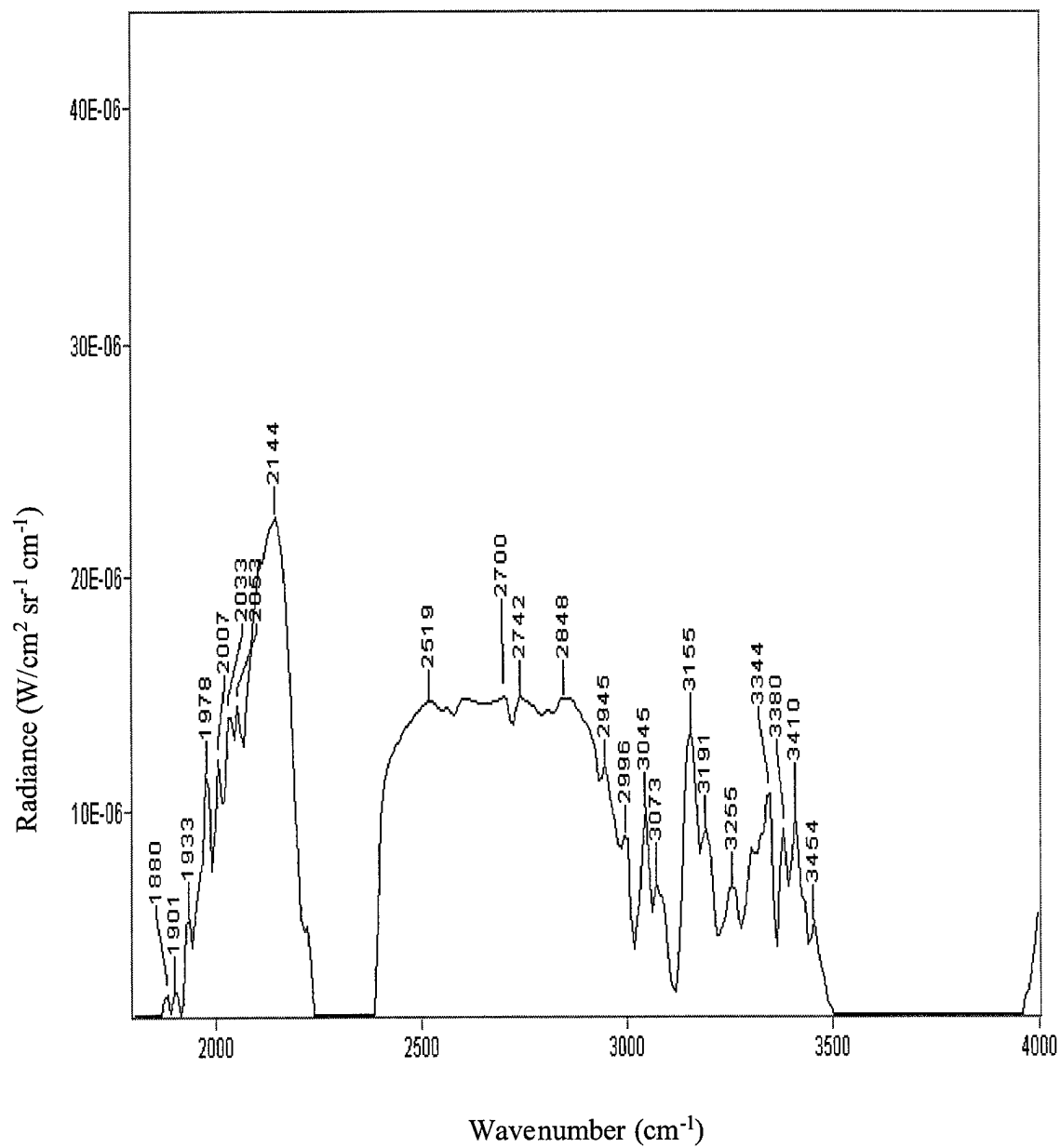


Figure A3.13b. Spectral signature of event 43, TLAM (WDU-25) missile explosion 0.267 seconds after Figure A3.13a.

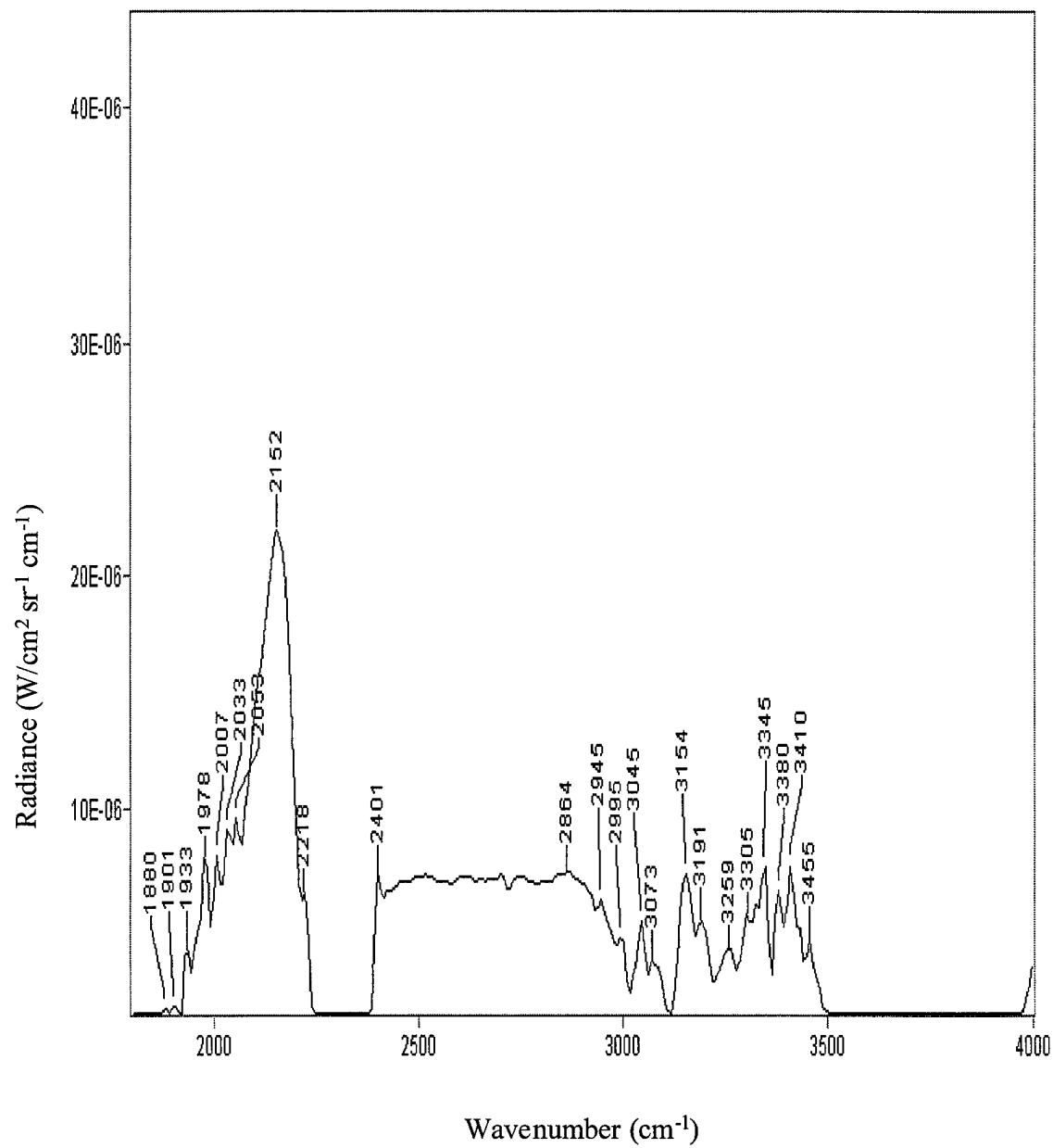


Figure A3.13c. Spectral signature of event 43, TLAM (WDU-25) missile explosion 0.536 seconds after Figure A3.13a.

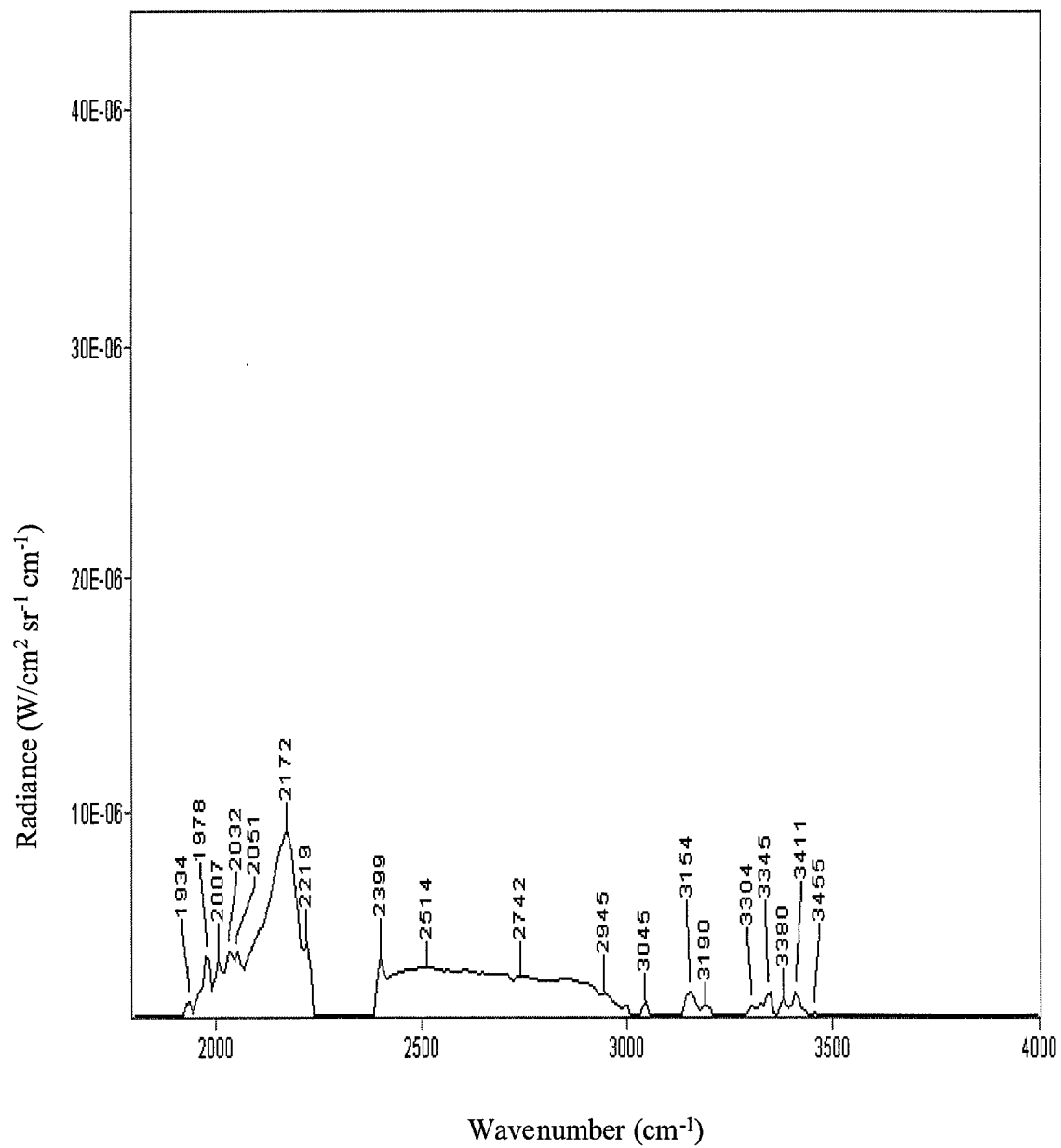


Figure A3.13d. Spectral signature of event 43, TLAM (WDU-25) missile explosion 0.804 seconds after Figure A3.13a

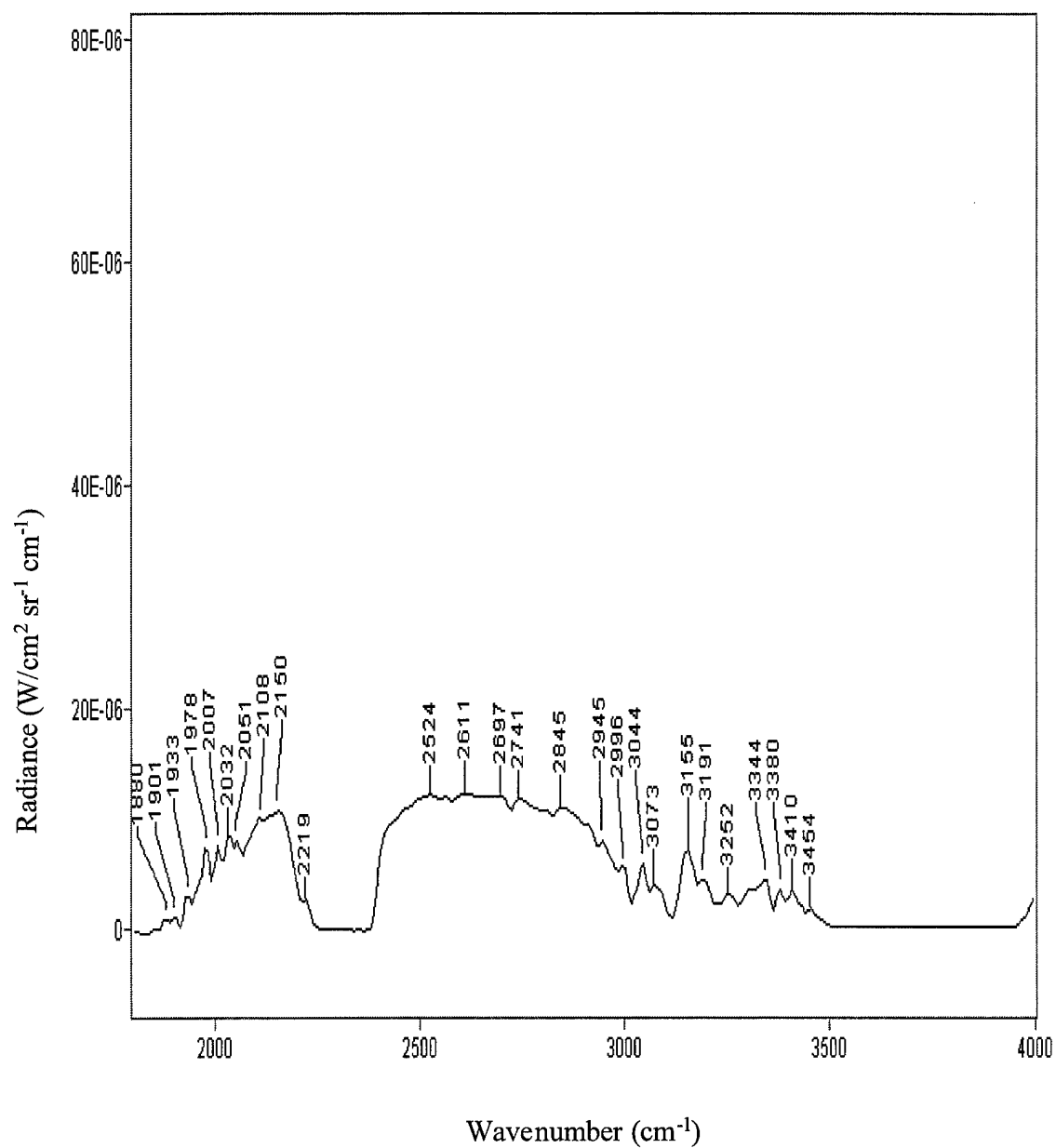


Figure A3.14a. Initial spectral signature retrieved of event 47, Mk 84 bomb explosion.

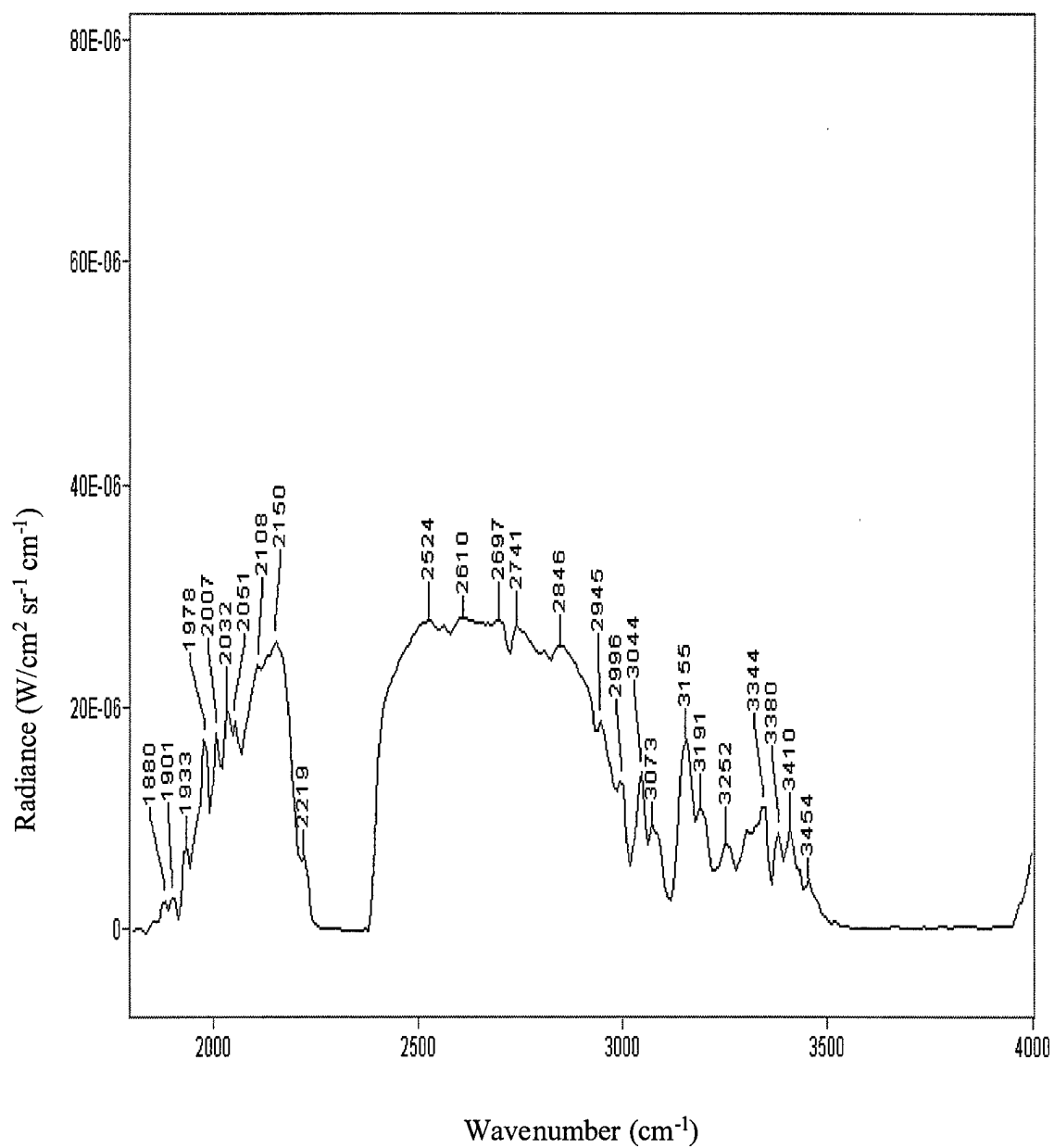


Figure A3.14b. Spectral signature of event 47, Mk 84 bomb explosion 0.267 seconds after Figure A3.14a.

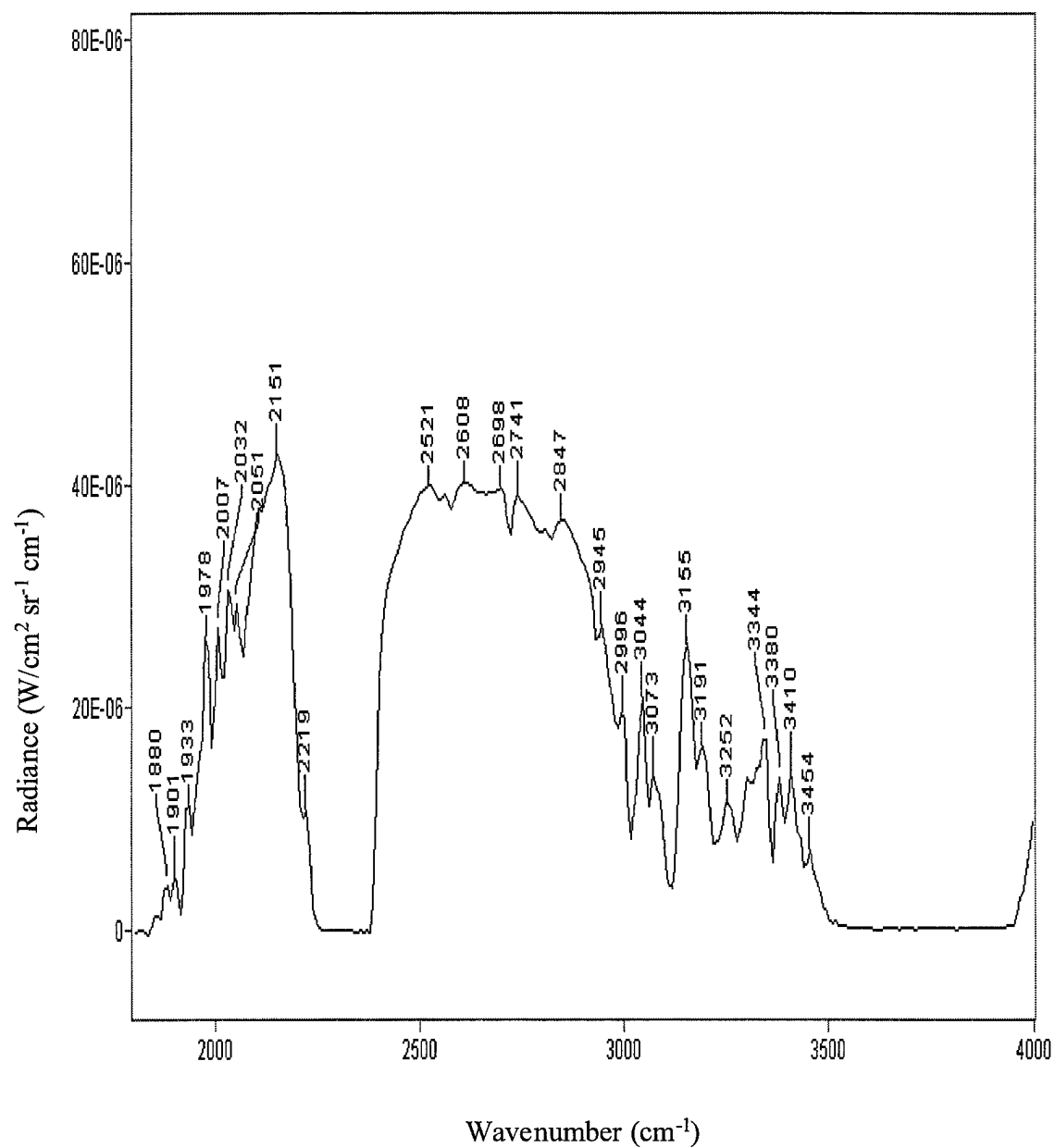


Figure A3.14c. Spectral signature of event 47, Mk 84 bomb explosion 0.536 seconds after Figure A3.14a.

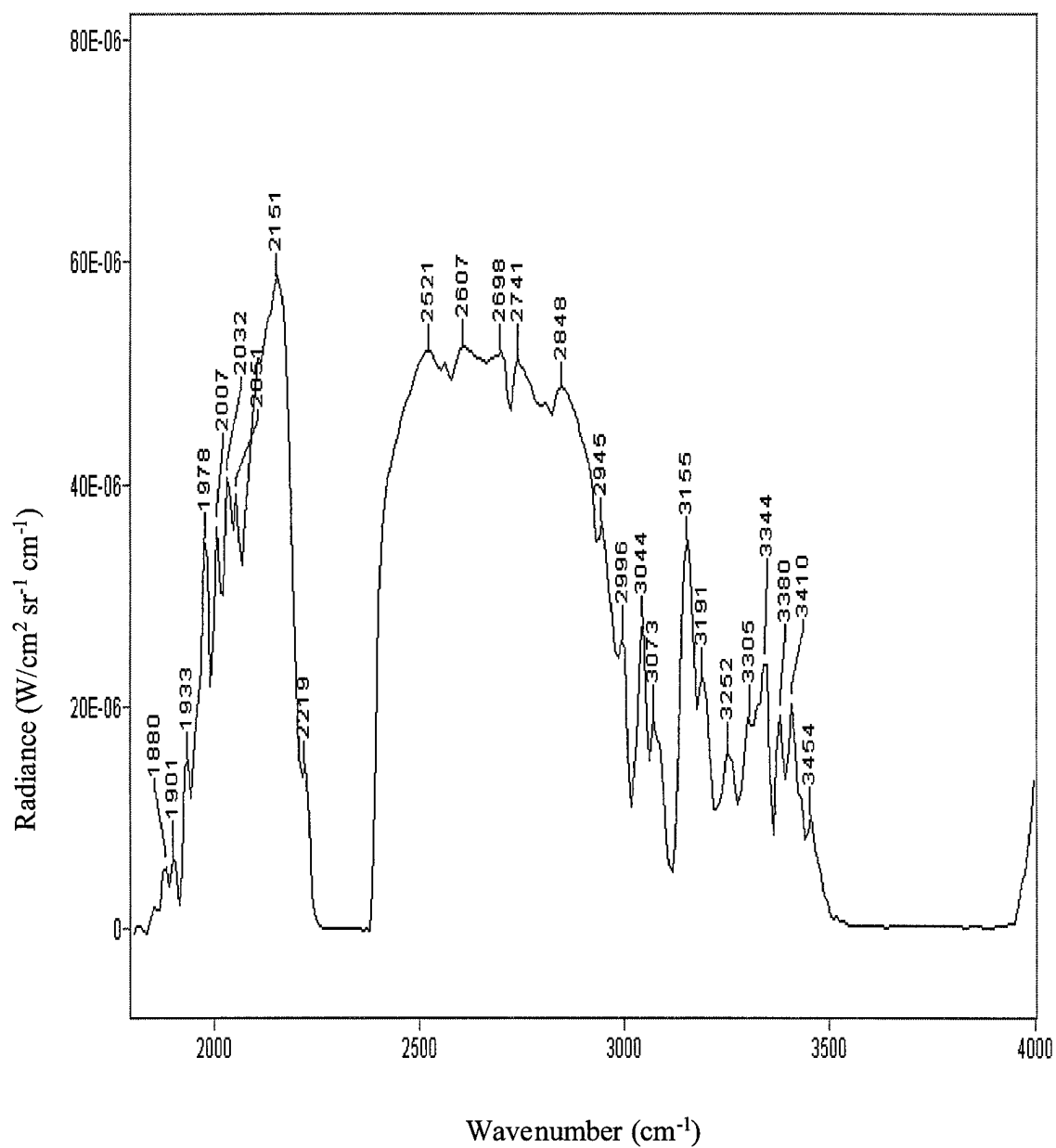


Figure A3.14d. Spectral signature of event 47, Mk 84 bomb explosion 0..803 seconds after Figure A3.14a.

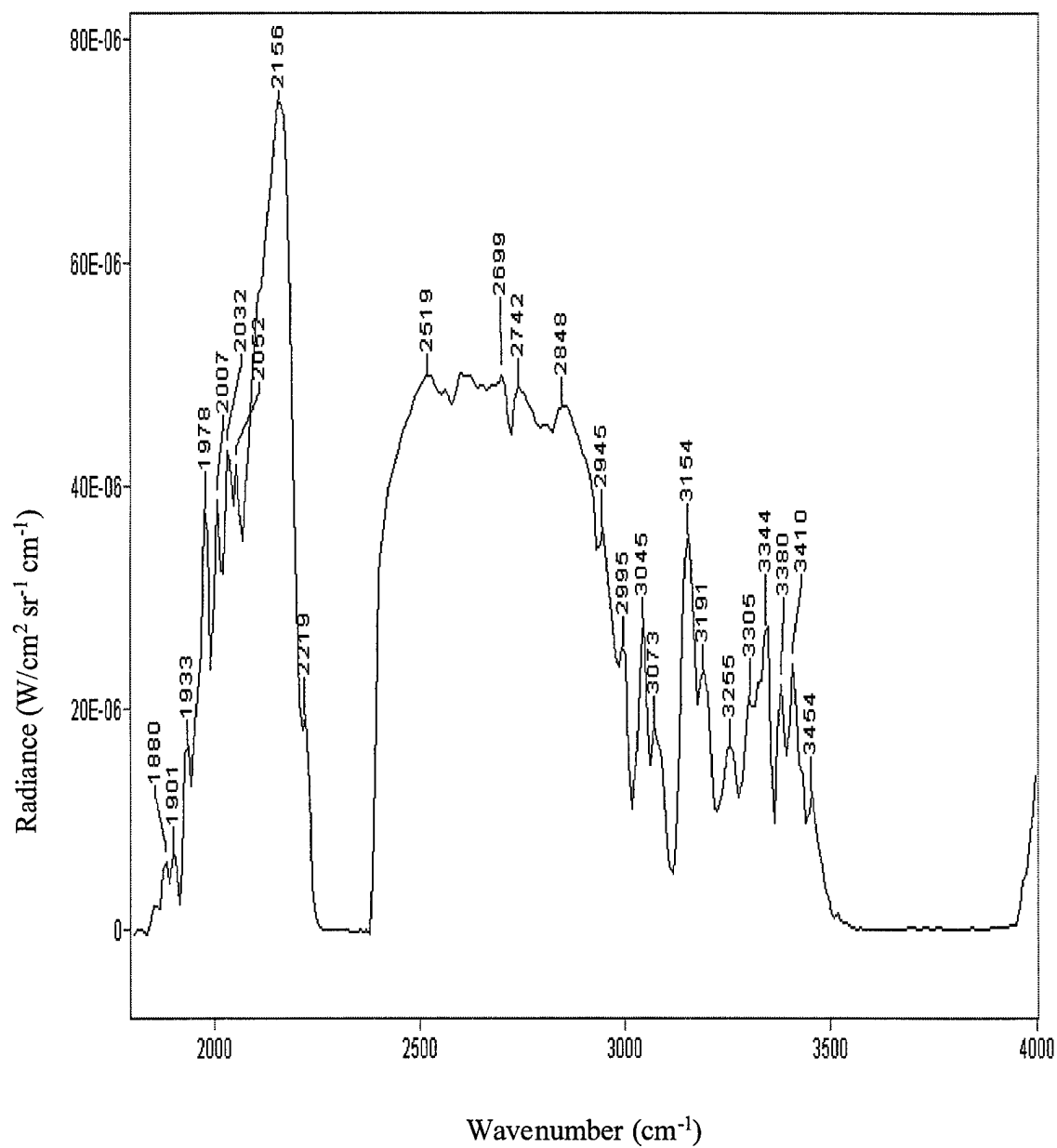


Figure A3.14e. Spectral signature of event 47, Mk 84 bomb explosion 1.071 seconds after Figure A3.14a.

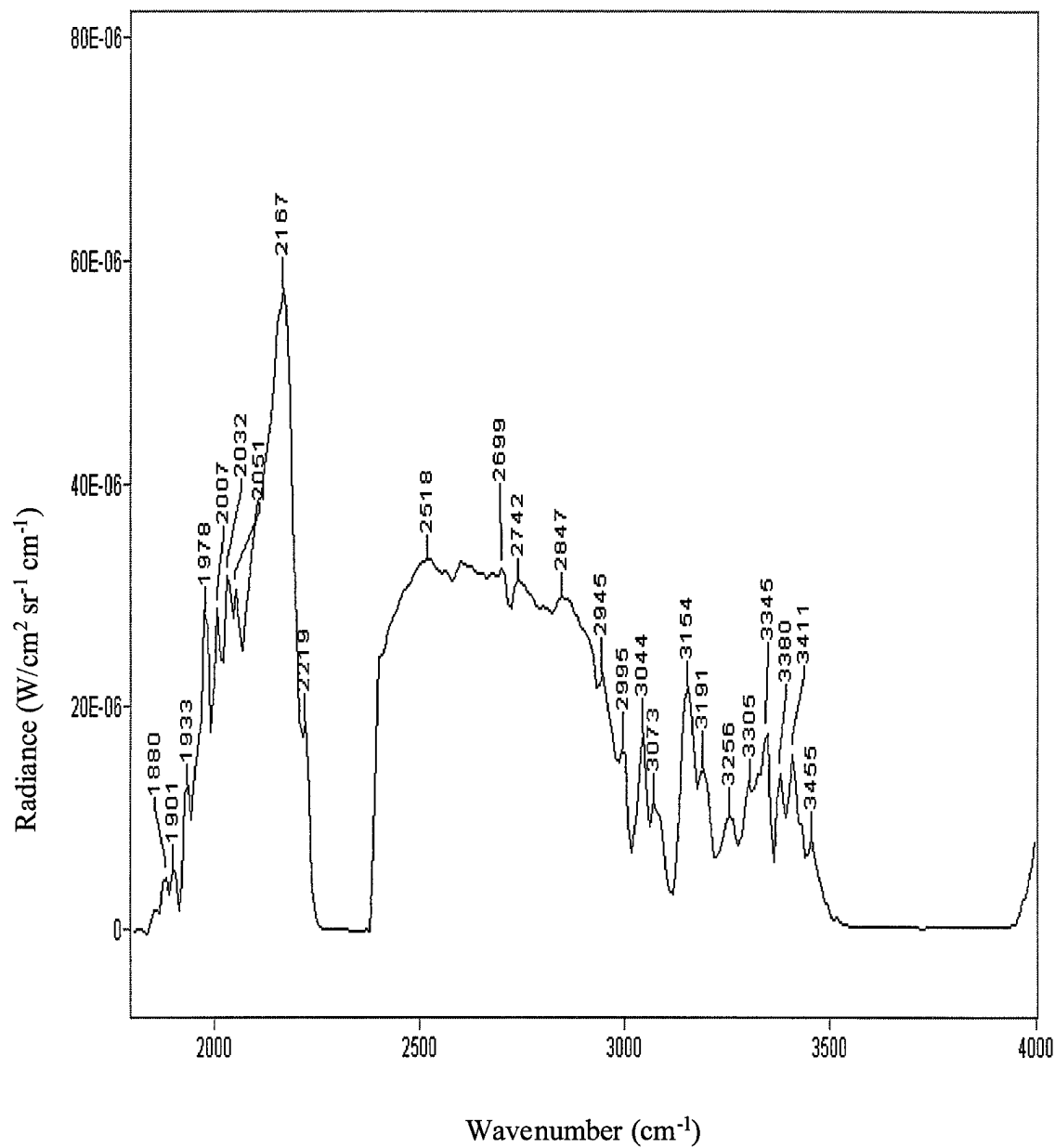


Figure A3.14f. Spectral signature of event 47, Mk 84 bomb explosion 1.339 seconds after Figure A3.14a.

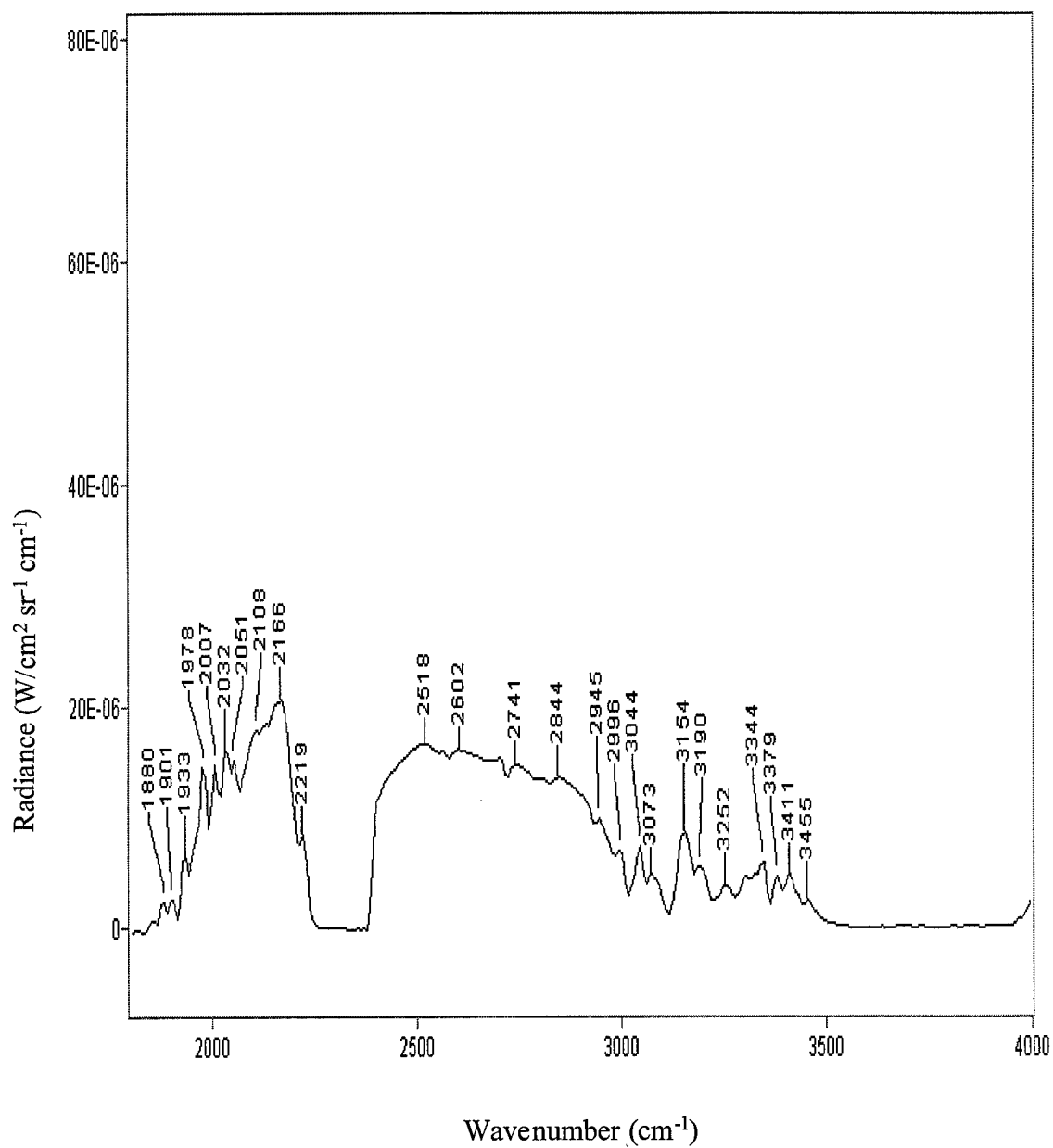


Figure A3.14g. Spectral signature of event 47, Mk 84 bomb explosion 1.606 seconds after Figure A3.14a.

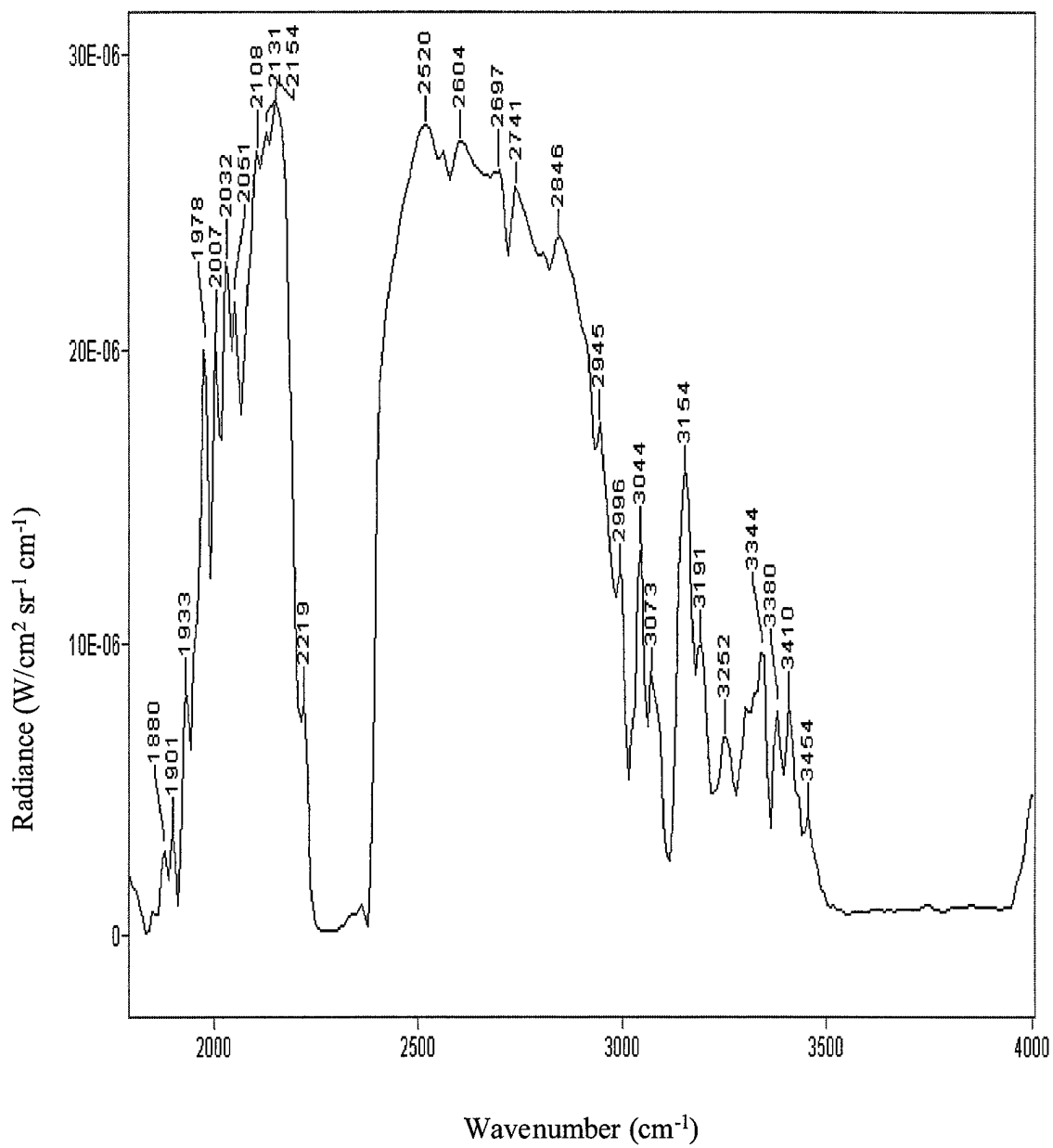


Figure A3.15a. Initial spectral signature retrieved of event 45, Mk 84 bomb explosion.

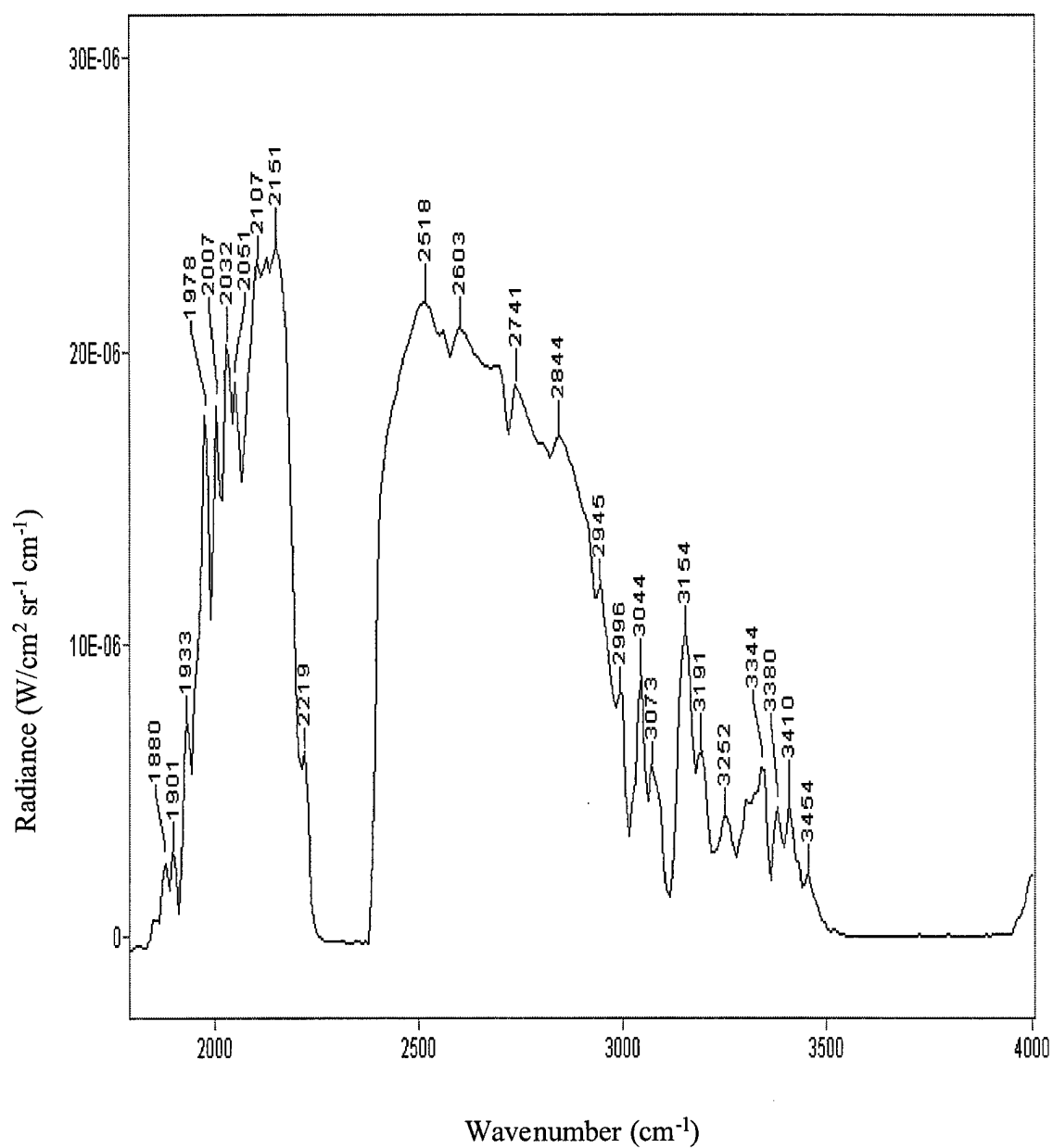


Figure A3.15b. Spectral signature of event 47, Mk 84 bomb explosion 0.269 seconds after Figure A3.15a.

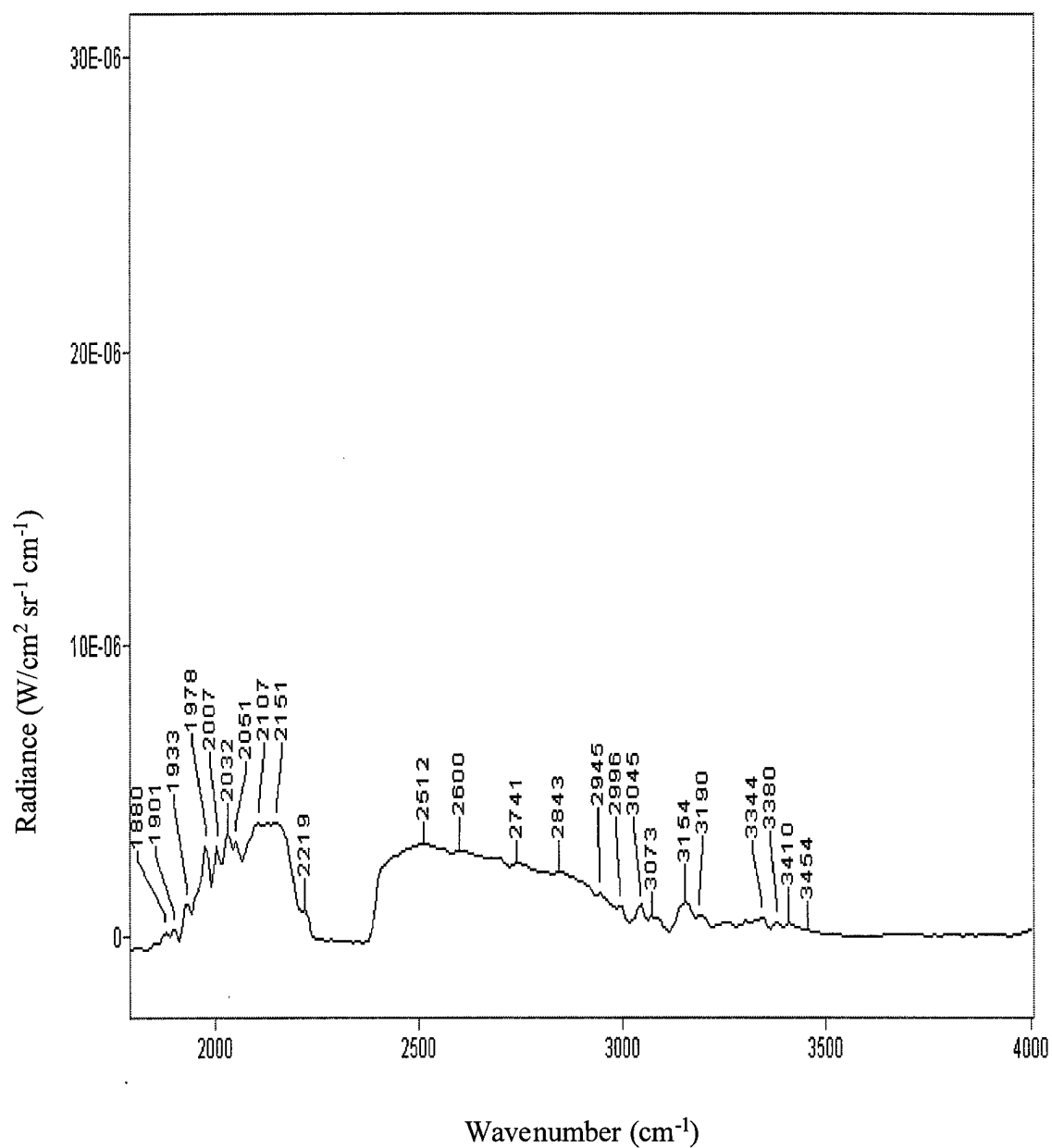


Figure A3.15c. Spectral signature of event 47, Mk 84 bomb explosion 0.537 seconds after Figure A3.15a.

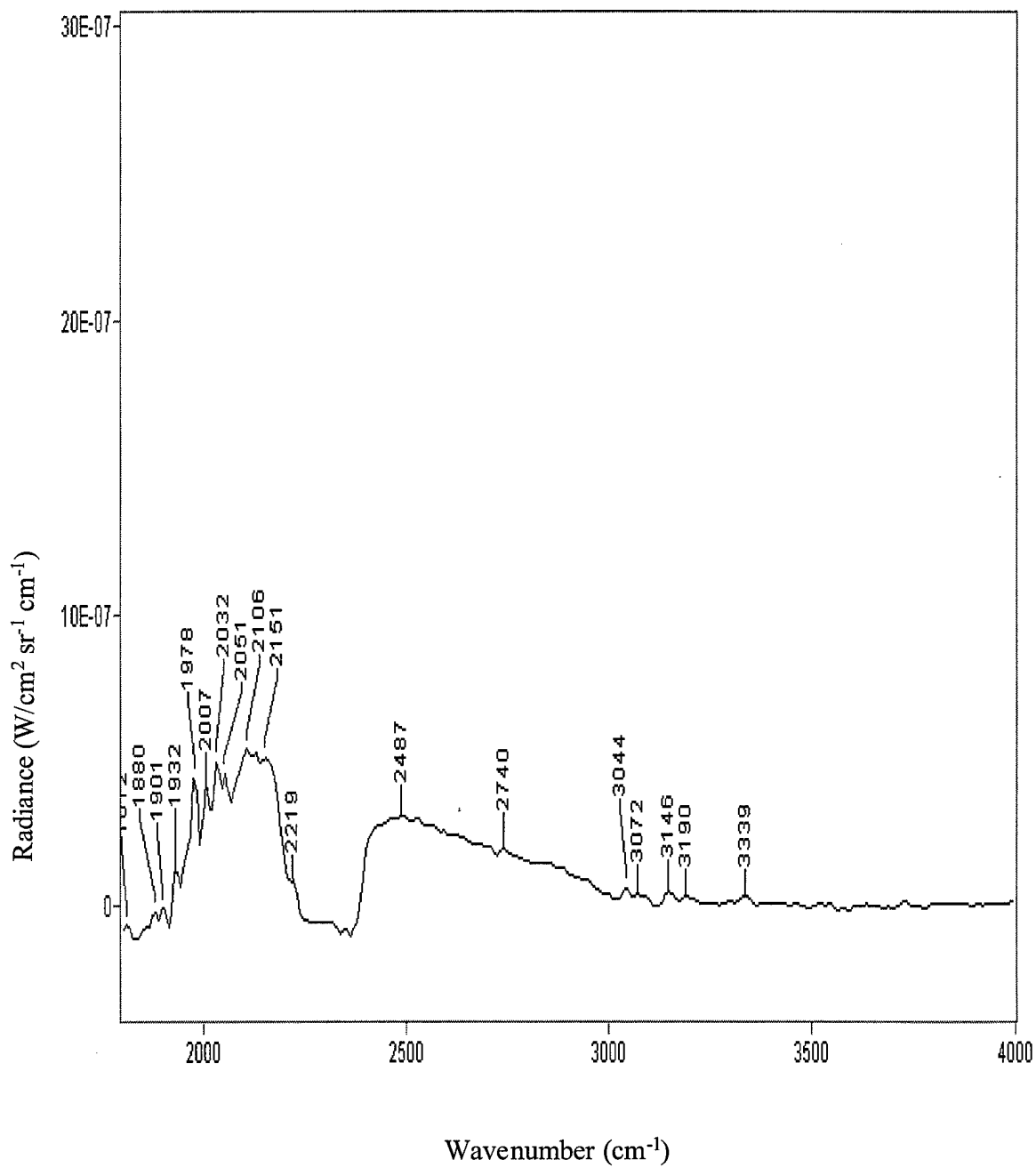


Figure A3.16a. Initial spectral signature retrieved of event 52, Mk 83 bomb explosion.

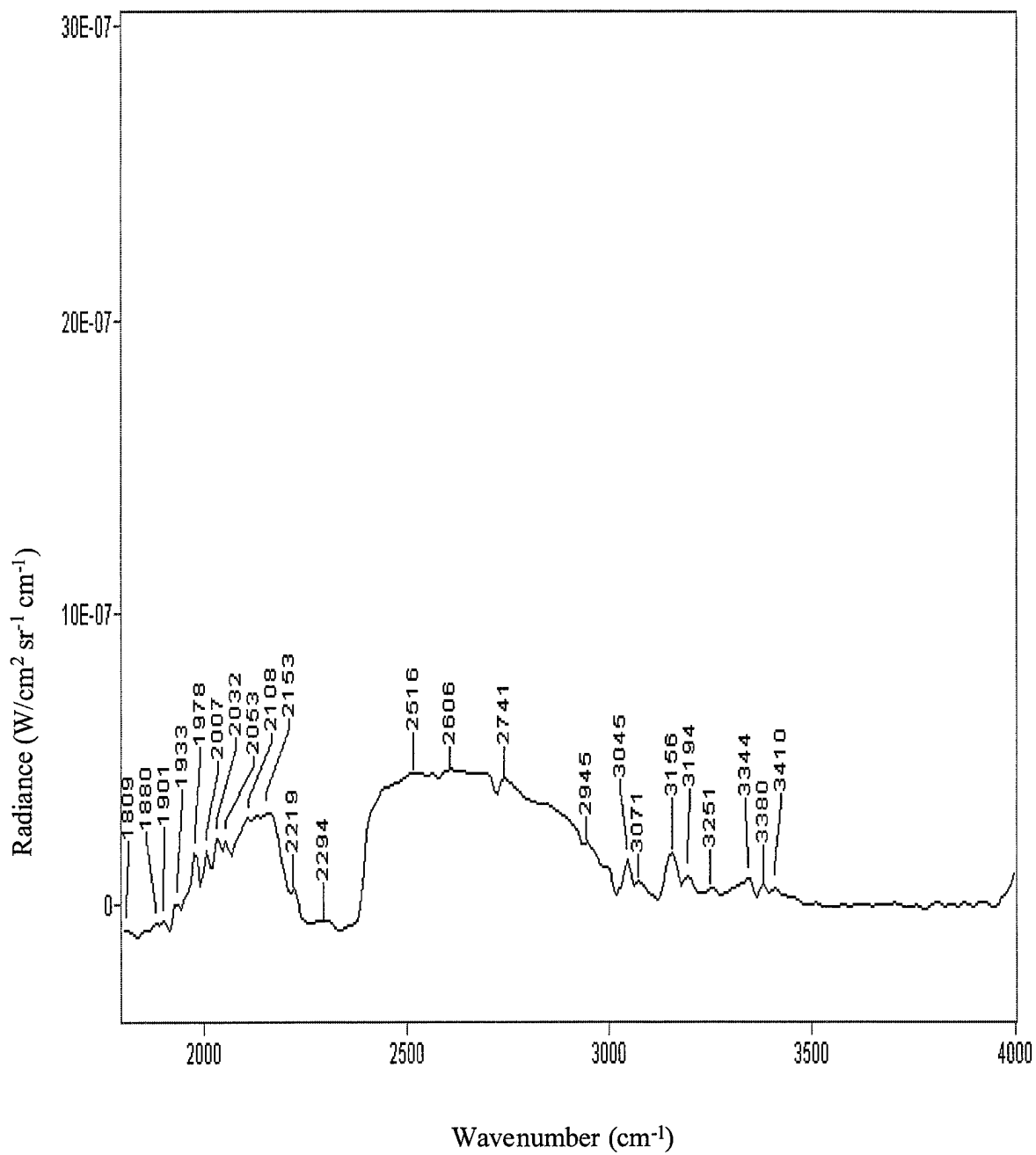


Figure A3.16b. Spectral signature of event 52, Mk 83 bomb explosion 0.271 seconds after Figure A3.16a.

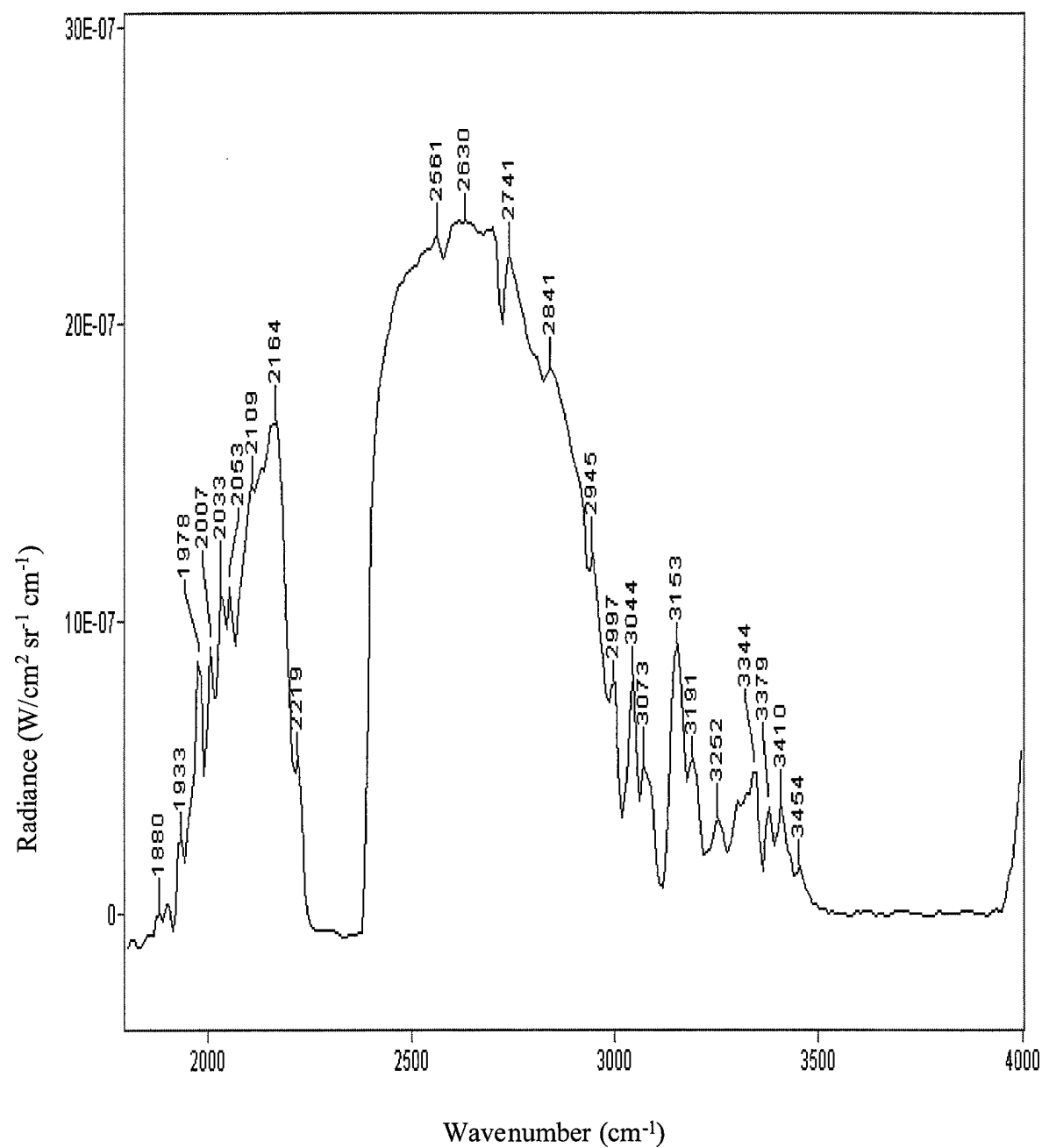


Figure A3.16c. Spectral signature of event 47, Mk 83 bomb explosion 0.540 seconds after Figure A3.16a.

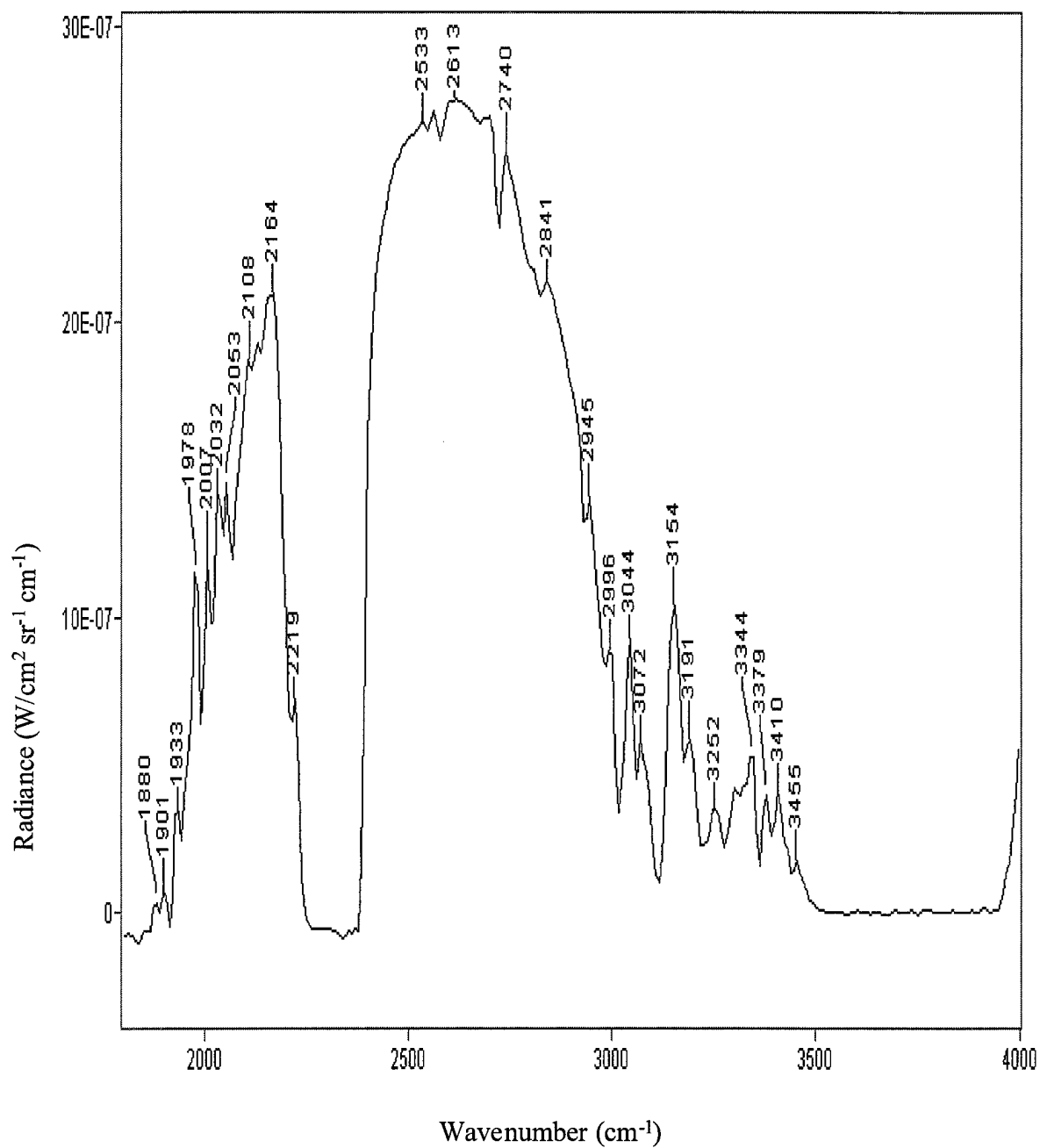


Figure A3.16d. Spectral signature of event 47, Mk 83 bomb explosion 0.810 seconds after Figure A3.16a.

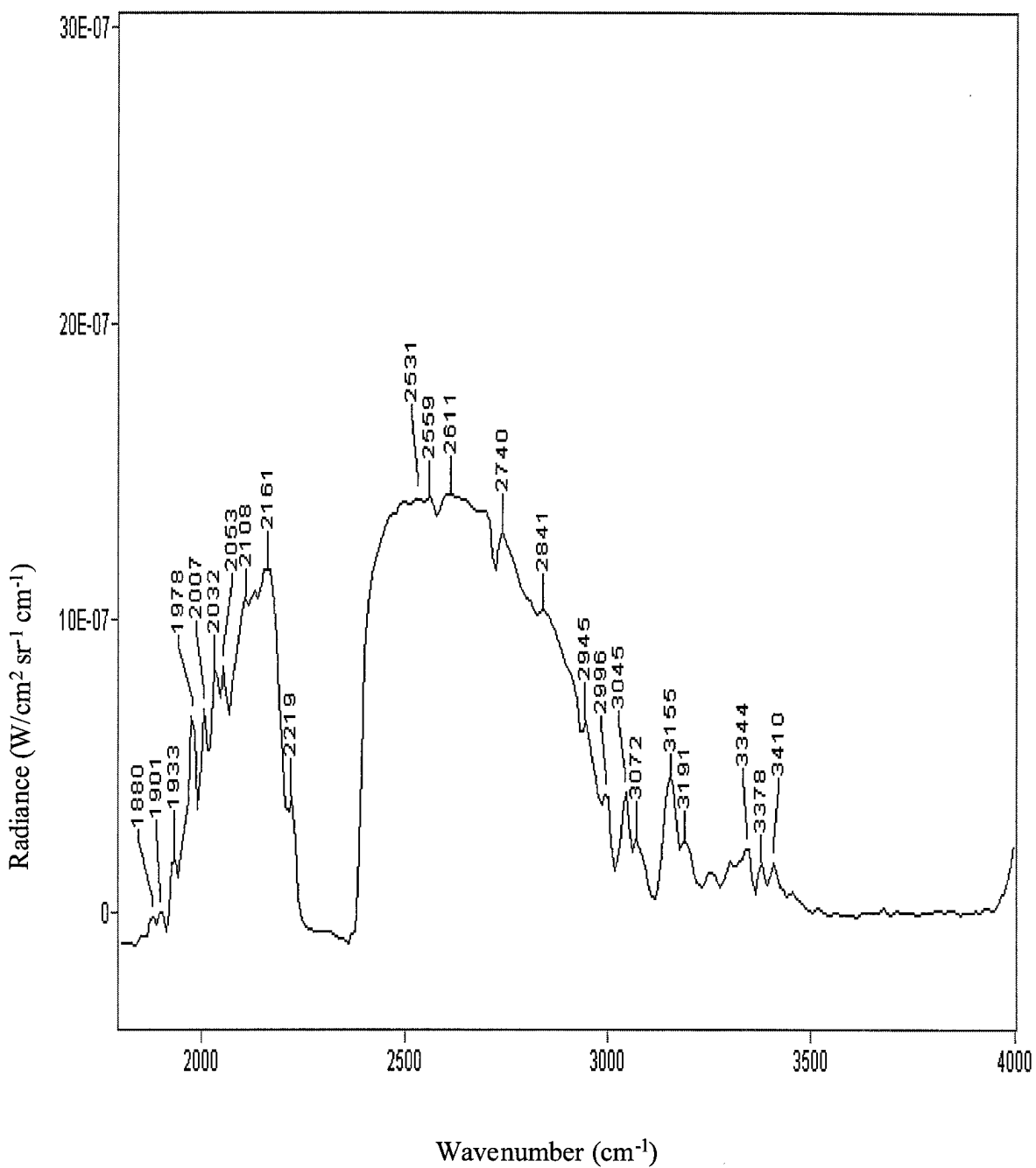


Figure A3.16e. Spectral signature of event 47, Mk 83 bomb explosion 1.080 seconds after Figure A3.16a.

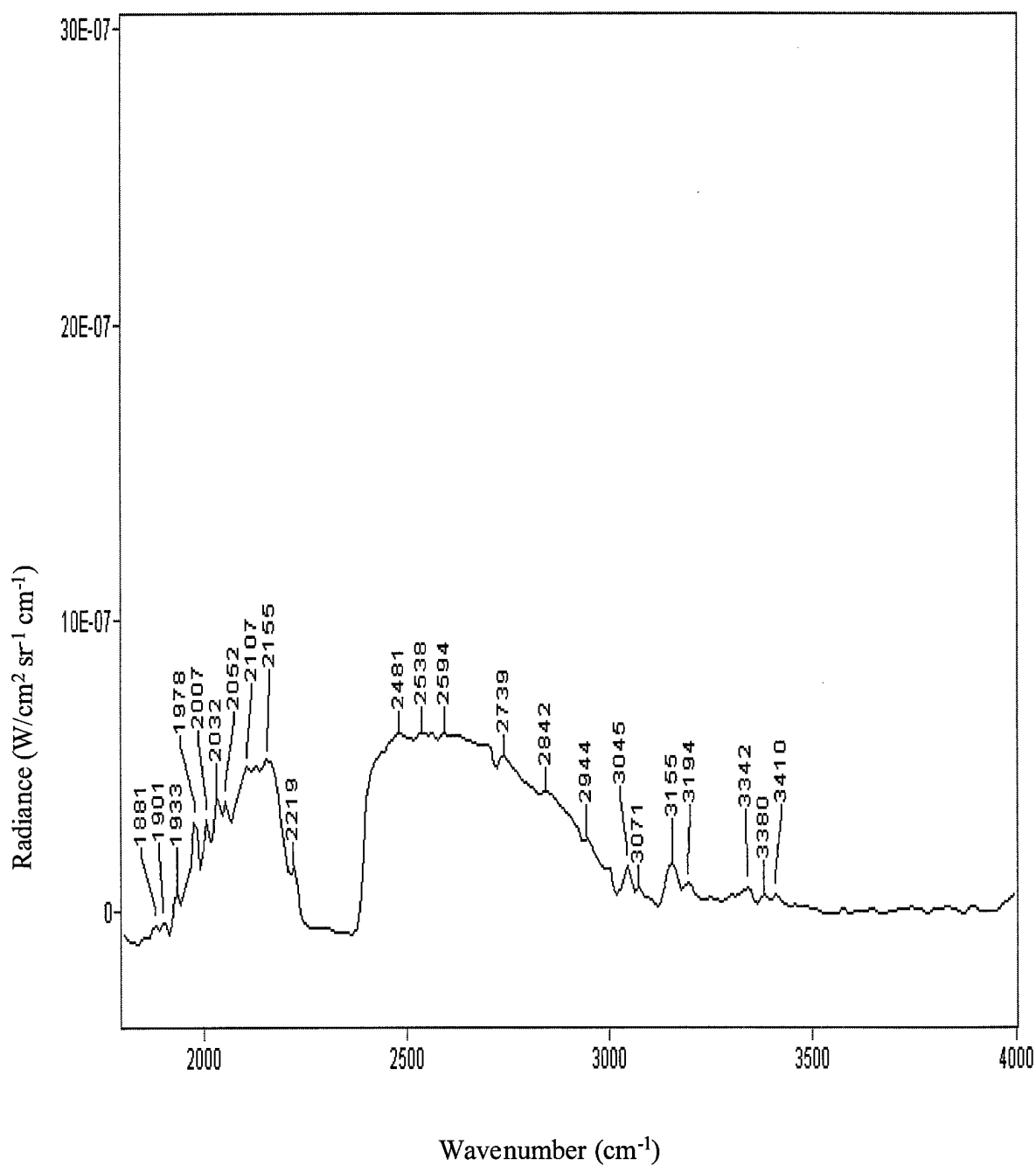


Figure A3.16f. Spectral signature of event 47, Mk 83 bomb explosion 1.351 seconds after Figure A3.16a.

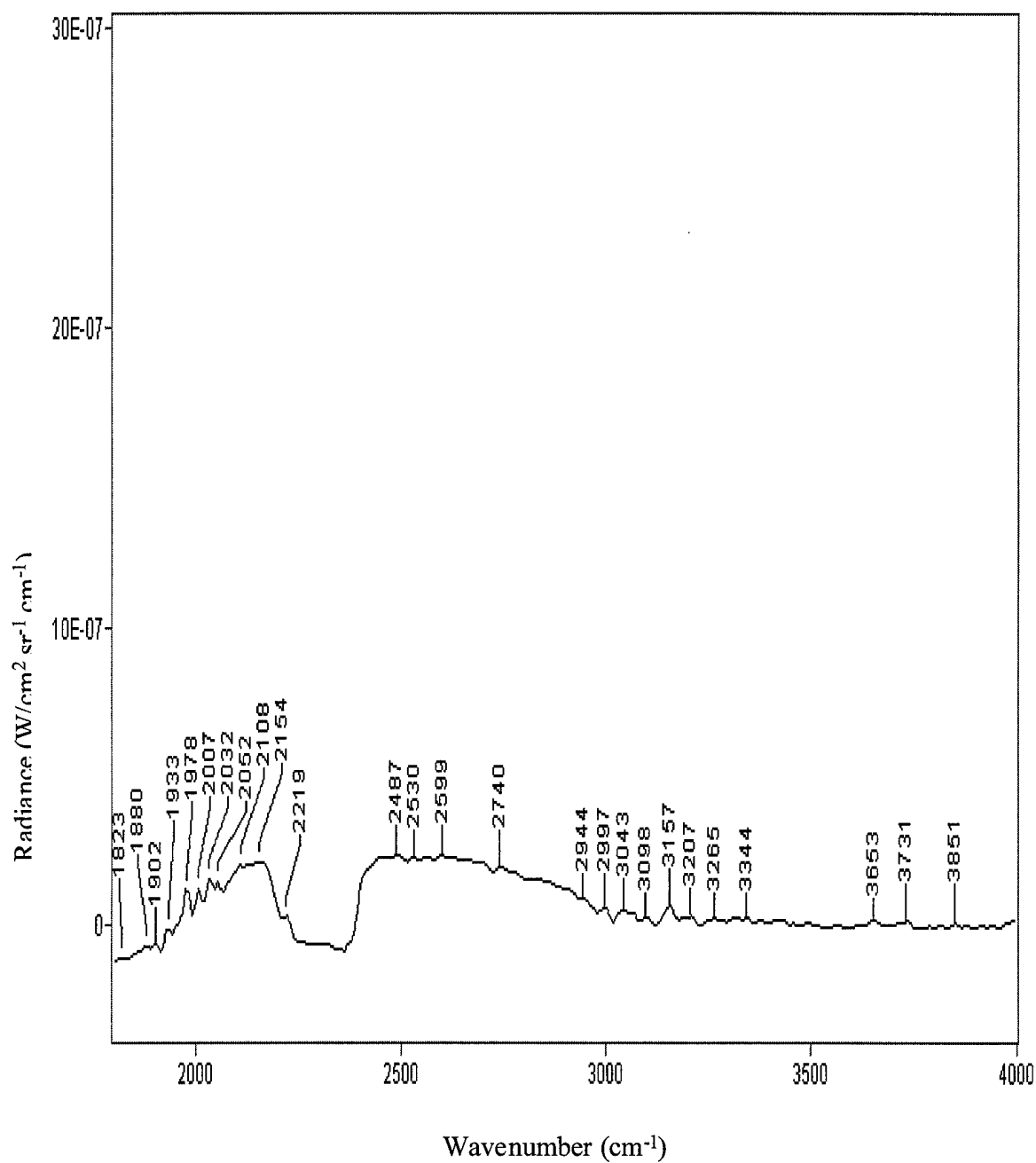


Figure A3.16g. Spectral signature of event 47, Mk 83 bomb explosion 1.621 seconds after Figure A3.16a.

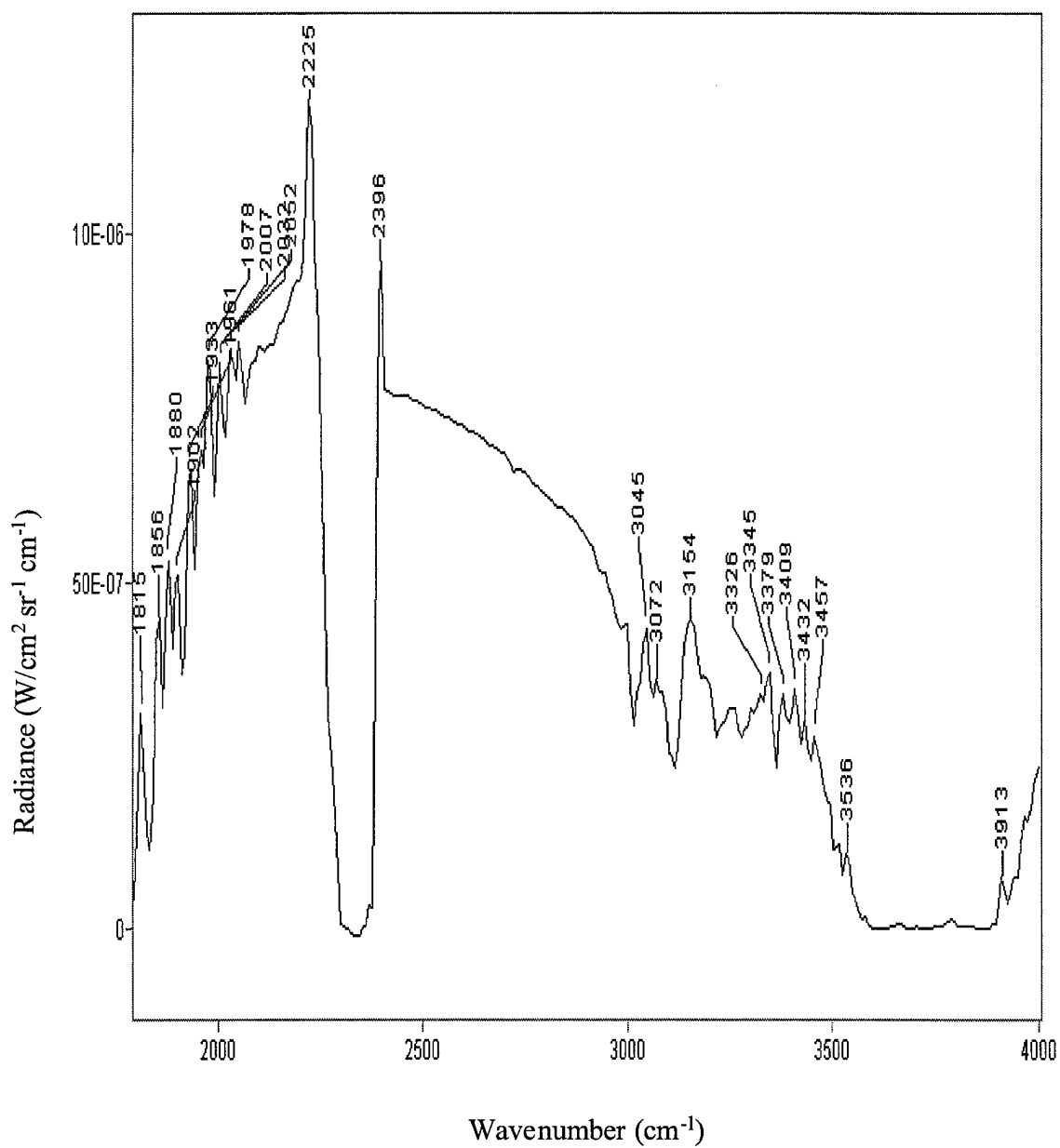


Figure A3.17a. Initial spectral signature retrieved of event A, C-4 plastic explosive detonation.

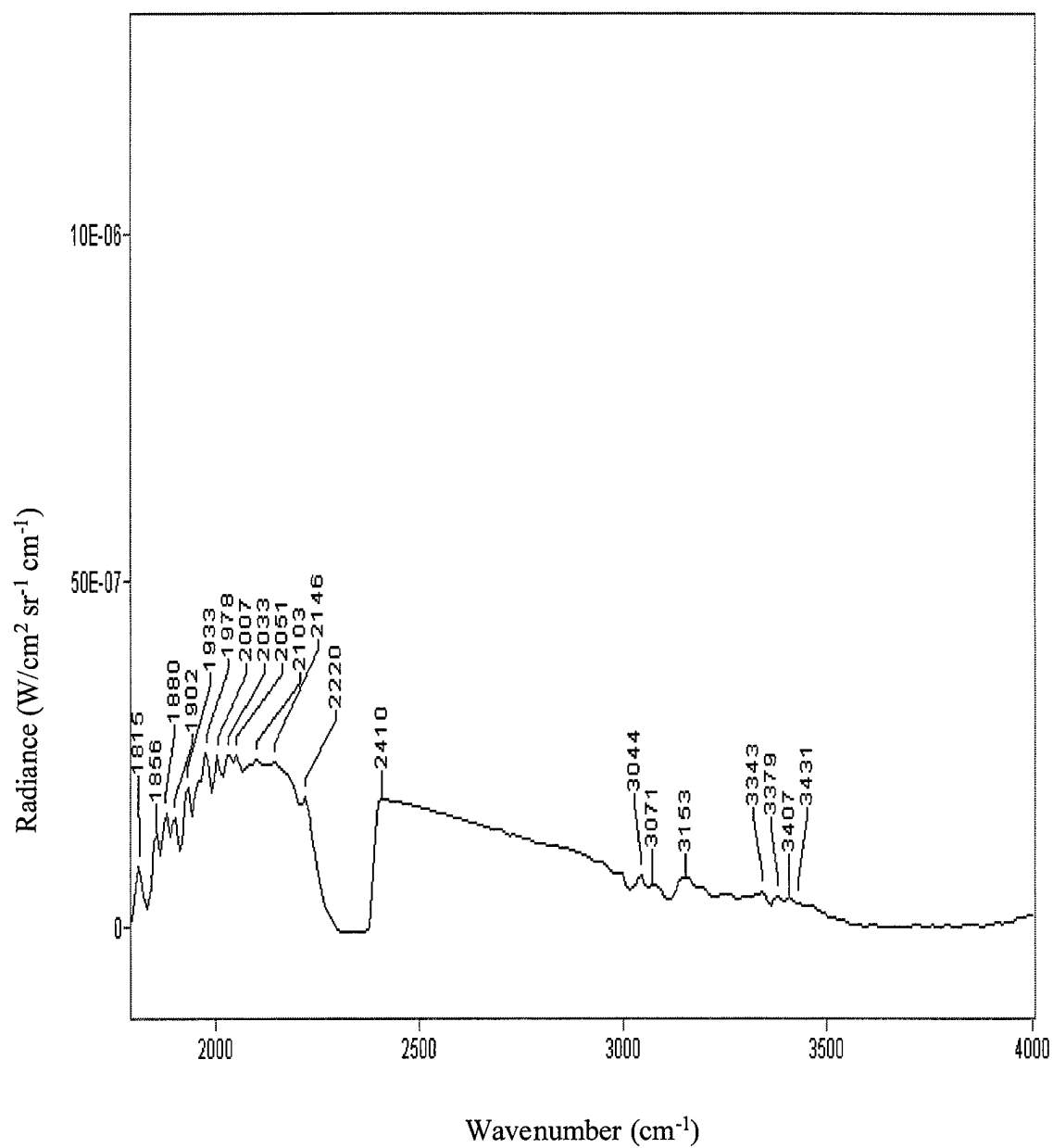


Figure A3.17b. Spectral signature of event A, C-4 plastic explosive 0.270 seconds after Figure A3.17a.

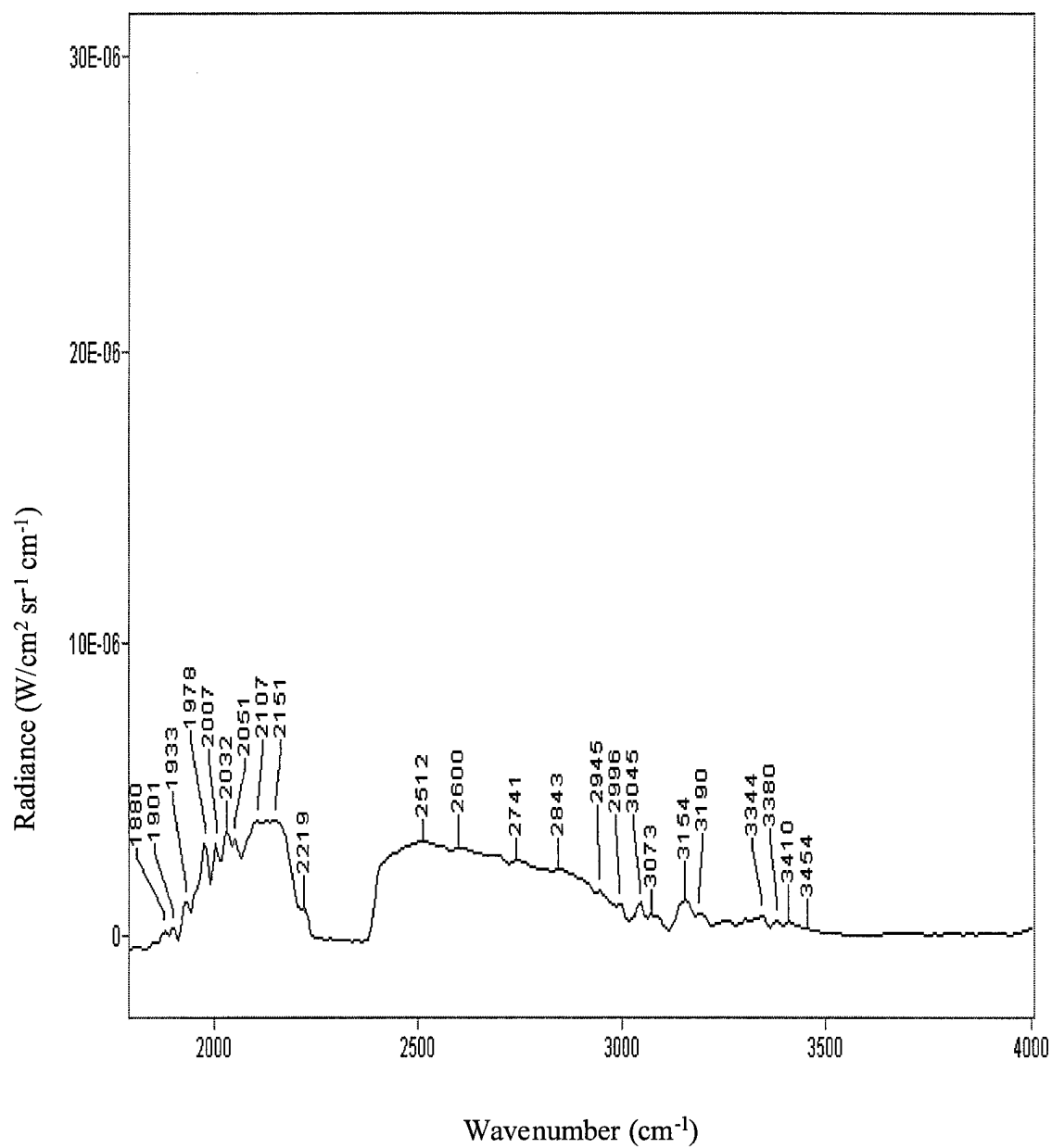


Figure A3.17c. Spectral signature of event A, C-4 plastic explosive 0.538 seconds after Figure A3.17a.

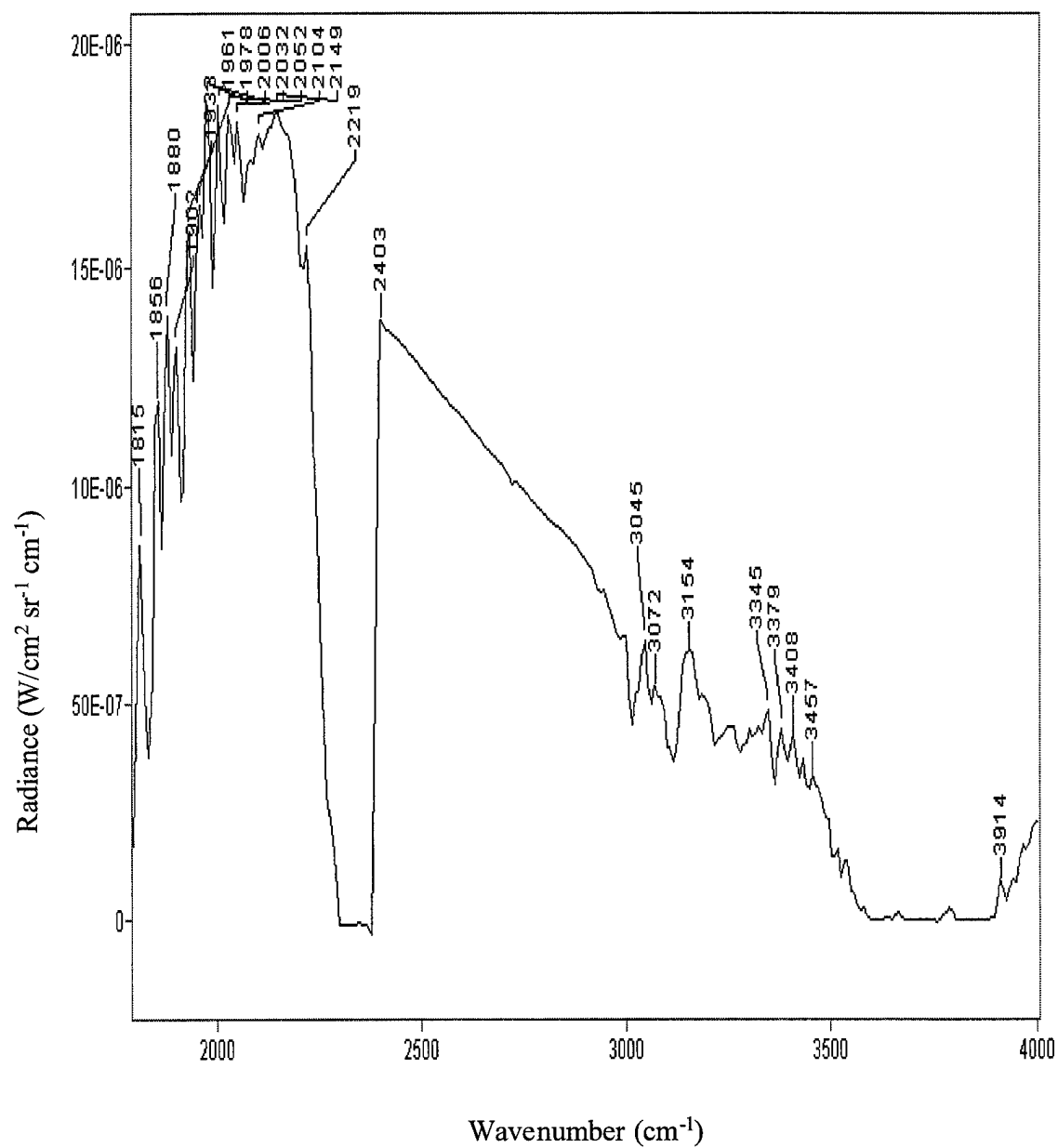


Figure A3.18a. Initial spectral signature retrieved of event C, C-4 plastic explosive detonation.

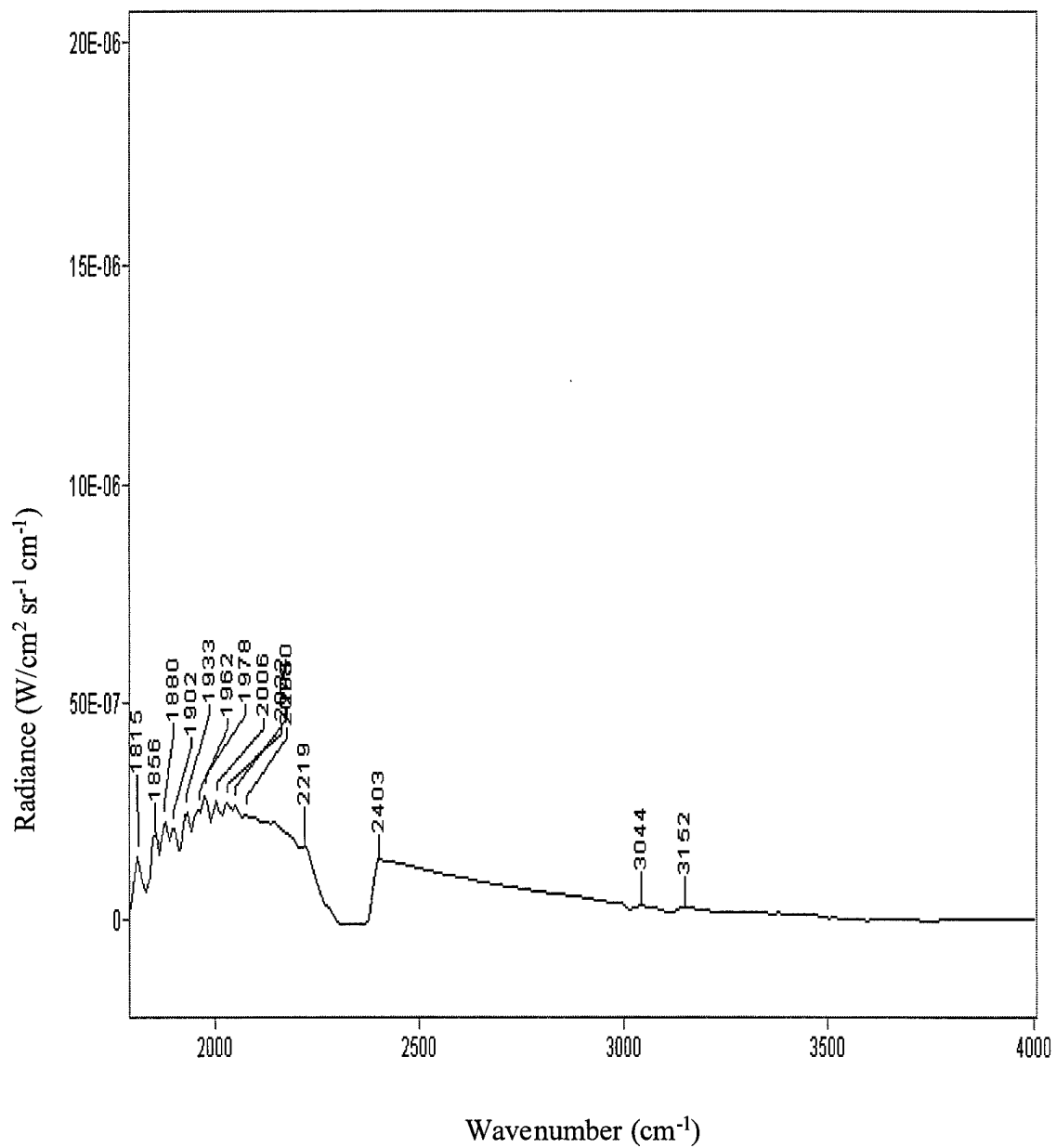


Figure A3.18b. Spectral signature of event C, C-4 plastic explosive 0.538 seconds after Figure A3.18a.

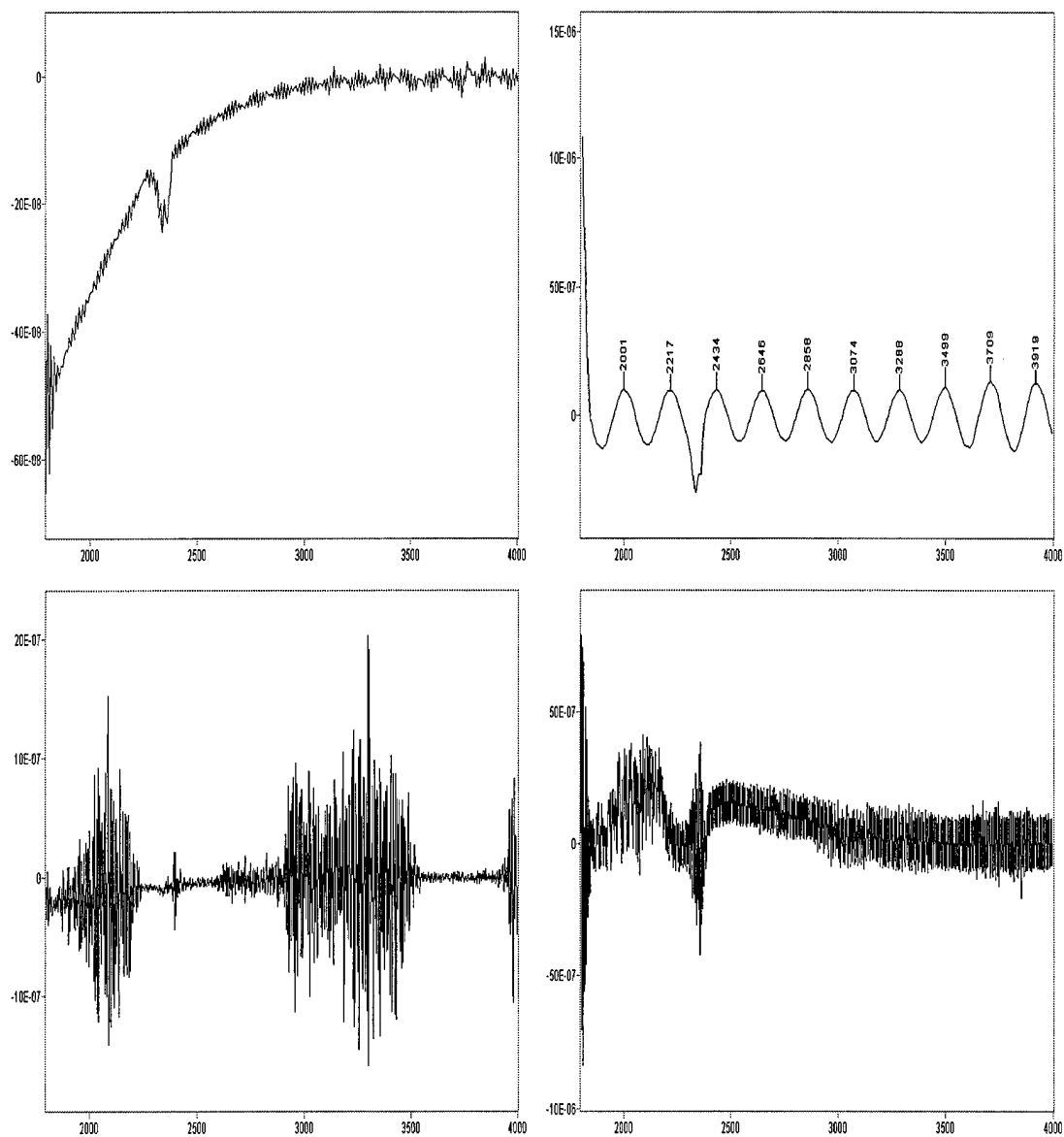


Figure A3.19a. Radio frequency (RF) interference patterns frequently observed one scan prior to the first scan of the explosion event. The RF was attributed to the remote detonators used by EOD.

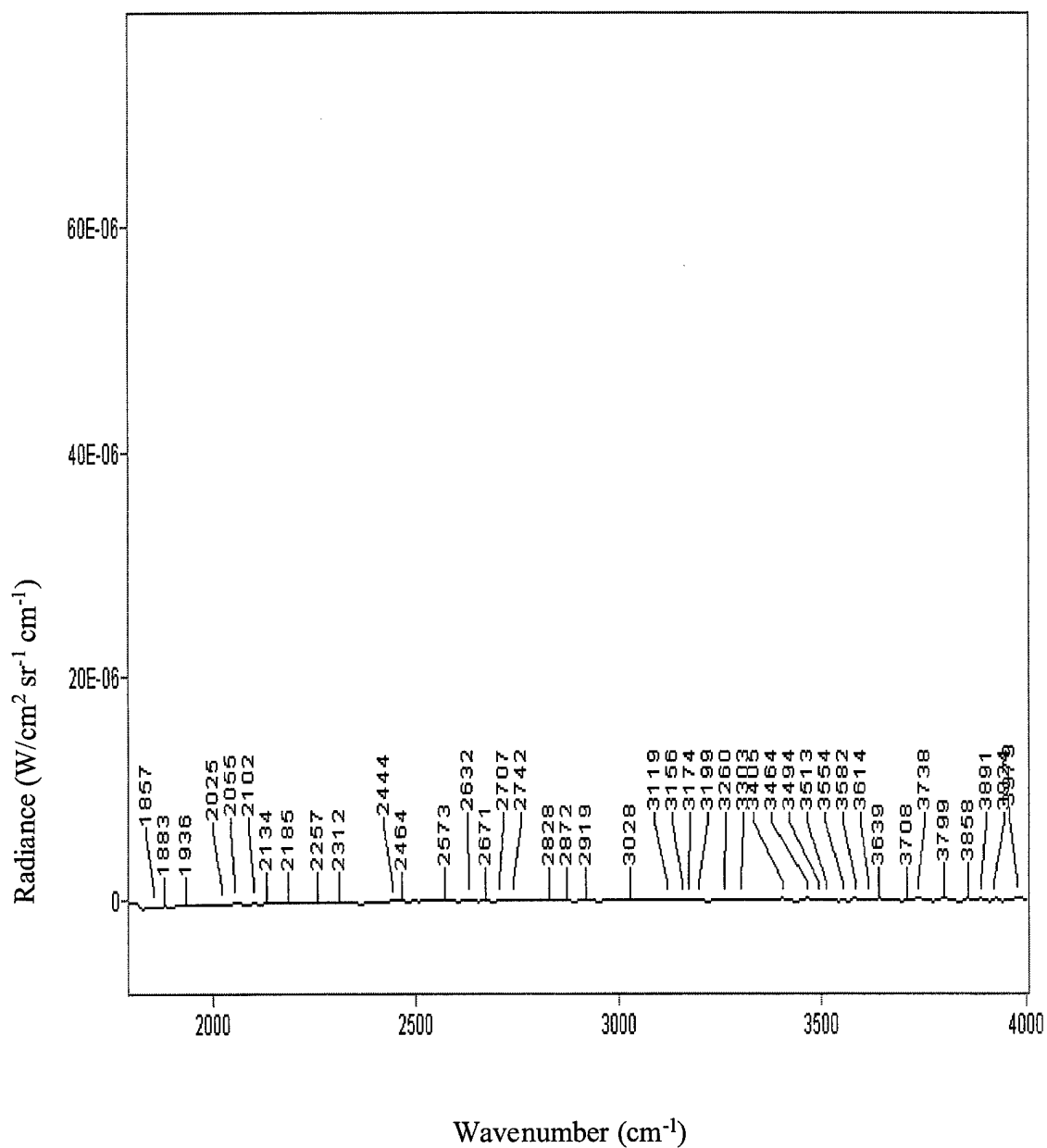


Figure A3.19b. Observed background radiance is negligible when plotted against the scale of a typical explosion event. The peaks identified are likely due to noise in the data and are not necessarily associated with atmospheric absorption.

Bibliography

- Anderson, G. P. and others. "History of One Family of Atmospheric Radiative Transfer Codes," The European Symposium on Satellite Remote Sensing, Conference on Passive IR Remote Sensing of Clouds and Atmosphere, 26-30 September 1994, Rome Italy.
- Berk, Alexander, Lawrence S. Bernstein, and David C. Robertson. MODTRAN: A Moderate Resolution Model for LOWTRAN 7. GL-TR-89-0122, Geophysics Laboratory, Hanscom Air Force Base, MA (30 April 1989).
- BOMEM Users Manual. MR Series FT-Spectroradiometers Design Overview and Theory, Version 1 (May 1995).
- Feltz, Wayne F., and others. "Meteorological Applications of Temperature and Water Vapor Retrievals from the Ground-Based Atmospheric Emitted Radiance Spectrometer (AERI)," Journal of Applied Meteorology, 37: 857-875, (September 1998).
- Goody R. M., and Y. L. Yung. Atmospheric Radiation: Theoretical Basis (Second Edition). New York: Oxford University Press, 1989.
- Herget, William F. "Remote and Cross-stack Measurement of Stack Gas Concentrations Using a Mobile FT-IR System," Applied Optics, 21: 635-641, (15 February 1982).
- "HITRAN 1996." CD-ROM. ONTAR Corporation, 9 Village Way, North Andover, MA.
- Kidder, Stanley Q., and Thomas H. Vonder Haar. Satellite Meteorology: An Introduction. San Diego: Academic Press, 1995.
- Liebowitz, Ruth P., GL Historian. "Historical Brief: GL Propagation Codes for DoD Systems (Revised Edition). Geophysics Laboratory, Hanscom AFB MA, May 1990.
- "PLEXUS." Version 2.1b. CD-ROM. Mission Research Corporation, 1996.
- Smith, William L. "Iterative Solution of the Radiative Transfer Equation for the Temperature and Absorbing Gas Profile of an Atmosphere." Applied Optics, 9: 1993-1999 (September 1970).

Smith, William L. and others. "GAPEX: A Groundbased Atmospheric Profiling Experiment," Bulletin of the American Meteorological Society, 71: 310-318 (March 1990).

Stankov, B. Boba. "Multisensor Retrieval of Atmospheric Properties," Bulletin of the American Meteorological Society, 79: 1835-1854 (September 1998).

Vita

Captain Robert G. Hauser [REDACTED]

[REDACTED]. He entered active duty in November 1983, completed basic training at Lackland AFB, Texas and was sent for technical training at Chanute AFB. His first assignment was at Wright-Patterson AFB where he served as a weather observer, weather forecaster, and wing weather NCO to the 2750th Air Base Wing and 4950th Test Wing.

In 1988, he completed an associate degree in Weather Technology from the Community College of the Air Force. Later that year, he completed his undergraduate degree in Earth Science at the University of Northern Iowa. He was selected for Officer Training School and was commissioned in September 1989. His first assignment as an officer was at Vandenberg AFB, California where he served as a launch weather officer and range meteorological instrumentation officer. He supported fifteen space and missile launches to include Minuteman, Peacekeeper, Scout and Atlas. He was transferred to Wright-Patterson AFB, Ohio in 1991 where he served as a staff meteorologist to the Aeronautical Systems Center and officer in charge of the busiest weather station in Air Force Material Command. His work as staff meteorologist earned him the Air Force Merewether Award for the most significant technical contribution to the weather support mission for 1994. In 1995, he went to Headquarters Air Mobility Command Weather Division as manager, standardization and requirements branch. In August 1997, he entered the Graduate Meteorology program at the Air Force Institute of Technology. Upon graduation, he will be assigned to the Headquarters Air Force Weather Agency.

REPORT DOCUMENTATION PAGE			Form Approved OMB No. 0704-0188	
<small>Public reporting burden for this collection of information is estimated to average 1 hour per response, including the time for reviewing instructions, searching existing data sources, gathering and maintaining the data needed, and completing and reviewing the collection of information. Send comments regarding this burden estimate or any other aspect of this collection of information, including suggestions for reducing this burden, to Washington Headquarters Services, Directorate for Information Operations and Reports, 1215 Jefferson Davis Highway, Suite 1204, Arlington, VA 22202-4302, and to the Office of Management and Budget, Paperwork Reduction Project (0704-0188), Washington, DC 20503.</small>				
1. AGENCY USE ONLY (Leave blank)		2. REPORT DATE February 1999		3. REPORT TYPE AND DATES COVERED Master's Thesis
4. TITLE AND SUBTITLE SURVEY OF MILITARY APPLICATIONS FOR FOURIER TRANSFORM INFRARED (FTIR) SPECTROSCOPY			5. FUNDING NUMBERS	
6. AUTHOR(S) Robert G. Hauser, Captain, USAF				
7. PERFORMING ORGANIZATION NAME(S) AND ADDRESS(ES) Air Force Institute of Technology 2950 P. Street Wright-Patterson AFB OH 45433-7765			8. PERFORMING ORGANIZATION REPORT NUMBER AFIT/GM/ENP/99M-07	
9. SPONSORING/MONITORING AGENCY NAME(S) AND ADDRESS(ES) 88th Weather Squadron 2049 Monohan Way Wright-Patterson AFB OH 45433-7204			10. SPONSORING/MONITORING AGENCY REPORT NUMBER	
11. SUPPLEMENTARY NOTES Lt Col G.P. Perram, ENP				
12a. DISTRIBUTION AVAILABILITY STATEMENT Approved for public release, distribution unlimited.			12b. DISTRIBUTION CODE	
13. ABSTRACT (Maximum 200 words) This paper surveyed four potential military uses for a Fourier Transform Infrared (FTIR) Spectrometer. A physical method to retrieve vertical atmospheric temperature profiles using a least-squares solution on atmospheric radiance observed at the surface in the 4.3-micrometer carbon dioxide absorption band was analyzed. The method was not successful. Weighting functions, calculated from the surface looking up, were a maximum at the surface, so no unique solution for temperature retrieval by height was determined. Observed atmospheric radiance measurements were compared with radiance calculated using the Moderate Resolution Transmittance Code (MODTRAN). Qualitative comparison showed spectral features of observed and calculated radiance plots matched exceptionally well. The utility of the FTIR spectrometer for environmental monitoring was demonstrated by identifying CO ₂ , CO, O ₃ , HCl, SO ₂ , and N ₂ O emissions from a coal-burning plant smokestack. An FTIR spectrometer was used to collect data of controlled detonations of statically displayed Mk 82, Mk 83, and Mk 84 bombs; High-speed Anti-Radiant Missiles (HARM); Tomahawk Land-Attack Missiles (TLAM); and C-4 plastic explosive over the 1800-6000 cm ⁻¹ spectral band at 16 cm ⁻¹ resolution. Results showed there were unique spectral features associated with some warhead types.				
14. SUBJECT TERMS Fourier Transform Infrared (FTIR) Spectrometer, spectroscopy, FTIR, physical retrieval, weighting functions, MODTRAN, atmospheric radiance, environmental monitoring, spectral plots of explosions			15. NUMBER OF PAGES 145	
			16. PRICE CODE	
17. SECURITY CLASSIFICATION OF REPORT UNCLASSIFIED	18. SECURITY CLASSIFICATION OF THIS PAGE UNCLASSIFIED	19. SECURITY CLASSIFICATION OF ABSTRACT UNCLASSIFIED	20. LIMITATION OF ABSTRACT UL	